STABLE HIGH CONDUCTIVITY BILAYERED ELECTROLYTES FOR LOW TEMPERATURE SOLID OXIDE FUEL CELLS

FETC AAD Document Control Bldg. 921
U.S. Department of Energy
Federal Energy Technology Center
P.O. Box 10940
Pittsburgh, PA 15236-0940

Contract # DE-AC26-99FT40712

Program Manager: Lane Wilson

Annual Report for Period 10/1/00 - 9/30/01

Eric D. Wachsman and Keith L. Duncan
Department of Materials Science and Engineering
University of Florida
Gainesville, FL 32611-6400

CONTENTS

EXECUTIVE SUMMARY

In this annual report to the US Department of Energy, we summarize the results of our research on stable high conductivity bilayered electrolytes for low temperature solid oxide fuel cells (Contract # DE-AC26-99FT40712). The report covers our progress in experimentation and computer modeling, and includes experimental verification of the model.

Initial experimental work focused on optimizing the fabrication of samaria-doped ceria (SDC) in order to maximize its density and conductivity. This is important because of SDCs notoriously poor sinterability. We then deposited an erbia stabilized bismuth oxide (ESB) layer on the SDC substrates using pulsed laser deposition (PLD). Because of the time needed for deposition, we were able to deposit only very thin (< 2 μm) ESB layers. Evaluation of the microstructure revealed that the ESB film adhered well to the SDC substrate and interdiffusion was not detectable. Further, we found that the resistance of the bilayer was in fact less than that of the SDC alone, confirming at the very least that no lower conducting phase formed at the bilayer interface.

We have also developed a new oxygen ion conductor based on Bi_2O_3 doped with Dy_2O_3 and WO_3 (DyWSB). It exhibits a higher conductivity than that of 20 mol% erbia stabilized bismuth oxide (20ESB), thus, giving it the highest conductivity of any known solid oxide electrolyte. Electrical conductivity results of the Dy - W stabilized bismuth oxide system are presented. The dopants were selected based on their polarizability and its effect on structural stability and conductivity. At 800°C the conductivity of $(BiO_{1.5})_{0.88}(DyO_{1.5})_{0.08}(WO_3)_{0.04}$ is 0.57 S/cm (1.5 times as high as that of 20ESB), and at 500°C the conductivity is 0.043 S/cm (2 times as high as that of 20ESB). Consequently, because its conductivity is even higher than ESB, we anticipate even better performance than originally predicted when it is incorporated into the bilayer.

We examined the electrochemical performance of SDC and ESB/SDC bilayer SOFCs as a function of anode P_{O_2} under open-circuit conditions (sections 4 and 6). SDC was examined first (section 4) to establish a suitable baseline for comparison. Our SDC based concentration cells performed as expected, with a low open-circuit potential (OCP) and effective ionic transference number (t_{ion}) due to electronic conduction. In contrast, results for SOFCs with bilayered electrolytes (section 6) showed they had higher OCP and t_{ion} values (approaching unity) compared to those with a single SDC layer. Further, we confirmed that OCP and t_{ion} increased as the relative thickness of the ESB layer increased, thereby re-confirming the bilayer concept. Despite this achievement, however, there is still work to be done on optimizing the thickness

ratio of the constituent layers (to achieve maximum performance) and evaluating the closed circuit performance of the bilayer.

We have also begun work on developing suitable anodes for the bilayers and a technique for depositing acceptor (samaria or gadolinia) doped ceria on them to form the basis for an anode supported bilayered SOFC. Investigation into the effect of relative thickness of the bilayers is further facilitated by electrode supported electrolytes, as fabrication of the bilayer requires some ingenuity due to the large difference in the sintering temperatures of bismuth oxide and ceria. As a first step, we report the fabrication and performance of Ni-gadolinium doped ceria (GDC) anode supported GDC thick film electrolyte, using a colloidal deposition method. Colloidal deposition has advantages over other techniques for thick film processing in its simplicity, cost-effectiveness, upscalibility and flexibility (thickness ranging from 10-100μm can be deposited). Further, under the reducing conditions at the anode doped ceria is a mixed ionic electronic conductor and hence, the reaction zone will not be restricted to the interface of the anode and the electrolyte leading to enhanced performance of the anode.

In order to further establish a sound theoretical basis for our approach, we have also extended, revised and applied our theoretical models for the generation, distribution and transport of defect in oxide mixed ionic-electronic conductors. For the sake of brevity, the report omits much of the model development and also focuses primarily (though not exclusively) on open-circuit conditions. In section 3, a model for defect distribution is developed based on the usual transport laws for charged species in a concentration gradient. The model is used (along with earlier models) to show how essential material constants may be obtained from various experimental data. In section 4, the model was verified through fitting to experimental data (measured vs. theoretical OCP). In all cases, correlation coefficients (corrected for two degrees of freedom) greater than 95% were obtained, thus, confirming the validity of the model.

Finally, the bilayer model, presented in an earlier report, was revised and extended to closed circuit conditions. In the revision, two very disparate approaches were taken and shown to yield essentially identical results for open-circuit conditions, thereby corroborating the validity of each. Perhaps of more interest, however, is that the predictions show that low area specific resistances (ASRs) are achievable using bilayer architecture for fuel cell electrolytes in open-circuit conditions.

Even more appealing results were obtained when the bilayer was modeled for closed-circuit conditions. In closed-circuit conditions, electronic species will flow primarily through the external circuit especially in the presence of the electron-blocking ESB layer. Consequently, the sole diffusing species inside the electrolyte (in closed-circuit conditions) are oxygen vacancies

and ESB is much less resistive to their transport than SDC. Therefore, the potential drop per unit length is much larger for SDC than ESB and a thin SDC layer will sustain enough voltage to protect the sensitive ESB layer. This situation is in contrast to open-circuit conditions where the diffusing species (oxygen atoms via ambipolar diffusion) is electrically neutral and ESB is the more resistive layer due to the unavailability (in comparison to SDC) of electronic species.

In closing, both experiment and theory support the viability of stable high conductivity bilayered electrolytes for low temperature solid oxide fuel cells. More work remains to be done, but present results demonstrate that we are on the right course.

1. INTRODUCTION

Solid oxide fuel cells (SOFCs) are the future of energy production in America. They offer great promise as a clean and efficient process for directly converting chemical energy to electricity while providing significant environmental benefits (they produce negligible hydrocarbons, CO, or NO_x and, as a result of their high efficiency, produce about one-third less CO_2 per kilowatt hour than internal combustion engines).

Unfortunately, the current SOFC technology, based on a stabilized zirconia electrolyte, must operate in the region of 1000°C to avoid unacceptably high ohmic losses. These high temperatures demand (a) specialized (expensive) materials for the fuel cell interconnects and insulation, (b) time to heat up to the operating temperature and (c) energy input to arrive at the operating temperature. Therefore, if fuel cells could be designed to give a reasonable power output at low to intermediate[1] temperatures tremendous benefits may be accrued. At low temperatures, in particular, it becomes feasible to use ferritic steel for interconnects instead of expensive and brittle ceramic materials such as those based on $LaCrO_3$. In addition, sealing the fuel cell becomes easier and more reliable; rapid start-up is facilitated; thermal stresses (e.g., those caused by thermal expansion mismatches) are reduced; radiative losses ($\sim T^4$) become minimal; electrode sintering becomes negligible and (due to a smaller thermodynamic penalty) the SOFC operating cycle (heating from ambient) would be more efficient. Combined, all these improvements further result in reduced initial and operating costs. The problem is, at lower temperatures the conductivity of the conventional stabilized zirconia electrolyte decreases to the point where it cannot supply electrical current efficiently to an external load.

The primary objectives of the proposed research are to develop a stable high conductivity (> 0.05 S cm^{-1} at ≤ 550 °C) electrolyte for lower temperature SOFCs. This objective is specifically directed toward meeting the lowest (and most difficult) temperature criteria for the 21st Century Fuel Cell Program. Meeting this objective provides a potential for future transportation applications of SOFCs, where their ability to directly use hydrocarbon fuels could permit refueling within the existing transportation infrastructure.

In order to meet this objective we are developing a functionally gradient bilayer electrolyte comprised of bismuth oxide on the air side and ceria on the fuel side. Bismuth oxide and doped ceria are among the highest ionic conducting electrolytes and in fact bismuth oxide

[1] In accordance with current convention, the term "low" is used here to for temperatures < 600 °C while the term "intermediate" refers to temperatures in the range 500-800 °C.

based electrolytes are the only known solid oxide electrolytes to have an ionic conductivity that meets the program conductivity goal.

The bilayered electrolyte we are developing consists of a layer of erbia-stabilized bismuth oxide (ESB) on the oxidizing side and a layer of SDC or GDC on the reducing side. In this arrangement, the ceria layer protects the bismuth oxide layer from decomposing by shielding it from very low P_{O_2}'s and the ESB layer serves to block electronic flux through the electrolyte. This arrangement has two significant advantages over the YSZ\SDC bilayers investigated by others [1, 2]. The first advantage is that SDC is conductive enough to serve as an intermediate temperature SOFC electrolyte. Moreover, ESB is conductive enough to serve as a low temperature electrolyte. Consequently, at worst an SDC\ESB bilayered SOFC should have the conductivity of SDC but with improved efficiency due to the electronic flux barrier provided by ESB. The second advantage is that small (dopant) concentrations of SDC in ESB or ESB in SDC, have been found to have conductivities comparable to the host lattice [3, 4]. Therefore, if solid solutioning occurs at the SDC-ESB interface, it should not be detrimental to the performance of the bilayer. In contrast, solid solutions of SDC and YSZ have been found to be significantly less conductive than SDC or YSZ. Thus, it bears emphasizing that, at this time, only SDC\ESB electrolytes have potential in low temperature SOFC applications.

The primary issue concerning SDC\ESB bilayers, is assessing the stability of ESB in this arrangement for various fuel cell operating conditions and optimizing the relative thickness of the SDC and ESB layers so that the oxygen partial pressure at the SDC-ESB interface is high enough to prevent decomposition of the ESB. In *open-circuit* conditions the stability of ESB must be determined by calculating (since direct measurement is not presently feasible) the effective P_{O_2} at the interface, which, as shown in Figure 1-1, is a function of the relative thicknesses of the layers. Ideally, the effective interfacial P_{O_2} should not fall below ~ 10^{-13} atm. (i.e., the P_{O_2} bismuth oxide below which decomposes) for the SDC\ESB bilayer. Under *closed-circuit* conditions one can no longer talk about an effective interfacial P_{O_2} since the oxygen is no longer permeating by ambipolar diffusion through the bilayer. Therefore, as shown later, other indicators of stability must be used.

We have previously demonstrated that this concept works, that a bismuth oxide/ceria bilayer electrolyte provides near theoretical open circuit potential (OCP) and is stable for 1400 h of fuel cell operation under both open circuit and maximum power conditions. More recently, we developed an analytical model to determine the defect transport in this bilayer and have found that a bilayer comprised primarily of the more conductive component (bismuth oxide) is stable for 500°C operation.

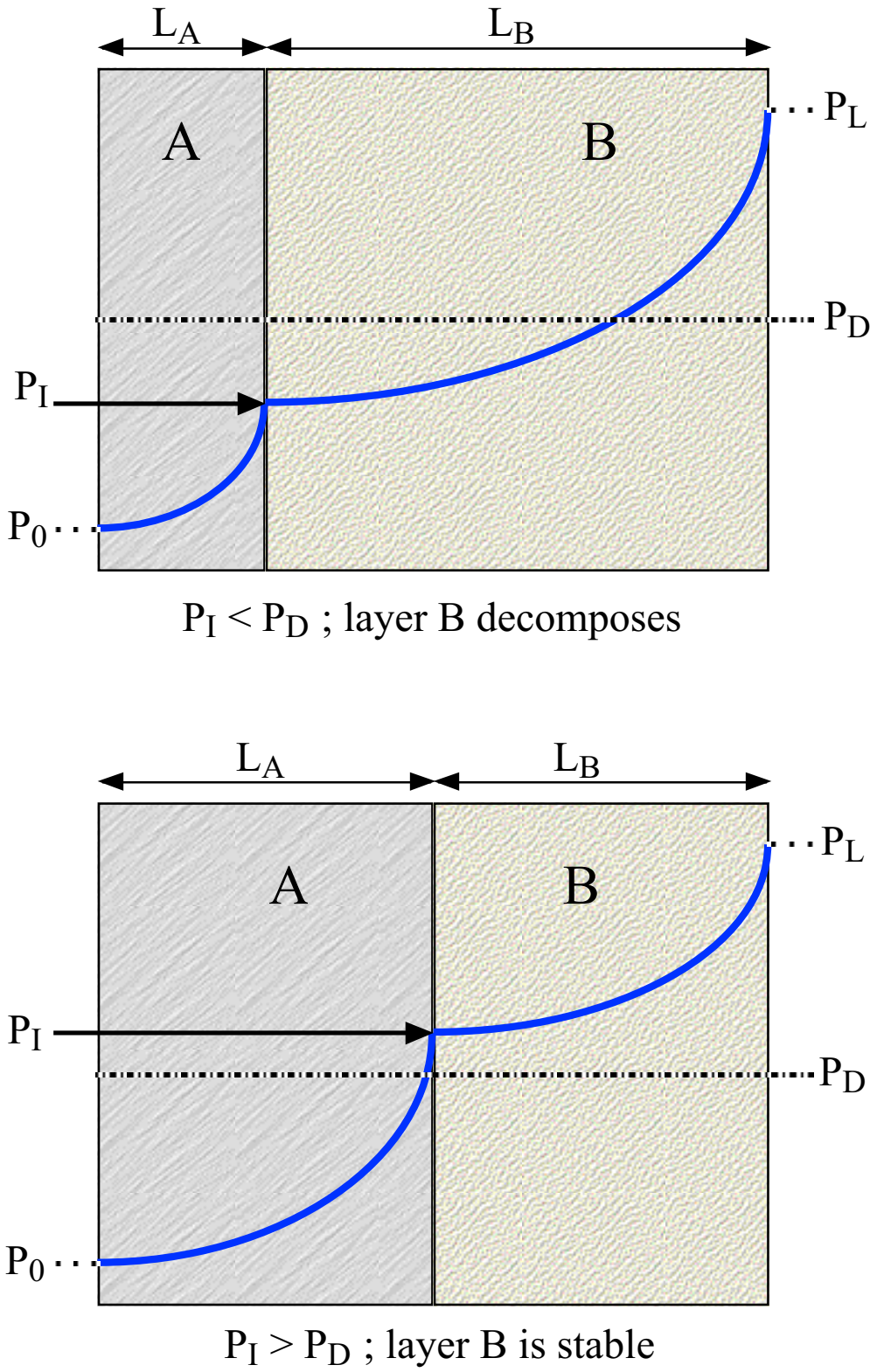

Figure 1-1. Conceptual representation of a bilayered electrolyte showing the effect of relative thickness on interfacial P_{O_2}, P_I; P_0 is the P_{O_2} (at x = 0) on the fuel/anode side, P_L is the P_{O_2} (at x = L) on the air/cathode side and P_D is the decomposition P_{O_2}.

In this report, the fabrication and characterization of single-layered electrolytes of SDC, ESB and bilayered electrolytes of SDC\ESB are presented. Fabrication techniques include standard ceramic processing with uni-axial pressing and with cold isostatic pressing (CIP). Characterization techniques include x-ray diffraction, density analysis, scanning electron microscopy (SEM), x-ray photo-electronic spectroscopy (XPS), energy dispersive spectroscopy (EDS) and electrical impedance spectroscopy (EIS) and open-circuit potential (OCP) measurements. The report also contains a (revised) model that was developed to predict the spatial distribution and transport properties of ionic and mixed ionic-electronic conductors (MIECs). First, the correctness of the model is verified by fitting it to experimental data for the OCP of an SDC based SOFC. Then the model is applied to bilayered electrolytes in order to obtain a relationship between the thickness ratio of the constituent layers of the SDC\ESB bilayer and interfacial conditions—i.e., an oxygen potential, P_{O_2}, drop (in open circuit conditions) or an electrical potential drop (in closed-circuit conditions)—for various fuel cell operating conditions. Finally, the model's predictions are again compared to experimental results for the OCP of SDC\ESB bilayered SOFCs.

2. EXPERIMENTAL

Previously, we completed the assembly, calibration and testing of the SOFC apparatus and a preliminary sintering study. Since then, the sintering study (of particular interest to SDC fabrication because of its extremely high sintering temperature) has been completed and is presented in this section. SDC and SDC\ESB samples were also analyzed to ensure that they had the correct (fluorite) structure, (which also served as an indirect test for the presence of secondary *impurity* phases) and the correct chemical composition and a suitable (and acceptably pore-free) microstructure. Finally, SDC and SDC\ESB samples were characterized for electrical conductivity via electrical impedance spectroscopy (EIS) and, for the former, the impact of processing techniques, impurities and microstructure on conductivity was assessed.

2.1 FABRICATION AND CHARACTERIZATION OF SDC AND SDC\ESB BILAYER

2.1.1 Samaria-Doped Ceria (SDC)

SDC powders were calcined at 1100, 1200 and 1300°C for 10hrs and sintered at 1465 °C, 1550 °C, and 1650 °C for 15 hrs. The densities of the SDC pellets prepared were found to be 70–98% of the theoretical density depending on the sintering temperature. Figure 2-1 shows the measured relative densities of SDC samples as a function of axially applied pressure by changing

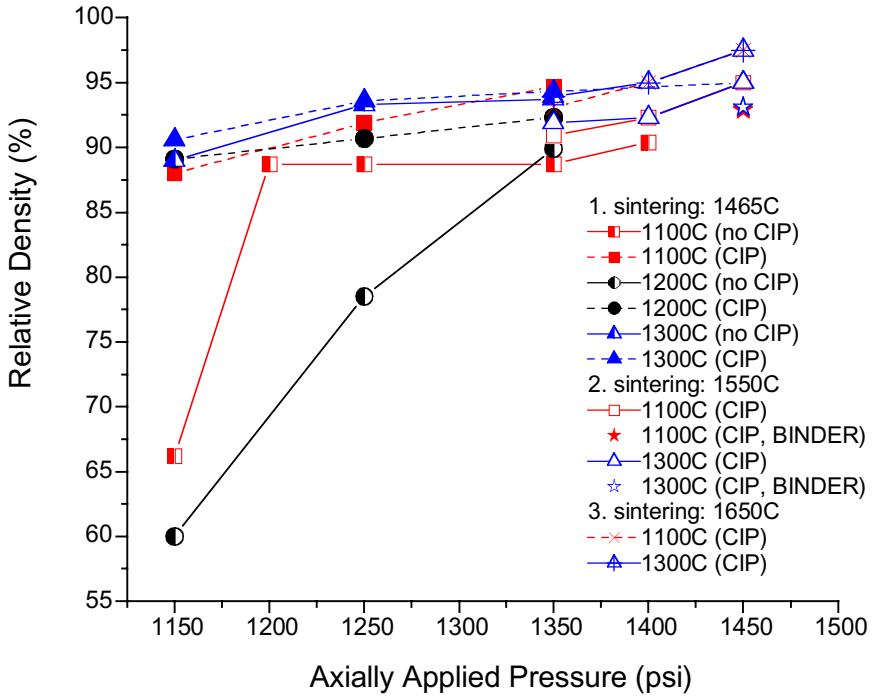

Figure 2-1. Effect of axially and isostatically pressing, calcining and sintering temperature, and binder (P.E.G. 8000) on SDC pellets

sintering temperature, calcination temperature, binder, and the use of cold-isostatic pressing (CIP). The density, ρ, of the sintered samples increased with the sintering temperature. Fabrication of SDC pellets by the solid-state technique required a fairly high temperature of 1600 °C in order to get more than 95% theoretical density. However, sintering at these temperatures is expensive and makes co-firing doped ceria with other materials difficult due to severe solid-state reaction and inter-diffusion at those temperatures [5]. Thus, it would be beneficial to fabricate doped ceria electrolyte at the lowest temperature as possible. To this end, Huang *et al*. [6] demonstrated that the small average particle size of sol-gel prepared green-bodies allows sintering of SDC samples into highly dense pellets at a significantly lower temperature of 1400°C, versus 1600°C required for conventionally prepared samples.

Theoretically, denser and/or stronger green-bodies may be obtained through one or a combination of: increased pressing load, binder (typical organic liquids) reinforcement or isostatic pressing. All three methods were tested in an attempt to simultaneously increase the density and lower the sintering temperature of SDC samples.

The uni-axial pressing load was increased systematically for SDC samples, Figure 2-1. However, it was found that increasing the uni-axial pressing load above 1500 psi causes de-lamination and end capping—two of the more common defects in die-compacted powders [7].

The binder polyethylene glycol (PEG) 8000 was tried in an attempt to increase the green-body strength. However, it was found (rather unexpectedly) that after sintering, the densities of the samples prepared with the PEG binder were lower than those prepared without it. This result was surprising because the PEG binder had increased the observed strength of the green-body after compaction (pressing). The reduction in sintered sample density may be attributable to structural anisotropy introduced by the binder that resulted in voids formation during sintering.

The highest SDC sample densities were achieved with cold-isostatically pressed samples. Cold-isostatic pressing increased the densities of the sintered samples because the pressing load is uniform and, consequently, powder movement (which causes de-lamination) is reduced [7].

2.1.2 Erbia-Stabilized Bismuth Oxide (ESB)

Disks of 20 mol.% Er_2O_3-Bi_2O_3 were fabricated by a solid state reaction. Bi_2O_3 (99.9995% pure) and Er_2O_3 (99.99% pure) powders were obtained from Alfa Aesar. The powders were mixed and ball-milled with magnesia stabilized zirconia ball media in a Nalgene® jar for 20 hours. The mixed powders were calcined at 800°C for 16 hours. Agglomerated powders were ground again using mortar and pestle and pressed into a disk-shaped 1 1/8-inch die using 5000 psi for OCP measurements and 1/4 inch die using 3000 psi for conductivity measurements. Polyvinyl alcohol (PVA) and stearic acid mixed with reagent alcohol were added as a binder and a lubricant respectively. The resulting green bodies were sintered in air at 890°C for 16 hours. After sintering, the specimens were polished to acquire even surfaces and desired thicknesses (1.5 mm and 2 mm for OCP and conductivity experiments respectively).

2.1.3 A New Oxygen Ion Conductor: Dy and W Stabilized Bismuth Oxide (DWSB)

The high ionic conductivity of δ-Bi_2O_3 is ascribed both to the large number of oxygen vacancies and a high anion mobility. The high concentration of oxygen vacancies (25% of the lattice sites) is a result of obtaining the fluorite structure with a Bi^{3+} cation. The high anion mobility is related to the high polarizability of the Bi^{3+} cation with its lone pair of electrons [8].

Pure bismuth oxide transforms to monoclinic α-phase on cooling below 730°C. The cubic phase at high temperature can be stabilized down to room temperature by the additions of dopants such as isovalent rare earth cations. However, these doped bismuth oxides show lower conductivity and undergo an order-disorder transition of the oxygen sublattice below 600°C, which leads to a decay in conductivity (aging effect) [9 - 11]. Our results have shown that the dopant cations affect the nature of the vacancy arrangement in the oxygen sublattice [9, 12, 13] and the polarizability of the cation affects the stability of the disordered oxygen sublattice [14].

These results showed that the most polarizable of the lanthanide dopants, Dy, provided the greatest stability for the disordered anion lattice [14]. Among the potential dopants to stabilize the fluorite structure of Bi_2O_3, W has the highest polarizability and therefore should also provide stability for the disordered anion lattice. Moreover, based on the results of Battle et al [8], the high polarizability of Dy and W should result in a high anion mobility.

Takahashi et al [15] reported that WO_3 stabilized Bi_2O_3 has high conductivity, but the fcc phase was stable only over a narrow composition range (22 - 28 mol % WO_3 in Bi_2O_3). Verkerk and Burggraaf [16] investigated the phase stability and oxygen ion conductivity of Dy_2O_3 stabilized Bi_2O_3. They found that the cubic structure was stable at low temperatures for the solid solutions containing 28.5 - 50 % Dy_2O_3. In both investigations it was found that the highest conductivity was obtained for the lowest dopant concentration that would stabilize the fcc phase ($(BiO_{1.5})_{0.88}(WO_3)_{0.12}$ and $(BiO_{1.5})_{0.715}(DyO_{1.5})_{0.285}$). Therefore, based on the cation ratio the fcc structure can be stabilized with W at a lower dopant concentration than with Dy. In addition, studies [17, 18] have shown that the face-centered cubic structure in the Bi_2O_3-based solid solutions can be stabilized down to room temperature with two rare earth oxide dopants with smaller total dopant concentrations. Since smaller dopant concentrations have higher conductivity, this results in an increase in conductivity, especially in the lower temperature regions. Therefore, we tried doping Bi_2O_3 with both Dy_2O_3 and WO_3 (DyWSB), the highly polarizable dopants, in order to obtain a structurally stable electrolyte with high conductivity.

Disks of Dy_2O_3 - WO_3 - Bi_2O_3 were fabricated for conductivity measurements by solid state reaction. Disks of $(BiO_{1.5})_{0.8}(ErO_{1.5})_{0.2}$, 20ESB, were also prepared for comparison of conductivity results. Six compositions were investigated: $(BiO_{1.5})_{0.87}(DyO_{1.5})_{0.10}(WO_3)_{0.03}$, $(BiO_{1.5})_{0.88}(DyO_{1.5})_{0.08}(WO_3)_{0.04}$, $(BiO_{1.5})_{0.89}(DyO_{1.5})_{0.06}(WO_3)_{0.05,}$ and $(BiO_{1.5})_{0.83}(DyO_{1.5})_{0.17-x}(WO_3)_x$ (where x = 0.05, 0.08, 0.12). The latter 3 compositions with a fixed 17% total dopant content are 12Dy5WSB, 9Dy8WSB and 5Dy12WSB. The former 3 compositions with a total dopant content between 11-13% are 10Dy3WSB, 8Dy4WSB and 6Dy5WSB.

Powders of Bi_2O_3 (99.9995% pure), Er_2O_3 (99.99% pure), Dy_2O_3 (99.99% pure) and WO_3 (99.8% pure), from Alfa Aesar, were mixed and ball-milled with zirconia ball media in a high-density polyethylene bottle for 20 hours. The mixed powders were calcined at 800°C for 16 hours. Agglomerated powders were ground again using mortar and pestle and pressed into a disk-shaped 0.635 cm die using 2 x 10^5 N/m^2. Poly vinyl alcohol was used as a binder and stearic acid mixed with reagent alcohol as a lubricant. The subsequent green bodies were sintered in air at 890°C for 16 hours. Powder X-ray diffraction (XRD) data were obtained at room temperature for phase analysis. The XRD patterns were obtained using CuKα radiation with a nickel filter. All compositions were found to be fcc structure.

After sintering, the specimens were polished to acquire an even surface and the desired thickness (2 mm). Engelhard gold paste mixed with isopropanol was brushed onto both sides of the electrolytes, and the organic additives were evaporated at 127°C for 30 minutes. Subsequently the electrodes were sintered at 800°C for 30 minutes. Gold wires (99.95% pure, DFG) spot-welded with circular gold mesh (99.9% pure, 100 mesh, DFG) were attached to the cells using Au paste and were sintered again at 800°C for 30 minutes.

2.1.4 SDC\ESB Bilayers

Sintered SDC pellets were coated on one face with a thin film of ESB via pulsed laser deposition (PLD) using a Lambda Physik pulsed excimer laser. For coating, an ESB target was rotated at 2 RPM, the laser was pulsed at 5Hz at a laser energy of 400mJ, with a substrate temperature of 700°C. Film thickness was measured by elipsometry of films deposited on Si with identical deposition parameters.

Figure 2-2 shows a linear relationship between film thickness and deposition time for the growth of an ESB film on a SDC substrate. A key feature of the ESB film is that it should be pinhole free to block access of the cathode (or cathodic conditions) to SDC. By so doing, the ESB layer prevents electronic conduction (which occurs in single layer SDC membranes) in the bilayered membrane. In the present study, the thickness of the ESB film was limited to 2 μm. This limitation was imposed by the long depositions times required (it took several hours each to evacuate, heat up, deposit and cool down).

The desired structure for SDC and ESB is the fluorite structure. The XRD patterns in Figure 2-3 show that a fluorite structure was obtained for SDC, ESB and the bilayered ESB\SDC samples. Although expected, this result also indicates that other phases (arising from reactions between SDC and ESB at their interface) are not present to any large degree and, by extension, that PLD is an acceptable way to deposit ESB on an SDC substrate.

Figure 2-4 shows an SEM micrograph of the cross-section of an ESB film (deposited by PLD) on a dense SDC substrate (i.e., the bilayered ESB\SDC electrolytes). Cross-sectional views indicate that the film adhered well to the baseline ceria substrate. The chemical composition of the bilayered ESB\SDC electrolytes was obtained, Figure 2-5, from energy dispersive analysis (EDS). The SEM in Figure 2-5(a) shows the region that was line-scanned and Figures 2-5(b) (graph) and 2-5(c) (picture) show the compositional results of the linescan. It is apparent (at this resolution) in Figure 2-5(b), that neither solid-state reaction nor inter-diffusion between the phases has occurred. Finally, the EDS spectra, in Figure 2-5(d), of the

SDC\ESB sample cross-section in Figure 2-5(a) shows that any impurity levels are below detectable limits.

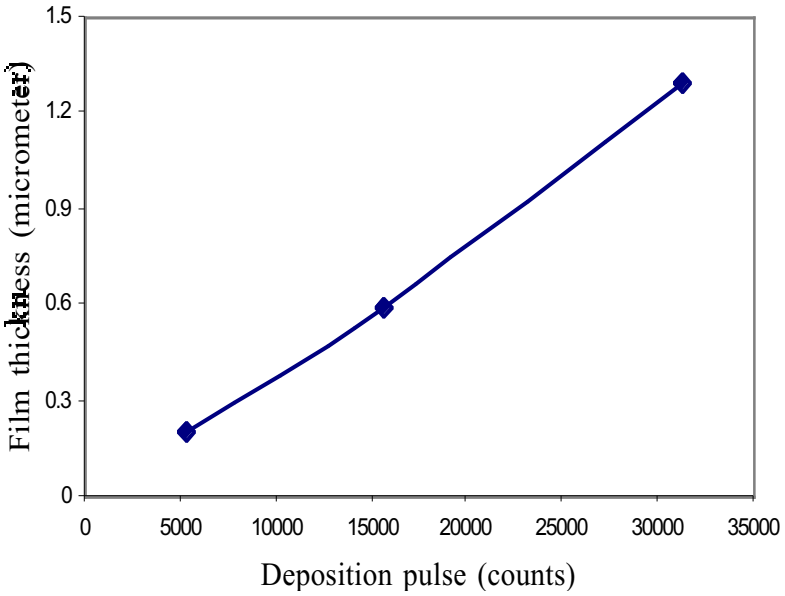

Figure 2-2. Thin film thickness on SDC substrate as a function of deposition time (pulses)

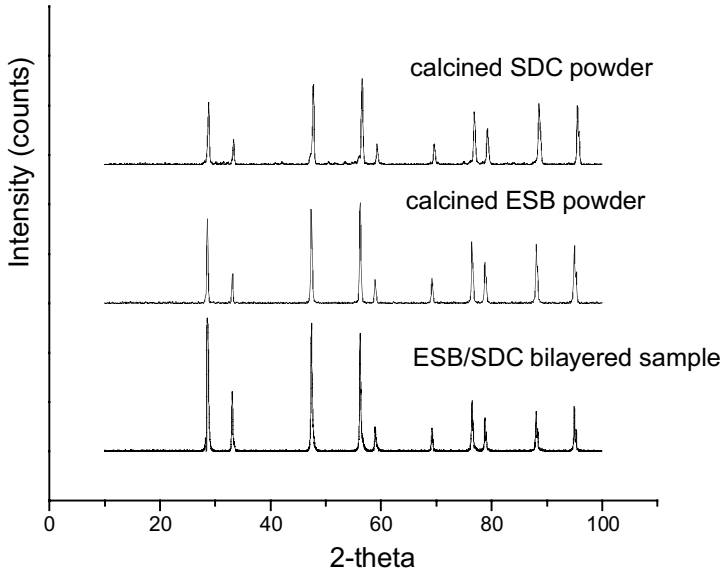

Figure 2-3. X-ray diffraction patterns of (top) SDC powder (middle) ESB powder and (bottom) SDC coated with ESB (bilayered SDC\ESB electrolyte, film thickness: 0.2 μm) via PLD.

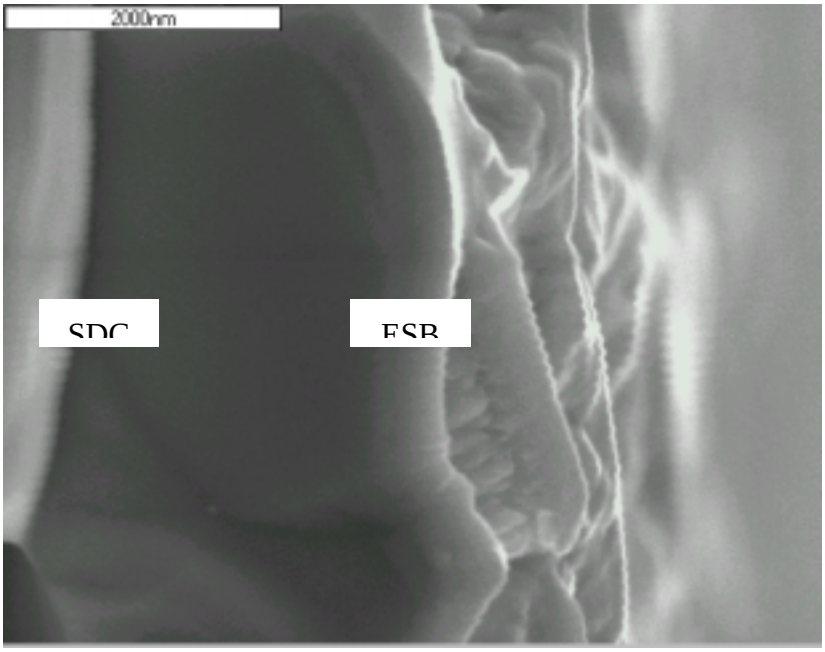

Figure 2-4 Cross-section SEM of ESB film on a dense SDC substrate (ESB\SDC bilayer)

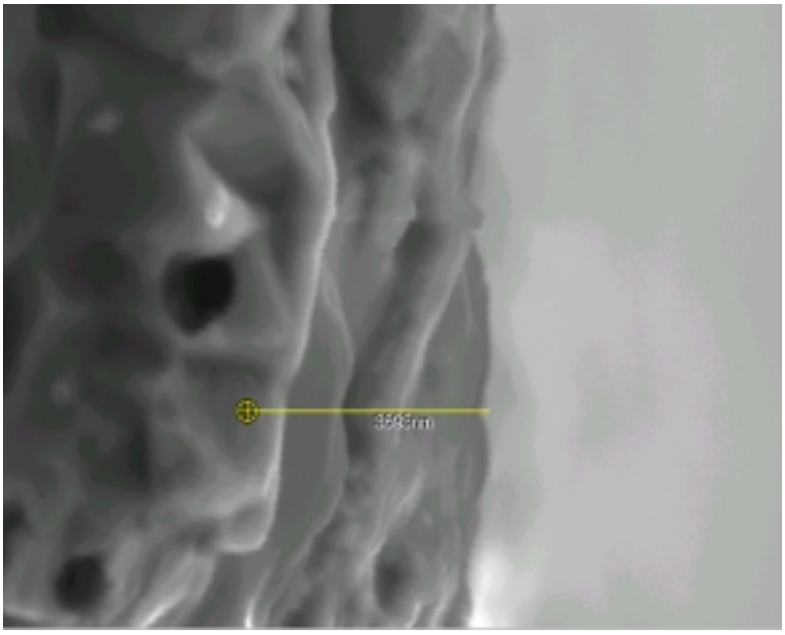

Figure 2-5(a). Line scanned SEM image of SDC\ESB sample.

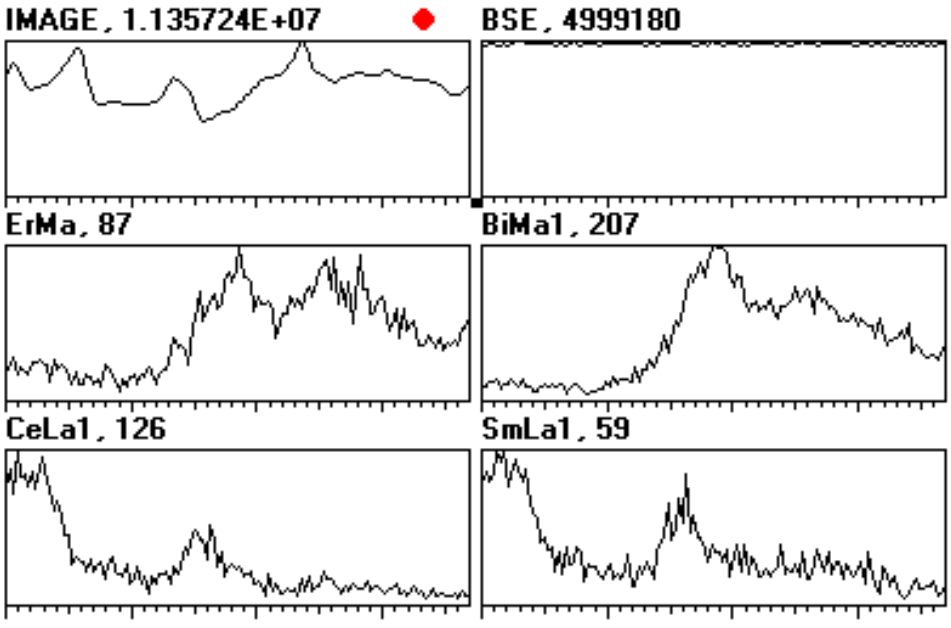

Figure 2-5(b). X-ray line-scan of elements of SDC\ESB sample

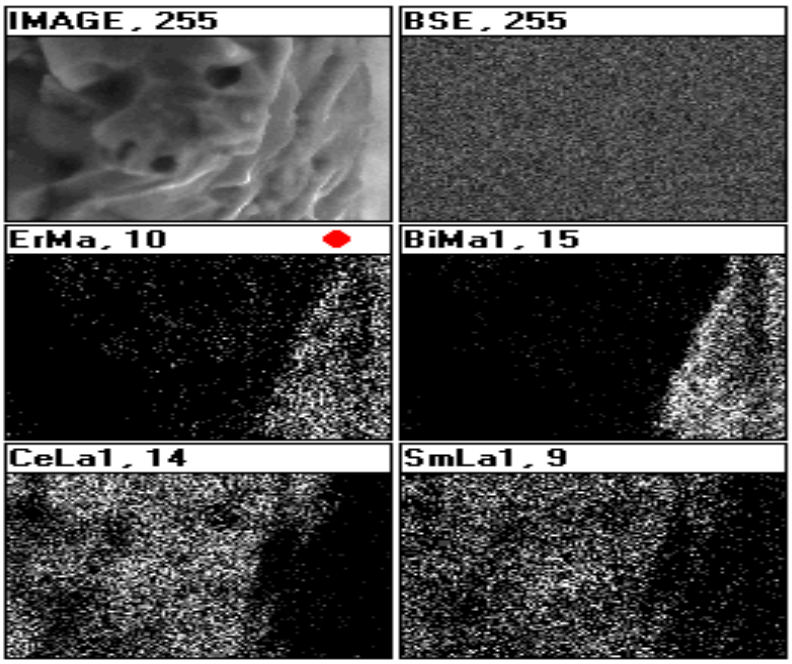

Figure 2-5(c). X-ray map of elements in an SDC\ESB sample (corresponding to Figure 2-5(b))

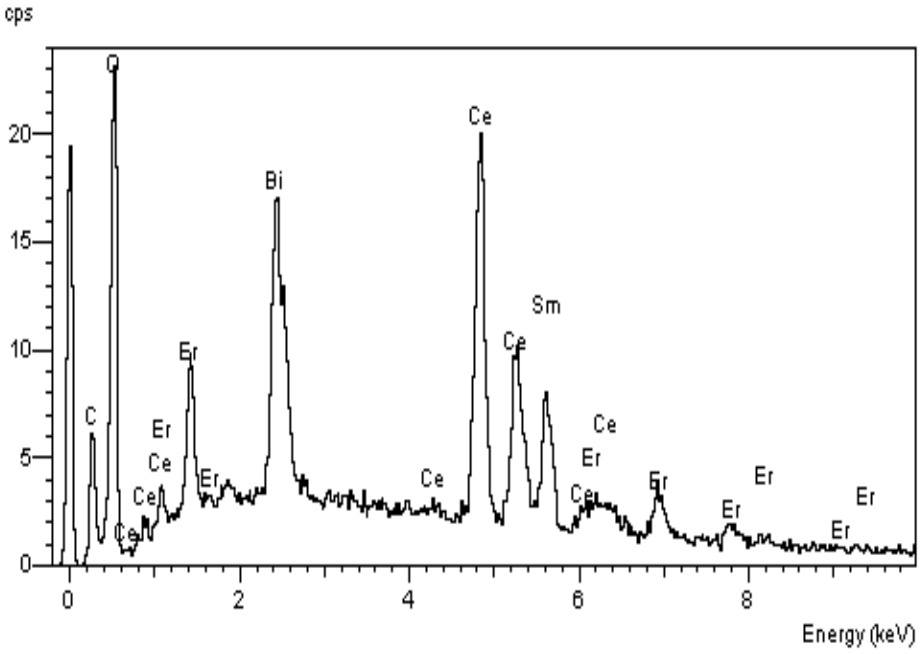

Figure 2-5(d). EDS spectra of the SDC\ESB sample cross-section.

Figure 2-5. The chemical composition of the bilayered SDC\ESB electrolytes estimated from EDS by X-ray line-scan and mapping.

2.2 CONDUCTIVITY OF SDC

2.2.1 Analysis Methods

Electrical impedance spectroscopy (EIS) can be used to measure the bulk, grain-boundary, and electrode conduction processes by analysis of the consecutive semicircles in the complex plane. We used this technique to analyze the grain (or bulk) resistance, R_g, and capacitance, C_g, and the grain-boundary resistance, R_{gb}, and capacitance, C_{gb}, for various temperatures and microstructures. By combining the resistance and capacitance values with appropriate geometric information from the sample, the corresponding conductivities, σ_g and σ_{gb} were derived. This is neither a trivial nor an unambiguous operation, however, and there are currently two prevailing schools of thought that have produced two distinct methodologies namely: the geometric method and the capacitance method. Additional information may be obtained from recent reviews on grain-boundary conductivity and microstructure relations by Steele [19], Virkar *et al.* [20], Hong *et al.* [21], Tian and Chan [22], and Gerhardt and Nowick [23].

2.2.2 Effect of Processing Parameters on SDC

Sintering temperature and density. The ionic conductivity of SDC electrolytes sintered under various conditions was investigated and correlated with the resulting microstructure. Arrhenius plots of the ionic conductivities measured in air are shown in Figures 2-6. The slopes of the Arrhenius plots—obtained by plotting the following equation:

$$\ln \sigma T = \ln \sigma^{\circ} - \frac{E_A}{k_B} \cdot \frac{1}{T} \tag{2.1}$$

—give the activation energy, E_A, for transport of the oxygen ion. In Eq. (2.1), σ° is a pre-exponential factor, k_B is Boltzmann's constant and T is temperature

Figure 2-6 shows that variations in the sintering conditions and density of pellets can change their conductivity by as much as an order of magnitude. In general, the higher densities correspond to higher ionic conductivities. However, the ionic conductivity of 90% density SDC (sintered at 1550°C for 15hrs) is higher than that of 98% density SDC (sintered at 1650°C for 15hrs) in the temperature range 300–800°C. That is, the conductivity increased with sintering temperature and time for the samples sintered below ~1550°C and decreases at higher sintering temperatures. These phenomena are discussed in ensuing sections.

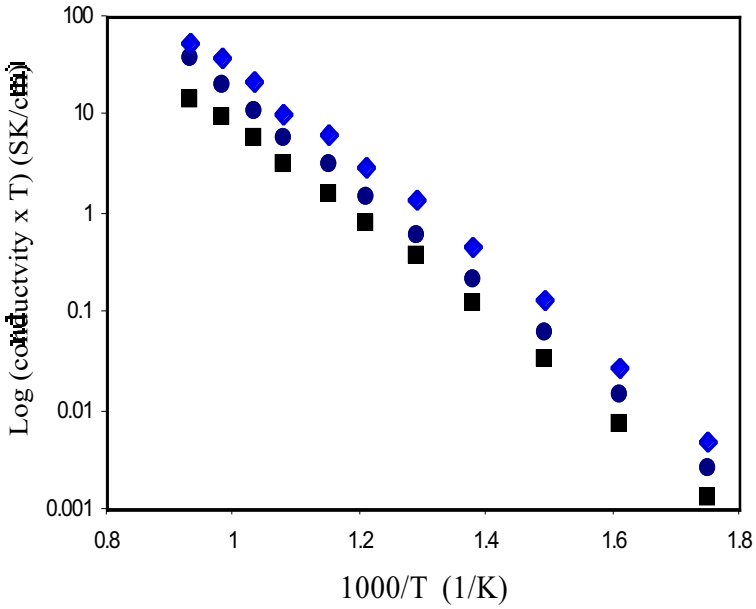

Figure 2-6. Total conductivities, in air, of SDC (uni-axial pressing) samples: (●) density, 97.5%, sintering temperature, 1650°C, (◆) 89.8%, 1550°C, and (■) 70%, 1450°C.

Cold-isostatic pressing. The effect of CIP on SDC samples can be observed by the change in E_A at 650 °C in Figure 2-7. Figure 2-8 shows that this change was brought about by reduced grain-boundary resistance, for T < 650 °C. Cold-isostatic pressing promotes grain growth, which in turn reduces the grain-boundary area (and therefore grain-boundary volume fraction, V_{gb}). Consequently, the contribution of the grain-boundary to the total conductivity, σ_{tot}, decreases. The total conductivity[2] is the sum of the grain (bulk) conductivity, σ_g, and grain-boundary conductivity, σ_{gb}, as shown below:

$$\sigma_{tot} = \sigma_g V_g + \sigma_{gb} V_{gb} \tag{2.2}$$

where V_g is the grain (bulk) volume fraction. It is evident in Eq. (2.2) that if $\sigma_g > \sigma_{gb}$ (true for SDC) then σ_{tot} increases as V_{gb} decreases. Conversely, above 650 °C, Figure 2-7, the effect of a smaller V_{gb} due to CIP is reduced significantly because differences between the values of E_A and σ^0 for σ_g (lower E_A) and σ_{gb} (higher E_A) dominates at higher temperatures.

[2] It is assumed that $\sigma_g > \sigma_{gb}$ and therefore parallel contributions to the total conductivity may be ignored.

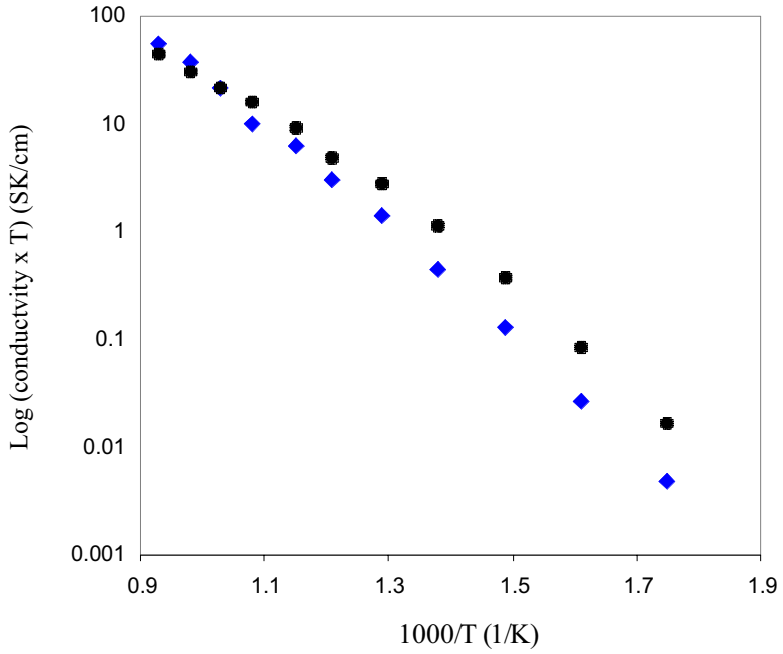

Figure 2-7. Effect of CIP on σ_{tot} for SDC sintered at 1550 °C for 15hrs: (●) CIP and (◆) uni-axial pressing.

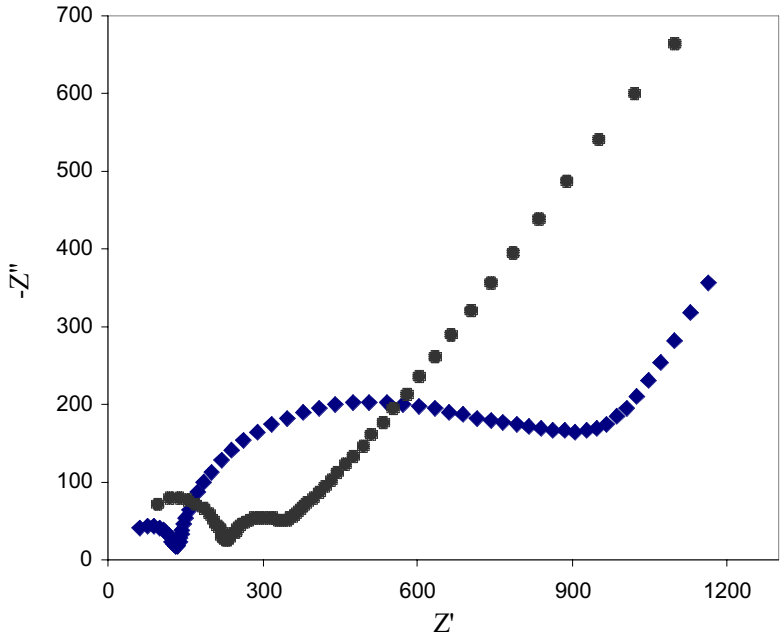

Figure 2-8. Impedance plots for SDC samples at 300 °C; (●) CIP and (◆) uni-axial pressing.

2.2.3 Effect of Grain-Boundary Impurities in SDC

For ceramics, conductivity depends primarily on a variety of microstructural parameters, e.g. grain size and porosity. In particular, grain boundaries have an important effect on the overall conductivity of most ceramic materials and σ_{gb} is affected by factors such as grain size (discussed earlier) and impurity level, among others.

Impurities, including second phases, introduced by the starting materials or during the fabrication procedure have a deleterious effect on σ_{gb} of SDC [19] because they tend to accumulate at grain boundaries during sintering. Various studies [19, 24, 25] have shown that continuous siliceous phases suppress grain growth resulting in small grain-sizes and larger grain-boundary volume fraction (smaller grain volume fraction). Moreover, these impurities provide a blocking layer within the grain-boundary system that makes the grain-boundary region less conductive. Together these effects significantly reduce the ionic conductivity of ceria.

2.2.4 Microstructure

Grain-size distributions were estimated using a linear intercept method. They were found to vary with sintering temperature in the range ~2 to ~15 μm as shown in Table 2-1. Grain-boundary thicknesses were procured from Christie and Berkel [26] whose data was obtained by high-resolution electron microscopy (HREM).

It is observed in Table 2-1 that as the sintering temperature increases so does the grain-size. Since the cations are not mobile until high temperature more than 1500 °C, extensive grain growth occurs above 1500 °C. In addition, high sintering temperatures are needed to ensure a homogeneous distribution of dopants in the sample. This concurs with the notion that cation transport is the limiting step for grain growth [27]. However, low cation mobility in the fluorite lattice means that cation segregation—formed by temperature gradients—may arise at elevated temperatures. Accordingly, it was found that changes in the sintering temperature and time can produce variations in both and bulk and grain-boundary conductivity by more than an order of magnitude. That is, sintering conditions have a significant effect on SDC conductivity.

Table 2-1 Mean Grain Size by Different Sintering Temperatures.

Sintering temperature (°C)	Sintering time (hrs.)	Mean grain size (μm)
1465	15	1.84
1550	15	4.21
1650	15	15.3

2.3 CONDUCTIVITY OF ESB AND DWSB

Impedance using the two probe method was measured with a Solartron 1260 over the frequency range of 0.1 Hz to 1MHz. The frequency response analyzer was interfaced to a computer, and Zplot software and a nulling technique were employed to remove any artifacts caused by inductive responses of the test leads and the equipment. The measurements were taken between 200°C and 800°C in air. The flow rate of air was fixed at 30 sccm. Activation energies were calculated from plots of $\ln(\sigma T)$ vs. 1/T.

Figure 2-9 shows the impedance spectra for 8Dy4WSB at 200 (a), 300 (b) and 500 °C (c). The conductivities were calculated from the values of the bulk resistance measured at the frequency corresponding to the appropriate minima in the complex plots. Both Figure 2-9 (a) and Figure 2-9 (b) show the typical bulk impedance consisting of a single semicircle, and a Warberg-type impedance indicating gas diffusion at the electrode. As the temperature increased (Figure 2-9 (c)), the high frequency semicircle attributable to the bulk resistance could no longer be resolved. The bulk resistance values were then calculated from the high frequency intercept.

The bulk conductivity results are plotted as log σ vs. 1000/T (Figure 2-10). The compositions having 11-13% dopant (10Dy3WSB, 8Dy4WSB and 6Dy5WSB) showed higher conductivity than 17% dopant level (12Dy5WSB, 9Dy8WSB and 5Dy12WSB). A comparison of the conductivity of DyWSB and 20ESB is also shown in Figure 2-10. 20ESB is considered in the literature to have the highest conductivity among the stabilized δ-Bi_2O_3's, with a conductivity at 800 °C, 500 °C and 200 °C of 0.41, 0.021 and 2.8 x 10^{-5} S/cm, respectively. The conductivities of 8Dy4WSB, the highest conductivity composition, at 800 °C, 500 °C and 200 °C are 0.56, 0.043 and 1.4 x 10^{-4} S/cm, respectively, significantly higher than 20ESB, especially in the lower temperature region.

A change in activation energy for some of the compositions was observed, with a lower activation energy above ~600°C and a higher activation energy below ~600°C. As the dopant concentration increases, the disparity between these two activation energies decreases. The observed disparity at ~600°C as a function of dopant concentration is a general trend in stabilized bismuth oxide systems [9]. The activation energy values measured for low and high temperatures with different compositions are shown in Table 1 and 2. From Table 1 and Figure 2-10, it is clear that the lower dopant content compounds (11-13% dopant) showed two different conductivity activation energies. On the other hand, the conductivity of 17% dopant level compositions (Table 2 and Figure 2-10) showed single activation energies, except for 12Dy5WSB that exhibited a slight change in activation energy. This change in activation energy is attributed to an order-disorder transition of the oxygen sublattice [11, 16]. Those compositions

with the greatest disparity have the greatest tendency to order at low temperature [9]. This tendency and the resulting conductivity decay are described in another publication [28].

In Figure 2-11, the conductivity in the WO_3-Dy_2O_3-Bi_2O_3 system is plotted against the dopant composition ratio ($X_{Dy}/(X_{Dy}+X_W)$) content at 500 and 700°C, respectively. Values from the literature were used for comparisons at either end of the dopant composition ratio range (WO_3 stabilized Bi_2O_3 and Dy_2O_3 stabilized Bi_2O_3). 12WSB exhibits the highest conductivity among the phase stable WO_3 compositions [13]. A thermal hysteresis in conductivity was observed at high temperature (650 to 750°C) for samples containing less than 20 mol% WO_3 ($(BiO_{1.5})_{0.89}(WO_3)_{0.11}$) due to the transformation from the monoclinic to the cubic structure. Therefore, the conductivity of 12WSB from Takahashi et al [15] is plotted (closed square) in Figure 2-11.

Verkerk and Burggraaf [16] investigated DySB, in the composition range 5 to 60 mol% Dy_2O_3. The cubic phase for DySB containing 28.5 to 50 mol % Dy_2O_3 was found to be stable over the temperature of measurement (300 to 800°C). The samples with lower Dy_2O_3 content showed a phase transition from cubic to rhombohedral below 800°C and no conductivity data was available. Therefore, values of 28.5DySB are plotted (closed triangle) on the right axis in Figure 2-11 to compare with the doubly doped system, rather than comparing with the concentration range where polyphasic regions appear.

One of the effects of double doping W and Dy is that the cubic structure is stabilized at dopant concentrations less than that necessary for Dy alone. Thus, the cubic structure was stabilized at as little as a 11-13% dopant concentration.

At the higher total dopant concentration (17%), intermediate between the dopant concentration of end compositions from the literature, there appears to be a minimum in conductivity at $X_{Dy}/(X_{Dy}+X_W) = 0.4 - 0.5$ depending on temperature. In contrast, at the lower total dopant concentration (11-13%), more closely matching the dopant concentration of the W end composition, there appears to be a maximum in conductivity at $X_{Dy}/(X_{Dy}+X_W) = 0.5 - 0.6$, depending on temperature. These results indicate the nature of the dopant (W vs. Dy) is as important as the total dopant concentration and that the effect of double doping on conductivity is “non ideal.” The observed differences in conductivity dependence on dopant ratio warrants further investigation.

In summary, the conductivity of Dy_2O_3 and WO_3 stabilized Bi_2O_3 was studied. These cations were selected for their high polarizability in order to achieve a stable disordered anion lattice and a high mobility. By double doping we were able to obtain compositions (11-17% dopant) that were cubic, when single dopants would not stabilize the cubic structure at this low

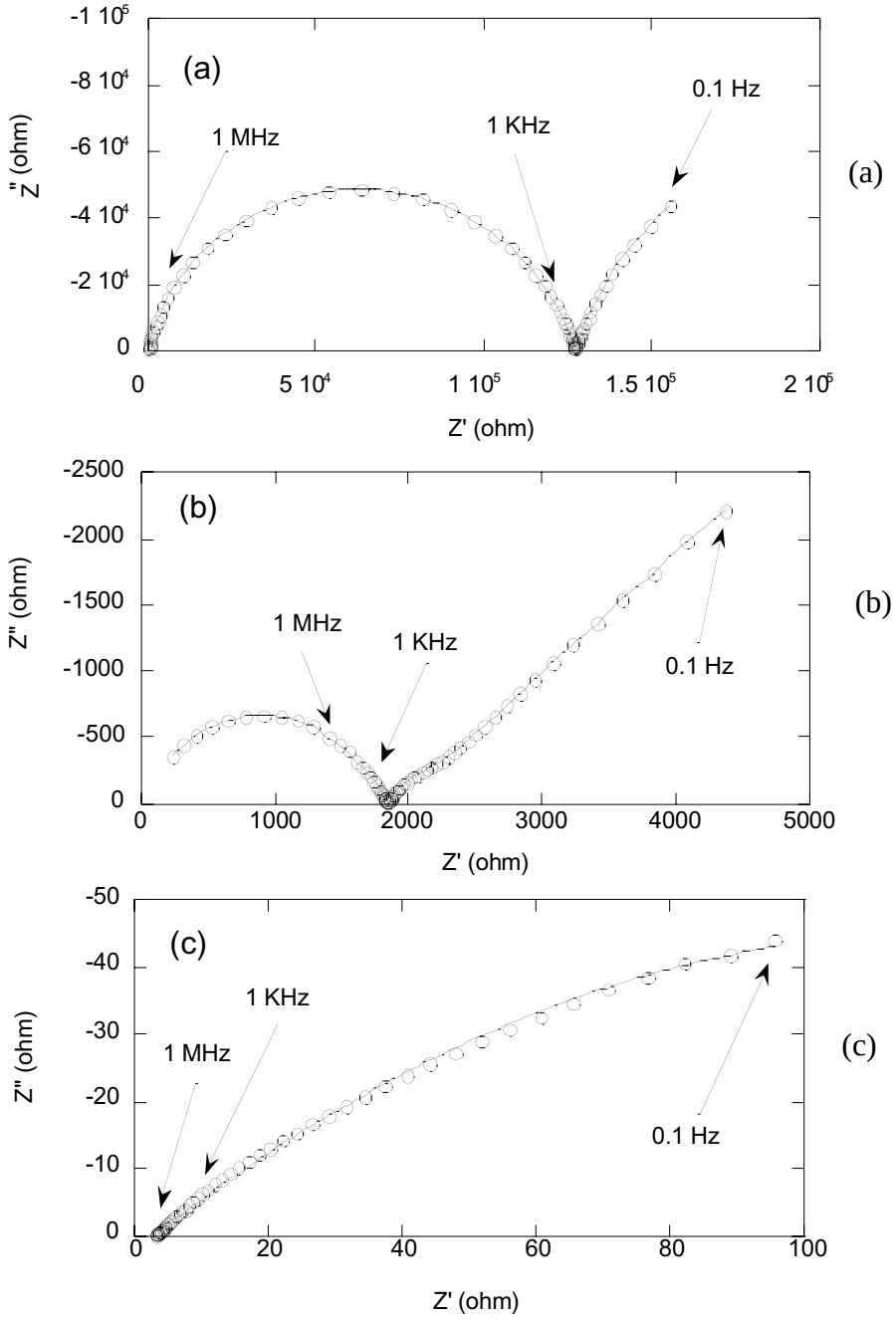

Figure 2-9. Impedance spectra for 8Dy4WSB with Au electrodes in air at (a) 200°C (b) 300°C and (c) 500°C.

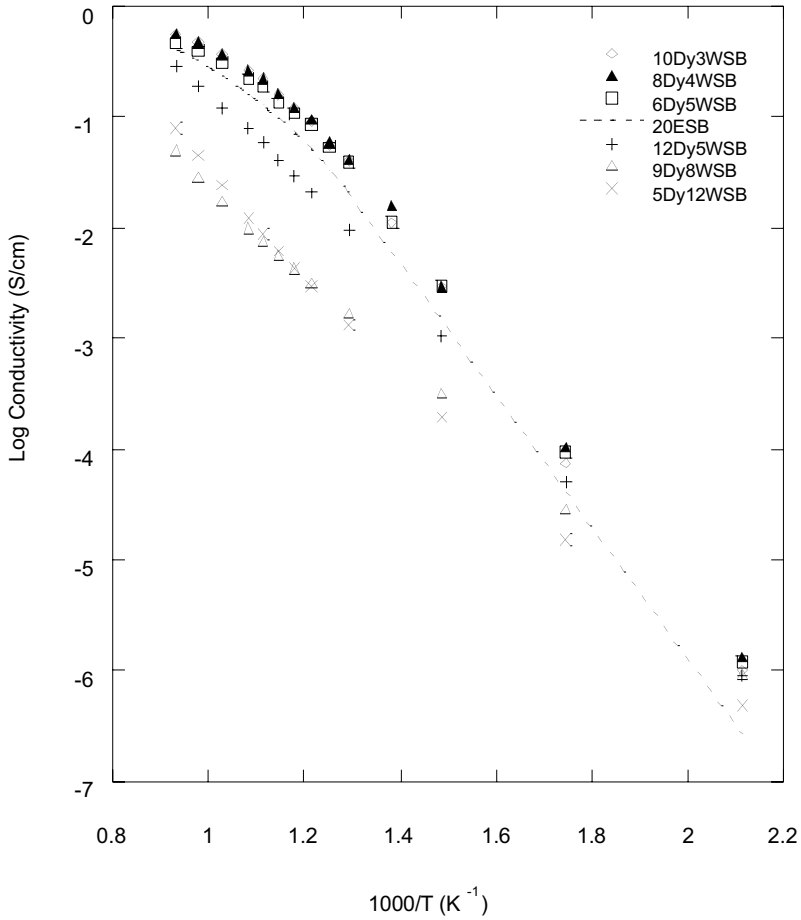

Figure 2-10. Arrhenius plot of conductivities for 10Dy3WSB, 8Dy4WSB, 6Dy5WSB, 12Dy5WSB, 9Dy8WSB, 5Dy12WSB and 20ESB

Table 1. Conductivity activation energies of 11 – 13% total dopant compositions

Composition	Low Temperature (< 600 °C) E_A (eV)	High Temperature (> 600 °C) E_A (eV)
6Dy5WSB	0.47	0.23
8Dy4WSB	0.47	0.29
10Dy3WSB	0.48	0.19

Table 2. Conductivity activation energies of 17% total dopant compositions

Composition	Low Temperature (< 600 °C) E_A (eV)	High Temperature (> 600 °C) E_A (eV)
5Dy12WSB	0.39	0.39
9Dy8WSB	0.34	0.34
12Dy5WSB	0.42	0.34

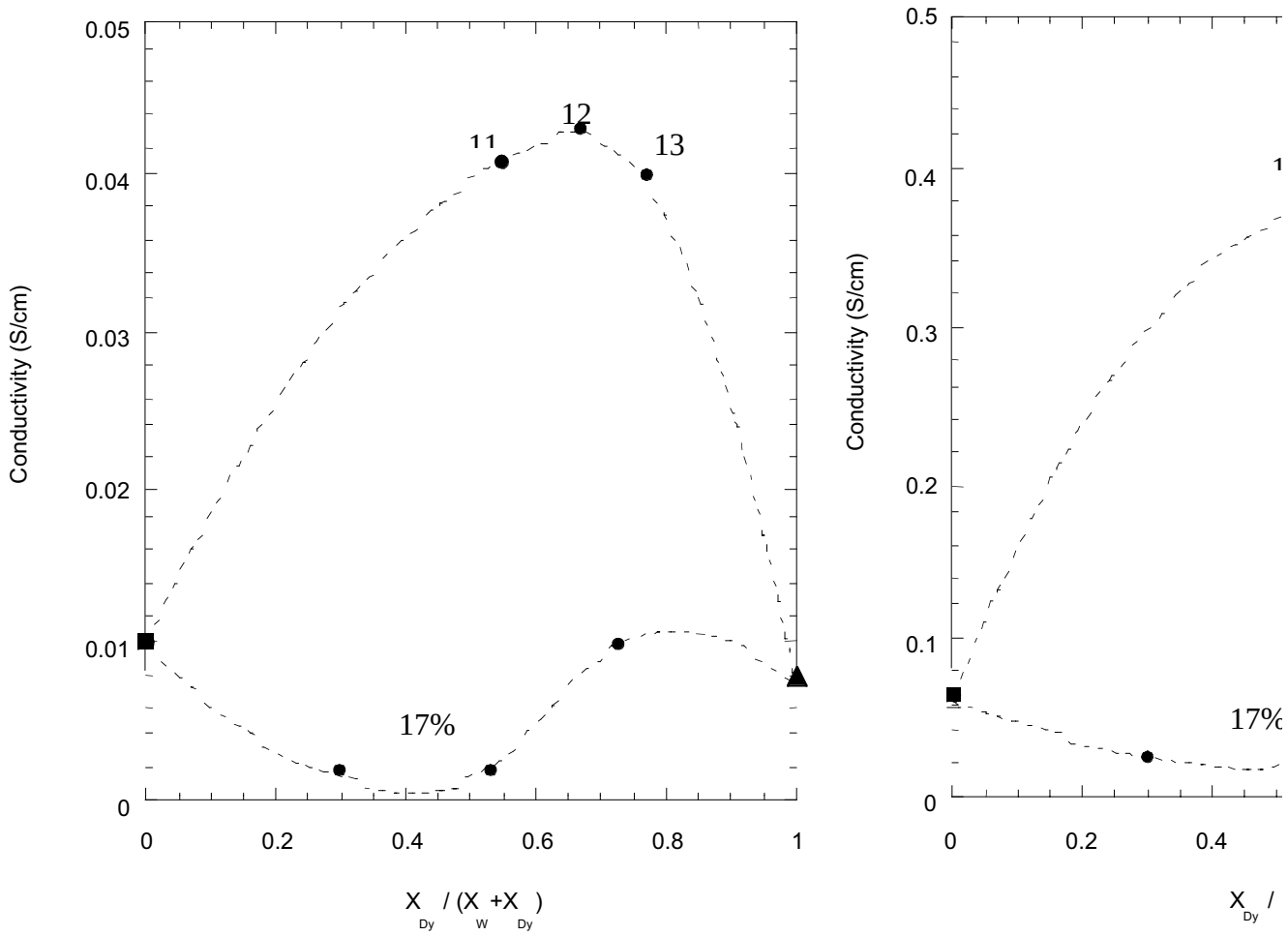

(a)

Figure 2-11. Conductivity as a function of dopant composition ratio ($X_{Dy}/(X_{Dy}+X_W)$) and total dopant concentration at **(a)**500°C and **(b)**700°C. The conductivity of 12WSB (Takahashi et al [15], closed square) and 28.5DySB (Verkerk et al [16], closed triangle) is given as a reference at either end of the range.

of a dopant level. The resultant cubic DyWSB′s had high conductivity. In particular, the composition 8Dy4WSB had a conductivity significantly greater than 20ESB, rating it **the most conductive oxide electrolyte currently known**.

2.4 CONDUCTIVITY OF SDC\ESB BILAYERS

The *effective*[3] conductivities of SDC\ESB sample (ESB film thickness: ~0.2 μm) were measured in air by EIS. Figure 2-12 shows that the *effective* conductivity of the SDC\ESB bilayer was higher than that of single layer SDC (fabricated by CIP or uniaxial pressing) for 600 °C < T < 800 °C despite the relative thinness of the ESB layer—i.e., $\sigma_{SDC\backslash ESB} > \sigma_{SDC(CIP)} > \sigma_{SDC(uniaxial)}$. This result also suggests that a low conductivity (relative to SDC and ESB) phase is not formed at the SDC-ESB interface. Nevertheless, because of the thinness of the ESB layer, the increase in the *effective* conductivity of the bilayer over the SDC single layer is somewhat surprising and may allude to the formation of a higher conductivity ESB phase in the grain-boundary area of SDC. This is speculative, however, and requires further research for confirmation.

The change in E_A for the conductivity of the SDC\ESB sample, seen at 600°C in Figure 2-12, may be attributed to the order-disorder transition in the oxygen sublattice of ESB at 600°C [29, 30]. We have studied this and the time dependent ageing phenomenon in phase-stabilized bismuth oxides extensively [29, 30].

Activation energies and pre-exponential factors for SDC and SDC\ESB electrolytes are listed in Table 2-2 and they are in good agreement with Tian and Chan [22], and Wang *et al.*'s results [31]. An inspection of Table 2-2 shows that activation energies and pre-exponential factors obtained by the capacitance method [19 - 23] were larger than those obtained by the geometric method [19 - 23].

A similar difference between the two methods was observed by Tian and Chan [22]. The difference between the values of the activation energy and pre-exponential terms, obtained from the capacitance and geometric methods, most likely arises from the inaccuracy in the assumed values of grain size and grain-boundary thickness used in the geometric method [19 - 23].

[3] Conductivity is an intrinsic material property, independent of sample geometry. Hence a bilayer does not have a true conductivity. The term *effective* conductivity is used here to describe a hypothetical material with a conductivity that is equivalent to the bilayer.

Table 2-2. Activation energies and pre-exponential factors of various SDC and SDC\ESB samples.

Sample thickness; (cm)	Relative Density (%)	CIP	T_{sinter} (°C)	Conductivity Type	Activation energy (eV)	Pre-exponential (SK/cm)
SDC (0.172)	97.5	No	1650	Total	0.99(3)	2.0×10^5
				Bulk	0.85(1)	2.0×10^6
				Grain (G) [1]	1.0(11)	2.5×10^4
				Grain (C) [2]	1.7(01)	4.0×10^8
SDC (0.183)	89.5	No	1550	Total	0.97(5)	3.0×10^6
				Bulk	0.86(9)	3.0×10^6
				Grain (G)	1.0(54)	1.8×10^4
				Grain (C)	1.8(65)	1.0×10^{11}
SDC (0.145)	70.0	No	1465	Total	0.97(7)	6.8×10^5
				Bulk	0.75(8)	1.3×10^5
				Grain (G)	1.0(57)	7.7×10^4
				Grain (C)	1.8(65)	1.0×10^{11}
SDC (0.171)	90.4	Yes	1550	Total [3]	0.97(0)	6.0×10^6
				Total [4]	0.66(5)	2.0×10^7
				Bulk	0.77(7)	3.8×10^5
				Grain (G)	0.98(4)	2.5×10^4
				Grain (C)	1.7(53)	1.0×10^{11}
SDC\ESB ($0.17\backslash 2 \times 10^{-5}$)	90.4	Yes	1550	Total [3]	1.0(39)	2.0×10^7
				Total [4]	0.66(5)	6.0×10^4
				Bulk	0.91(8)	5.0×10^6
				Grain (G)	0.91(3)	8.0×10^3
				Grain (C)	1.8(65)	1.0×10^{11}

1. Grain (G): grain-boundary conductivity obtained by using geometrical method.
2. Grain (C): grain-boundary conductivity obtained by using grain and grain-boundary capacitance
3. Total: total conductivity in temperature range between at 300 °C and 500 °C.
4. Total: total conductivity in temperature range between at 500 °C and 800 °C.

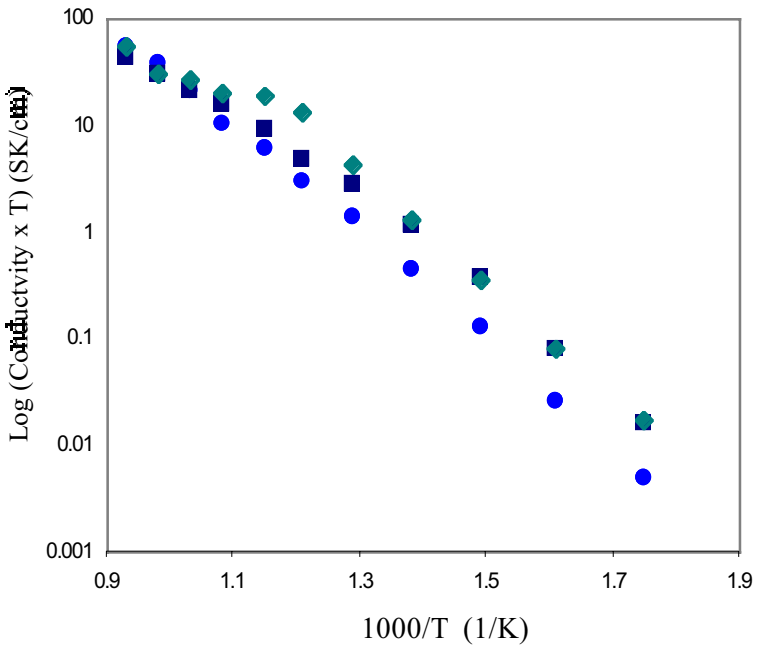

Figure 2-12. Total conductivity, in air, of (●) SDC (density: 90%, uni-axial pressing, sintered at 1550 °C), (■) SDC (90%, CIP, 1550 °C) and (◆) SDC\ESB (90%, CIP).

2.5 FABRICATION OF ANODE-SUPPORTED CERIA ELECTROLYTES BY COLLOIDAL DEPOSITION

Investigation into the effect of relative thickness of ceria-bismuth oxide bilayers can be facilitated by electrode-supported electrolytes, as fabrication of the bilayers requires some ingenuity due to the large difference in the sintering temperatures of bismuth oxide and ceria. As a first step, the fabrication and performance of Ni-gadolinium doped ceria (GDC) anode supported GDC thick film electrolyte, using a colloidal deposition method is being reported here. Future work involves depositing doped bismuth oxide layer on the GDC coated anode substrates, to form anode supported bilayer electrolytes and electrochemical characterizations on them. An anode supported electrolyte cell was preferred over a cathode supported electrolyte cell as the anode polarization is, in general, smaller than the cathode polarization. GDC as the ceramic component in the anode will lead to an enhanced performance, as under the reducing conditions at the anode GDC is a mixed ionic electronic conductor and the reaction zone will not be restricted to the interface of the anode and the electrolyte.

Microstructure plays an important role in the performance of the electrodes, as shown in a recent work by Ohara et al [32]. They studied the performance of Ni-Samaria doped Ceria

cermet anodes as a function of Ni content and found that at 800°C, the lowest anodic polarization (~30mV) was achieved for a cermet with a Ni content of around 50vol% at a current density of 300mA/cm^2. Thus, in this work a NiO-GDC anode was fabricated with Ni content of 50vol%. Reduction of NiO to Ni was accomplished in situ in the cell, which would generate ~26% porosity in the structure.

Several techniques have been developed for depositing thick films on substrates from vapor deposition techniques (CVD/EVD) and pulse laser deposition (PLD) to chemical routes (sol-gel) among others [33]. However, colloidal deposition has definite advantages over these techniques in its simplicity, cost-effectiveness, upscability and flexibility (thickness ranging from 10-100μm can be deposited). Also, exceptional performance has been reported for SOFCs fabricated from colloidal deposition technique by de Souza et al. using a 10μm thick YSZ electrolyte [34].

2.5.1 Experimental

11mol% GDC powder (GDC d_{50}=0.64um) from Rhodia and NiO powder from Alfa-Aesar were mixed and ball milled for 24 hours with Zirconia ball media in Ethanol. The mixed NiO-GDC powder was pressed uniaxially at pressures of 39.3 MPa to form discs of 1.25 inches diameter. The green bodies were then pre-sintered at temperatures between 800°C to 1100°C, to coarsen the microstructure and to provide strength for further processing steps.

For the colloidal suspensions, 10g of GDC powder was mixed in 100ml of Iso-propyl alcohol (IPA). Poly-vinyl Butyral (PVB) in ethanol was added to the solution as binder, equal to 5wt% of the oxide powder. The suspension was sonicated in an ultrasonic bath to disperse the GDC powder, with intermittent stirring. The GDC electrolyte layer was deposited on the pre-sintered NiO-GDC discs by dip-coating and finally sintered at 1600°C and 1650°C. Multiple coating was done to get thicker films.

The pre-sintering and final sintering temperatures were varied to find the optimum combination at which the densification rate of the GDC film matches with the shrinkage rate of the NiO-GDC anode substrate. This helps in keeping the film under compression rather than in tension and hence, avoids the cracking of the film due to stress built up by the 2-D confinement during sintering.

The diameters of the anode discs were measured after each processing step to calculate the shrinkage profile. The density of the discs was measured using the Archimedes's principle. The coated substrate was characterized by XRD (APD-4720) and SEM (JEOL-6400) techniques.

The percentage porosity of the GDC films was measured by stereological counting methods using point probes.

2.5.2 Results and Discussion

The representative microstructures of the ceria film with the anode substrates pre-sintered at 800C, 850°C, 900°C, 1000°C, 1100°C for 4 hours, and after coating finally sintered at 1600°C for 6 hours and 1650°C for 10 hours are show in Figure 2-13(a)-(e) and Figure 2-14(a)-(e), respectively. Figure 2-15 shows the shrinkage profile of the NiO-GDC substrate during sintering. The density of the anode substrate was calculated to be 6.72 gm/cc (~98% of the theoretical density) after sintering at 1600°C. Figure 2-16 shows the percentage porosity of the GDC film under different sintering profiles. The volume fraction of the porosity in the microstructure is calculated by taking the average fraction of points on a grid, lying on the pores. Figure 2-17 shows the cross-sectional SEM of the film pre-sintered at 900°C for 4 hours and finally sintered at 1600°C for 6 hours. The thickness of the film was about 10μm after 4 coats.

For applications in SOFCs, the electrolyte needs to be highly dense to act as a barrier for the fuel gases and air. As can be seen from Figure 2-16, varying the pre-sintering temperatures lead to minima in porosity at 850°C for both the final sintering temperatures of 1600°C and 1650°C, with values of 1.38% and 1.48% respectively. Therefore, after pre-sintering at 850°C, the shrinkage rate of the anode matches the densification rate of the film. However, as can be seen in the Figure 2-14, sintering at 1650°C leads to coarsening of the microstructure. Both the grain and pore size increase and become almost the double the size to that sintered at 1600°C. Bigger pore size in the electrolyte microstructure has larger chances of failure in partitioning the fuel and air atmospheres in comparison. Also, thermodynamic studies on film stability have shown that, the film thickness should be larger than the grain size of the film [35]. Otherwise, the film would lower its energy by breaking into isolated islands and exposing the substrate. Hence, it was decided to work with films pre-sintered at 850°C and finally sintered at 1600°C for OCP and I-V measurements. Figure 2-17 shows the cross-sectional SEM of the film pre-sintered at 850°C for 4 hours and finally sintered at 1600°C for 6 hours, after being tested in a fuel cell for over 200 hours showing the reduced porous anode and the dense Ceria layer.

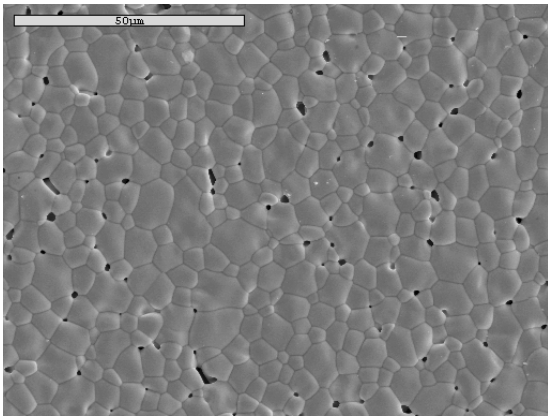

(a)800°C,4 hrs /1600°C,6 hrs

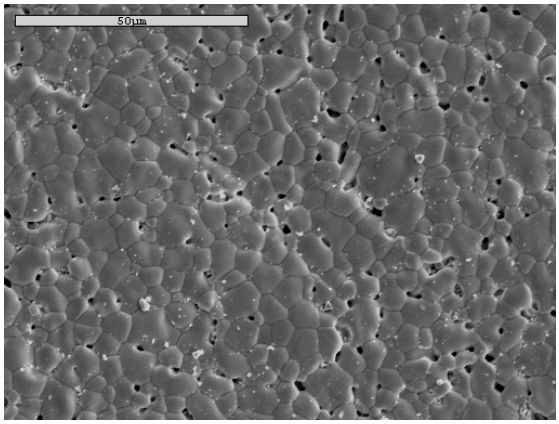

(b)850°C,4 hrs /1600°C,6 hrs

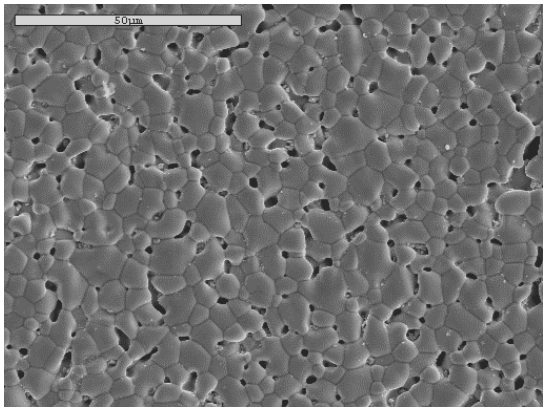

(c) 900°C,4 hrs /1600°C,6hrs

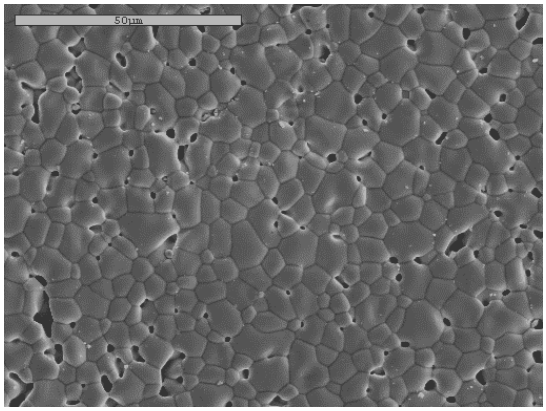

(d)1000°C,4 hrs /1600°C,6 hrs

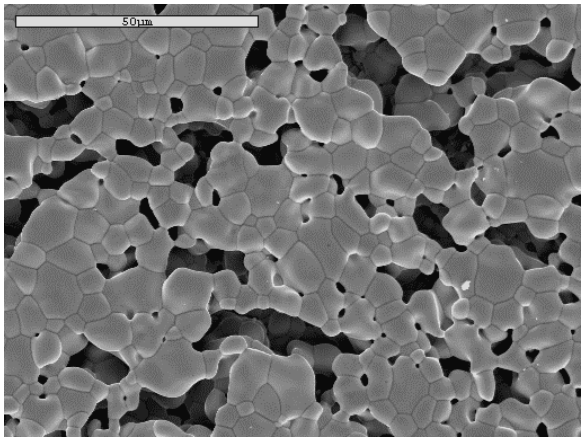

(e) 1100°C,4 hrs /1600°C,6 hrs

Figure 2-13 (a)-(e): Representative microstructures of the Ceria film under different sintering conditions. (Pre-sintering condition /Final Sintering condition)

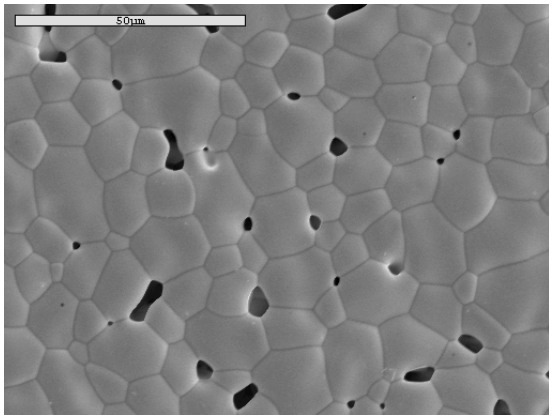

(a) 800°C,4 hrs /1650°C,10 hrs

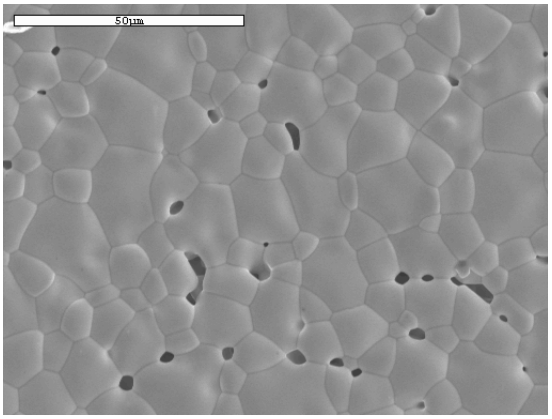

(b) 850°C,4 hrs /1650°C,10 hrs

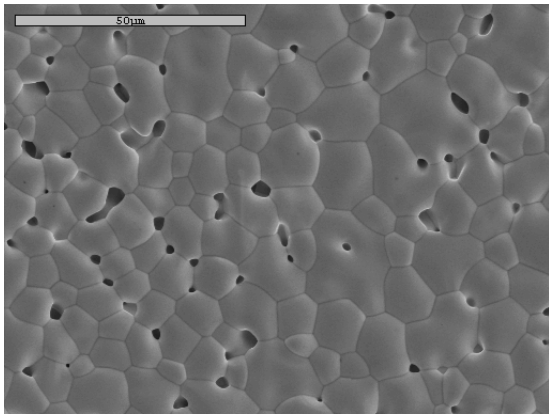

(c) 900°C,4 hrs /1650°C,10 hrs

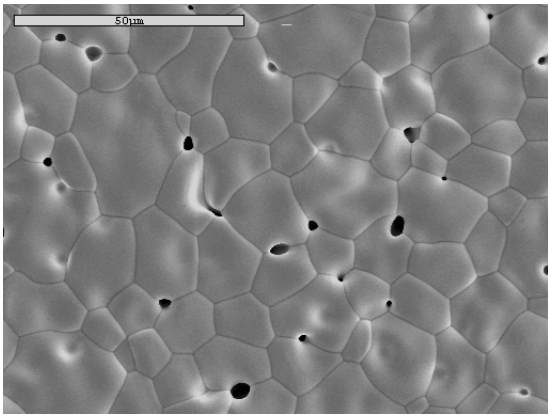

(d) 1000°C,4 hrs /1650°C,10 hrs

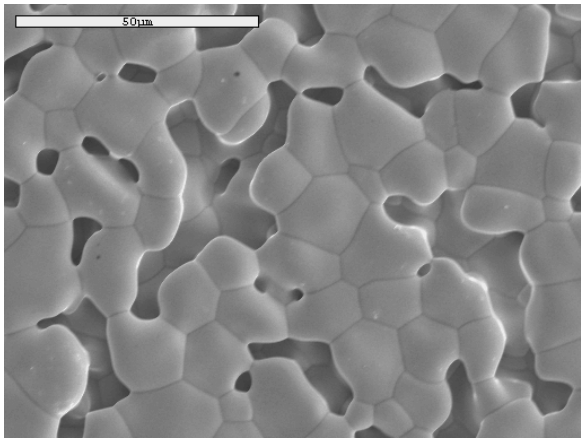

(e) 1100°C,4 hrs /1650°C,10 hrs

Figure 2-14 (a)-(e): Representative microstructures of the Ceria film under different sintering conditions. (Pre-sintering condition/Final Sintering condition).

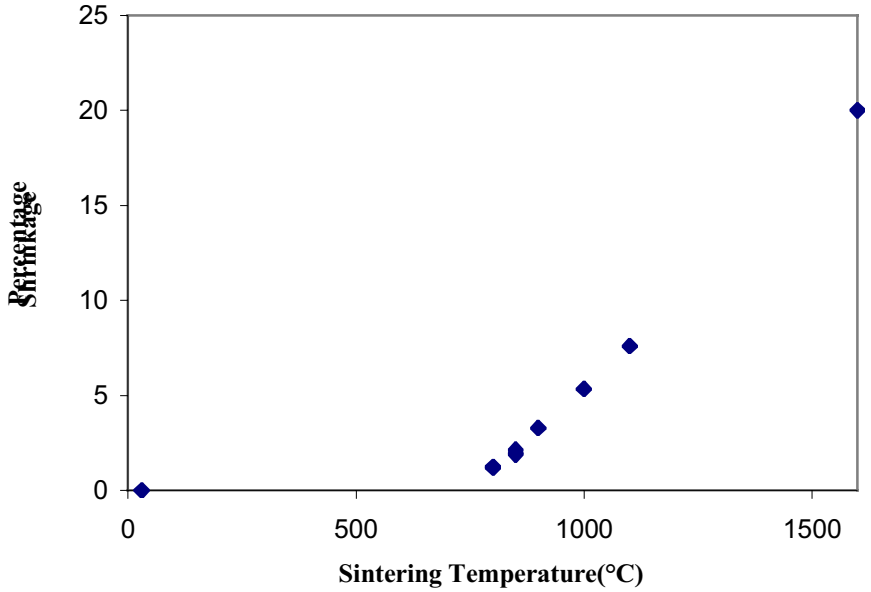

Figure 2-15. Shrinkage profile of the NiO-GDC anode with sintering temperature.

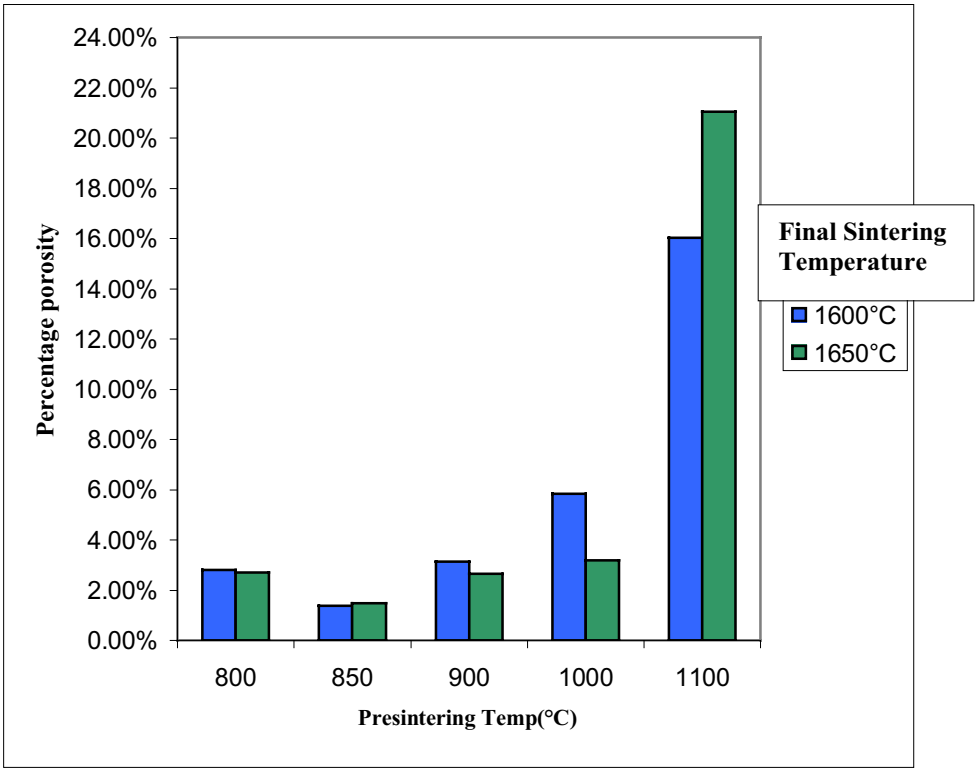

Figure 2-16. Porosity in the Ceria film as a function of the pre-sintering and final sintering temperature of the anode.

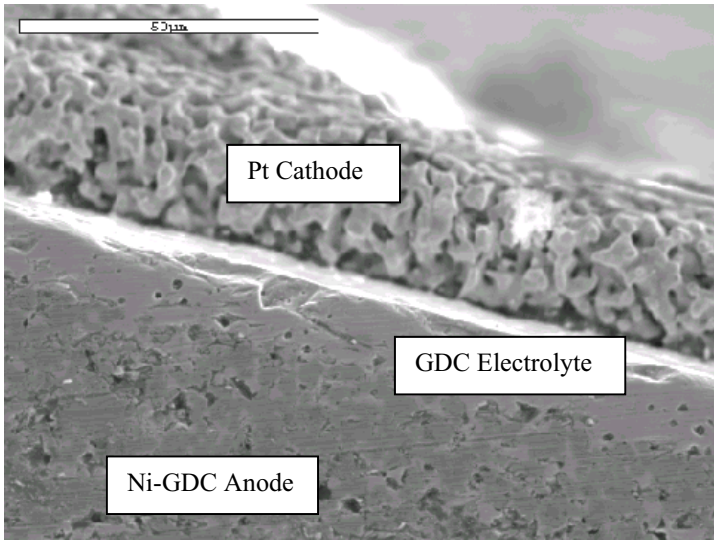

Figure 2-17. Cross-sectional SEM of the film pre-sintered at 850°C for 4 hours and finally sintered at 1600°C for 6 hours, after being tested in a fuel cell for over 200 hours.

3. ANALYTICAL MODEL FOR DEFECT DISTRIBUTION AND TRANSPORT IN OPEN-CIRCUIT CONDITIONS

In this section, the *open-circuit* electrochemical performance (i.e., the *open-circuit* potential, Φ_{oc}) of SOFCs is modeled with specific reference to (single layer) SDC-based SOFCs. The model is evaluated by fitting it to the experimental data presented in the next section (section 4). Previous modeling work used a "thermodynamic approach" to develop equations for defect concentration dependence on P_{O_2} (i.e., defect equilibria). Since then a "transport approach" has been developed [36] from the fundamental transport laws and is the method presented below. The approach has proved more versatile in describing transport phenomena and is derived with fewer assumptions than the previous "thermodynamic approach".

To lay the groundwork for deriving the model, the definitions of relevant transport properties and transport laws are given first. Next, the open-*circuit* spatial concentration distribution of defects in an MIEC in an oxygen potential gradient is derived and expressions for the defect concentration dependence on P_{O_2} are cited from previous work [36]. Expressions for Φ_{oc} are then derived from the "thermodynamic approach" (based on earlier work [36]) and the "transport approach" (based on the work presented here).

Finally, to close this section, the evaluation of the mass action constant for the external equilibrium reaction, K_r, and the effect of defect association are explored. The evaluation of this

important constant is an extension of our previous work [36] and part of an ongoing effort to find methods through which K_r may be determined accurately. Secondly, we are interested in the effects defect association may have on the performance of oxide mixed conductors.

3.1 DEFINITIONS AND LAWS

The first transport property of interest is the conductivity of the *i*th species, σ_i, defined as:

$$\sigma_i = z_i^2 q^2 \frac{D_i}{k_B T} c_i \tag{3.1}$$

where z is charge number, q is the elementary charge on an electron, k_B is Boltzmann's constant, T is temperature, D is diffusivity and c is concentration. The total conductivity, σ_{tot}, of the MIEC is then the sum of all the *i*th conductivities, written as

$$\sigma_{tot} = \sum_i \sigma_i \tag{3.2}$$

A related and useful transport property is the transference number of the *k*th defect species, t_k,—$k \in \{1, 2,..., i\}$, the set of i defects—which is given by:

$$t_k = \frac{\sigma_k}{\sigma_{tot}} = \frac{\sigma_k}{\sum_i \sigma_i} \tag{3.3}$$

The relevant transport laws are given in the next three equations. Firstly, the flux density of the *i*th species, j_i is given by:

$$j_i = -D_i \nabla c_i - z_i D_i c_i f \nabla \phi = -z_i^{-2} q^{-2} \sigma_i \nabla \tilde{\mu}_i \tag{3.4}$$

where $f = q/k_B T$. The electrochemical potential $\tilde{\mu}_i$ of the *i*th defect species is given by

$$\tilde{\mu}_i = \mu_i + z_i F \phi = k_B T \ln c_i + z_i q \phi \tag{3.5}$$

where μ is the chemical potential and is defined for, electrically charged, defect species as

$$\mu_i = k_B T \ln c_i \tag{3.6a}$$

For, electrically neutral, gaseous species μ is defined as

$$\mu_i = k_B T \ln P_{X_\xi} \tag{3.6b}$$

where P_{X_ξ} is the partial pressure of the gas X with stoichiometry, in the standard state, ξ.

Secondly, the current density, J, is the sum of the current density contributions of each ith defect species, J_i, and given by:

$$J = \sum_i J_i = q \sum_i z_i j_i \tag{3.7}$$

Finally, the material balance for the ith species may be stated as

$$\partial c_i / \partial t = -\nabla j_i + \Gamma_i \tag{3.8a}$$

where t is time and Γ_i, often referred to as *production*, is the rate of the formation of the ith species due to homogenous chemical reactions in the bulk (i.e., not at the electrode surfaces). It is assumed that the system under consideration is at steady state (i.e., $\partial c_i/\partial t = 0$) and that all chemical reactions take place at the electrode surfaces (i.e., $\Gamma_i = 0$). Thus, Eq. (3.8a) reduces to:

$$\nabla j_i = 0 \tag{3.8b}$$

In other words, j_i is independent of position.

By definition [37], the *open-circuit* potential across the fuel cell, Φ_{oc}, is given by

$$\Phi_{oc} = \tfrac{1}{2} z_V^{-1} q^{-1} \int_{\mu_{O_{2_0}}}^{\mu_{O_{2_L}}} t_{ion} \cdot \mathrm{d}\mu_{O_2} = \tfrac{1}{2} z_V^{-1} q^{-1} \int_{P_0}^{P_L} t_{ion} \cdot \mathrm{d} \ln P \tag{3.9a}$$

where P is oxygen partial pressure, the subscript "V" refers to oxygen vacancies and the subscripts "0" and "L" refer to conditions on either side of the fuel cell, at $x = 0$ and $x = L$.

Alternatively, if the spatial dependence of the defect species is known, then Eq. (3.9a) may be written as

$$\Phi_{oc} = \tfrac{1}{2} z_V^{-1} q^{-1} \int_0^L t_{ion} \left(\mathrm{d}\mu_{O_2} / \mathrm{d}x \right) \cdot \mathrm{d}x \tag{3.9b}$$

where x is the spatial ordinate.

3.2 DEFECT DISTRIBUTION IN OPEN-CIRCUIT CONDITIONS

Defect transport in open-circuit conditions—$J = 0$, $\nabla\phi = 0$ and $\nabla c_i \neq 0$—is crucially different, see Figure 3-1, from defect transport in closed-circuit conditions—$J \neq 0$ and $\nabla\phi \neq 0$. In closed-circuit conditions the defect mobilities are independent of each other because $J \neq 0$ and there is a net transport of charge across the MIEC. In open-circuit conditions, however, $J = 0$ and there is no net transport of charge across the MIEC. The absence of net charge transport implies that the charge carrying species must diffuse simultaneously in a ratio that fulfills the requirement of zero charge transport (i.e., the defect mobilities are no longer independent of each other). This phenomenon is known as ambipolar diffusion.

Therefore, for an MIEC in open-circuit conditions, Eqs. (3.4) and (3.8) reduce to

$$j_i = -D_{ambi}\nabla c_i \tag{3.10}$$

and

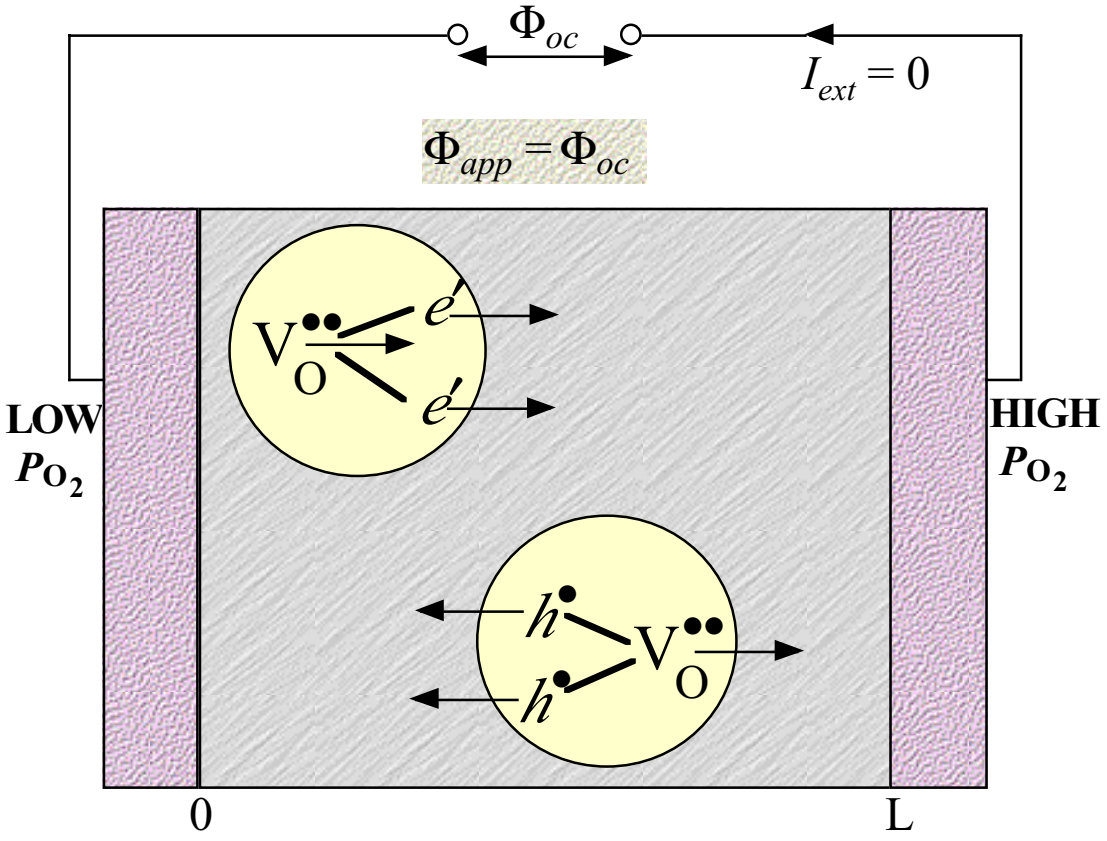

Figure 3-1. Ambipolar defect flux in an SOFC in *open-circuit* conditions.

$$\nabla j_i = -D_{ambi} \nabla^2 c_i = 0 \tag{3.11}$$

Given the usual boundary conditions—at $x = 0$, $c_i = c_{i_0}$ and at $x = L$, $c_i = c_{i_L}$—then the solution of the second-order differential equation in Eq. (3.11) is

$$c_i(x) = \left(c_{i_L} - c_{i_0}\right)\frac{x}{L} + c_{i_0} \tag{3.12}$$

Finally, if the effects of the double layer at the electrode-electrolyte interface may be ignored, then the boundary values of the defect concentrations are set by a combination of the charge balance and the defect equilibrium equation that governs the oxide's equilibrium with the gas phase. The charge balance equation for an acceptor-doped *n*-type oxide MIEC, like samaria-doped ceria or gadolinia-doped ceria, is given by

$$z_V c_V + z_e c_e + z_A c_A = 0 \tag{3.13}$$

where the subscripts "*A*" and "*e*" refer to the acceptor dopant and electron respectively. While the oxide-oxygen gas equilibrium reaction is given by

$$\mathrm{O_O^\times} \leftrightarrow \mathrm{V_O^{\bullet\bullet}} + 2e' + \tfrac{1}{2}\mathrm{O_2} \qquad\qquad K_r = c_V c_e^2 P^{\frac{1}{2}} \tag{3.14}$$

where K_r is the mass action constant for the external equilibrium reaction. Eqs. (3.13) and (3.14) constitute a pair of simultaneous equations which can be solved (for the defect concentration dependence on oxygen partial pressure) numerically [38, 39] or, as we have shown previously [36], through analytical modeling. From our earlier modeling of the defect concentration dependence on oxygen partial pressure in ceria and other MIECs [36], we have:

$$c_V(P) = \left[\tfrac{3}{4}K_r^{\frac{1}{2}}P^{-\frac{1}{4}} + \left(\tfrac{1}{2}c_A\right)^{\frac{3}{2}}\right]^{\frac{2}{3}} \tag{3.15}$$

and

$$c_e(P) = K_r^{\frac{1}{2}}P^{-\frac{1}{4}}\left[\tfrac{3}{4}K_r^{\frac{1}{2}}P^{-\frac{1}{4}} + \left(\tfrac{1}{2}c_A\right)^{\frac{3}{2}}\right]^{-\frac{1}{3}} \tag{3.16}$$

Through substitution of the oxygen partial pressure values at the boundaries ($x = 0$ and $x = \mathrm{L}$) of an MIEC in a fuel cell setup (see Figure 3-1), the boundary defect concentrations, c_{i_0} and c_{i_L}, may be determined from Eqs. (3.15) and (3.16).

3.3 OPEN-CIRCUIT POTENTIAL

From the equations developed (and cited) in the two immediately preceding sections, we are now ready to obtain expressions for Φ_{oc} of an SOFC. There are two approaches that may be used to derive equations for Φ_{oc}. The first combines Eqs. (3.1), (3.2), (3.3), (3.6b), (3.9), (3.15) and (3.16) with the result (since $z_V = 2$ and $z_e = -1$):

$$f \cdot \Phi_{oc} = \frac{1}{4}\int_{P_0}^{P_L} \frac{\mathrm{d}\ln P}{1+\Theta K_r^{\frac{1}{2}} P^{-\frac{1}{4}}\left[\frac{3}{4}K_r^{\frac{1}{2}}P^{-\frac{1}{4}} + \left(\frac{1}{2}c_A\right)^{\frac{3}{2}}\right]^{-1}} = \frac{1}{4}\ln\frac{P_L}{P_0} - \ln\frac{\left(\frac{3}{4}+\Theta\right)K_r^{\frac{1}{2}}P_0^{-\frac{1}{4}} + \left(\frac{1}{2}c_A\right)^{\frac{3}{2}}}{\left(\frac{3}{4}+\Theta\right)K_r^{\frac{1}{2}}P_\mathrm{L}^{-\frac{1}{4}} + \left(\frac{1}{2}c_A\right)^{\frac{3}{2}}}$$

$$= f \cdot \Phi_{th} - \ln\frac{\left(\frac{3}{4}+\Theta\right)K_r^{\frac{1}{2}}P_0^{-\frac{1}{4}} + \left(\frac{1}{2}c_A\right)^{\frac{3}{2}}}{\left(\frac{3}{4}+\Theta\right)K_r^{\frac{1}{2}}P_\mathrm{L}^{-\frac{1}{4}} + \left(\frac{1}{2}c_A\right)^{\frac{3}{2}}} \qquad (3.17)$$

where Φ_{th} is the theoretical (Nernst) potential and

$$\Theta = \frac{z_e^2 D_e}{z_V^2 D_V} \qquad (3.18)$$

which is a constant dependent on the ratio of the electron diffusivity, D_e, to the vacancy diffusivity, D_V.

An alternative approach combines Eqs. (3.1), (3.2), (3.3), (3.6a), (3.9b), (3.12) and (3.14) with the result

$$f \cdot \Phi_{oc} = -\frac{1}{z_V}\int_0^L \frac{c_V(x)}{c_V(x)+\Theta c_e(x)}\left(\nabla\ln c_V(x) - \frac{z_V}{z_e}\nabla\ln c_e(x)\right)\cdot \mathrm{d}x$$

$$= -\frac{1}{z_V}\left\{\frac{1-z_V^2\Theta}{1-z_e z_V \Theta}\ln\frac{c_{V_L}+\Theta c_{e_L}}{c_{V_0}+\Theta c_{e_0}} - \frac{z_V}{z_e}\ln\frac{c_{e_L}}{c_{e_0}}\right\} \qquad (3.19)$$

While both expressions for Φ_{oc} are useful, the latter result should, in principle, be more accurate since less assumptions were made in it development. Nevertheless, a knowledge of K_r, D_e, and D_V are critical for the successful application of either equation and is discussed in the following section.

3.4 EVALUATING THE MAGNITUDE OF THE EQUILIBRIUM CONSTANT, K_r

In this section, the evaluation of the external equilibrium constant K_r and it relationship with the diffusivity of ionic and electronic defect species is discussed because of their importance in predicting the performance of SOFCs. Ultimately, K_r must be obtained from experiments. However, typical conductivity and *open-circuit potential* experiments measure properties that depend on K_r as well as the electron diffusivity, D_e. Consequently, it is difficult to separate K_r and D_e from such measurements without independent knowledge of one of them.

Usually, researchers try to circumvent this problem by using other experimental methods such as Hebb-Wagner polarization or thermogravimetry. However, these experiments introduce other problems. Hebb-Wagner polarization experiments, which use blocking electrodes, depend on the reversibility of electrodes used for the experiment [40, 41]. The assumption of electrode reversibility, however, is often unjustifiable (especially at low temperatures) and becomes poorer as current increases (from zero). Conversely, thermogravimetry is, in principle, an excellent way of determining defect concentration dependence on oxygen partial pressure (from which K_r may then be deduced through appropriate methods). However, the small mass variations involved in non-stoichiometry experiments (with oxide MIECs) push the sensitivity of the equipment used to (and often beyond) their limits, making this technique at best very difficult and error prone [40].

In an attempt to address these issues, three methods (including thermogravimetry) of evaluating K_r are examined and compared in this section. Two other methods were discussed in an earlier report. As will become increasingly clear (if not already so), K_r is a critical constant and it is worth the effort to find reliable ways of determining its value accurately.

3.4.1 Estimation of K_r from Thermogravimetry

In principle, the best way to determine K_r is through thermogravimetric experiments, which are designed to give the weight change of an MIEC sample (and hence the concentration of defects) as a function of P_{O_2} [42]. However, it is usually very difficult to get accurate and reproducible data from thermogravimetric experiments because of the high sensitivity required to detect very small changes in the mass of the specimen [38]. Nevertheless, Kobayashi *et al.* [43] recently determined the oxygen/metal atom ratios (c_O/c_{cat}) for SDC for various temperatures and

Table 3-1. Calculated values of K_r for SDC from thermogravimetry data of Kobayashi *et al*. [43].

c_O/c_{cat}	log P_{O_2} [ln (atm.)]	K_r ($m^{-9}atm.^{1/2}$)	ln K_r ($m^{-9}atm.^{1/2}$)
1.86	-20.5	6.732×10^{71}	165.390
1.87	-19.5	1.149×10^{72}	165.925
1.88	-18.75	1.159×10^{72}	165.934
1.89	-17.55	1.102×10^{72}	165.883

pressures. Oxygen vacancy concentration is related to the c_O/c_{cat} ratio as follows:

$$c_V = c_{cat}\left(2 - c_O / c_{cat}\right) \tag{3.20}$$

and substituting Eq. (3.20) into Eq. (3.15) and rearranging it yields for K_r:

$$K_r^{\frac{1}{2}} = \tfrac{4}{3} P^{\frac{1}{4}} c_V^{\frac{3}{2}} - \tfrac{4}{3} P^{\frac{1}{4}} \left(\tfrac{1}{2} c_A\right)^{\frac{3}{2}} = \tfrac{4}{3} P^{\frac{1}{4}} \left[c_{cat}\left(2 - c_O / c_{cat}\right)\right]^{\frac{3}{2}} - \tfrac{4}{3} P^{\frac{1}{4}} \left(\tfrac{1}{2} c_A\right)^{\frac{3}{2}} \tag{3.21}$$

K_r is calculated from Eq. (3.21) for c_O/c_{cat} ratios in the range 0.186 to 0.189 at 800 °C where c_{cat} = 2.5×10^{28} m^{-3}—SDC lattice constant = 0.544 nm [44]—and $c_A = 0.2c_{cat}$ using Eq. (3.21); the results are shown in Table 3-1. The values calculated for K_r are narrowly distributed and so the standard deviation of the data set for ln K_r is 0.263[4] [ln ($m^{-9}atm.^{1/2}$)], which is < 0.2% in the worst case. The average value[4] of K_r in Table 3-1 is 9.97×10^{71} $m^{-9}atm.^{1/2}$.

3.4.2 Estimation of K_r from Open-Circuit Potential

In this section, expressions derived earlier, Eqs. (3.17) and (3.19), for Φ_{OC} are used to determine K_r from experimental data. Rearranging Eq. (3.17) yields

$$K_r^{\frac{1}{2}} = \frac{\left(\frac{1}{2} c_A\right)^{\frac{3}{2}}}{\frac{3}{4} + \Theta} \cdot \frac{1 - \left(\frac{P_L}{P_0}\right)^{-\frac{1}{4}\left(1 - \frac{\Phi_{OC}}{\Phi_{th}}\right)}}{P_0^{-\frac{1}{4}} \left(\frac{P_L}{P_0}\right)^{-\frac{1}{4}\left(1 - \frac{\Phi_{OC}}{\Phi_{th}}\right)} - P_L^{-\frac{1}{4}}} \tag{3.17b}$$

which allows direct calculation of K_r. Conversely, K_r must be calculated from Eq. (3.19) through numerical (e.g., an equation solver) means.

[4] The geometric mean and variance were required to calculate the standard deviation in the K_r values.

In principle, either Eqs. (3.17) or (3.19) allows K_r to be determined from measurements of Θ and Φ_{oc} for a given P_0 and P_L. However, Eq. (3.19) has the advantage of being derived using $c_i(x)$, which is an exact solution, Eq. (3.12), of the transport laws (in *open-circuit* conditions) given in section 4.3. Conversely, Eq. (3.17) is derived using $c_i(P)$, Eqs. (3.15) and (3.16), which were modeled using (reasonable) simplifying assumptions. In addition, Eq. (3.19) can be used to determine other external equilibrium constants (i.e., it is not specific to *n*-type fluorites like SDC or GDC) as a function of Θ (or D_e) for given environmental conditions (e.g., P_L, P_0, T, etc.).

In calculating K_r, experimental values of Φ_{oc} may need to be corrected for electrode effects, which alter the true oxygen activity seen by the electrolyte at each interface. Furthermore, as Steele [19] points out, values for D_e, and hence Θ, are difficult to obtain from experiment. Moreover, values available in the literature are inconsistent.

Gödickemeier *et al.* [45, 46] modeled and evaluated the overpotentials for various electrodes on a SDC electrolyte. From their data for a $La_{0.84}Sr_{0.16}CoO_3$ cathode and a Ni-$Ce_{0.9}Ca_{0.1}O_{1.9}$ cermet anode on an SDC electrolyte, values of $\Phi_{oc} \approx 800$ mV ($\Phi_{oc} \approx 740$ mV when corrected for electrode overpotentials [45, 46]) and $\Phi_{th} \approx 941$ mV for $P_L = 0.21$ atm. and $P_0 \approx 4 \times 10^{-19}$ atm. at 800 °C were obtained. K_r is calculated for various values of Θ, from Eqs. (3.17) and (3.19), using *corrected* (for electrode overpotential) data from Gödickemeier *et al.* [45, 46] and the results are shown in Table 3-2.

Table 3-2 shows that, for a given $\Theta \geq 1$, the K_r values calculated using Eq. (3.17) or Eq. (3.19) are very close. However, for $\Theta \leq 1$ no unique value of K_r is computable from Eq. (3.19). Physically, that is a good result since it implies that, for $\Theta \leq 1$ (i.e., $D_e \leq 4D_V$), the main reason $\Phi_{oc} < \Phi_{th}$ (i.e., $\Phi_{oc}/\Phi_{th} < 1$) is the presence of the ionic defect concentration gradient. Finally, K_r values calculated from Eq. (3.19) are always greater than those from Eq. (3.17). This trend likely indicates that there is an underestimation of the oxygen vacancy concentration gradient in Eq. (3.17), since the difference between the values gets smaller as Θ increases (i.e., as the effect of D_e on Φ_{oc} becomes more significant than the oxygen vacancy concentration gradient).

Two additional features of Eqs. (3.17) and (3.19) are of particular interest. First, by rewriting Eq. (3.17) as follows:

$$\frac{K_r(3+4\Theta)^2}{16c_A^3} \approx \frac{K_r\Theta^2}{c_A^3} = \beta = \tfrac{1}{8}\left[1-\left(\frac{P_L}{P_0}\right)^{-\frac{1}{4}\left(1-\frac{\Phi_{oc}}{\Phi_{th}}\right)}\right]^2\left[P_0^{-\frac{1}{4}}\left(\frac{P_L}{P_0}\right)^{-\frac{1}{4}\left(1-\frac{\Phi_{oc}}{\Phi_{th}}\right)} - P_L^{-\frac{1}{4}}\right]^{-2} \qquad (3.22)$$

it becomes evident that for given values of t'_{ion}, c_A, P_L and P_0, the term β is a constant.

Table 3-2. Calculated values of Θ and K_r for SDC SOFC from the *corrected* Φ_{oc} data of Gödickemeier *et al.* [45, 46].

	from Eq. (3.19)		from Eq. (3.17)	
$\Theta = D_e/4D_V$	K_r ($m^{-9}atm.^{1/2}$)	β ($atm.^{1/2}$)	K_r ($m^{-9}atm.^{1/2}$)	β ($atm.^{1/2}$)
0.1	n.a.	n.a.	8.7×10^{74}	7.0×10^{-11}
1	6.6×10^{75}	5.3×10^{-8}	2.1×10^{74}	1.7×10^{-9}
10	8.1×10^{72}	6.5×10^{-9}	5.5×10^{72}	4.4×10^{-9}
24.4	1.2×10^{72}	5.7×10^{-9}	1×10^{72}†	4.7×10^{-9}
26.4	1×10^{72}†	5.6×10^{-9}	8.5×10^{71}	4.7×10^{-9}
100	6.5×10^{70}	5.2×10^{-9}	6.2×10^{70}	5.0×10^{-9}
1000	6.4×10^{68}	5.1×10^{-9}	6.3×10^{68}	5.0×10^{-9}

†K_r calculated from thermogravimetric data of Kobayashi *et al.* [43], section 4.4.2.

Similarly, for $\Theta c_{e_0} >> c_{V_0}$, $c_{e_L} << c_{V_L} = c_A/2$ (typical for SDC or GDC if $P_L \geq$ ~0.21 atm. and $P_0 \leq$ $\sim 10^{-18}$ atm. [19, 36, 45 - 47]) and $\Theta >> 1/2$ (i.e., $D_e >> 2D_V$), Eq. (3.19) becomes:

$$f \cdot \Phi_{oc} \approx \mathbf{ln} \frac{c_{V_L}}{\Theta c_{e_L}} \tag{3.23a}$$

Moreover, Eqs. (3.13), (3.15) and (3.16) may be substituted into Eq. (3.23a), with the result

$$\beta = K_r \Theta^2 c_A^{-3} \approx \tfrac{1}{8} P_L^{\frac{1}{2}} \mathbf{exp}\left(f \cdot \Phi_{oc} \right) \equiv \text{constant} \tag{3.23b}$$

Therefore, from an entirely different approach, Eq. (3.23b) shows that, for a given Φ_{oc}, β is a (material) constant. Thus, one may deduce from Eqs. (3.22) and (3.23b) that, for constant c_A, K_r is inversely proportional to Θ^2. This assertion is borne out in the trends evident in Table 3-2.

A second noteworthy feature of Eqs. (3.22) and (3.23b) is that as $\Phi_{oc}/\Phi_{th} \rightarrow 1$ (i.e., for good electrolytes) $\beta \rightarrow 0$ (i.e., a very small value). Conversely, as $\Phi_{oc}/\Phi_{th} \rightarrow 0$ (i.e., for poor electrolytes) Eq. (3.22)[5] shows that $\beta \rightarrow \infty$. In other words, the suitability of an oxide MIEC as an electrolyte can be determined from knowledge of β which combines information on the reducibility of the MIEC (K_r), the relative diffusivity of the electronic and ionic defects, Θ, and the doping level (c_A).

[5] The assumptions made in deriving Eq. (3.19c) from Eq. (3.19) exclude poor electrolytes. Nevertheless, Eq. (3.19c), still shows that β attains its maximum value when $\Phi_{oc} = 0$.

Additionally, since β is a material constant, it is difficult to separate K_r and Θ (D_e) in experiments which measure properties that are dependent on both defect concentration (K_r and c_A) and diffusivity (Θ or D_e) such as conductivity (next section) and *open-circuit potential* (discussed in this section) experiments.

Finally, ln K_r (ln $K_r = -\Delta G_r/k_BT$, where ΔG_r is the Gibbs' free energy associated with the reaction in Eq. (3.21))[6] doesn't change much even when Θ varies over ~2 orders of magnitude. From the preceding discussion, this result may indicate that the oxygen exchange process is limited by the ability of the SDC to produce electrons (i.e., its band gap) rather than the relative speed (i.e., Θ) they are supplied to, or consumed from, the interface.

3.4.3 Estimation of K_r from Conductivity Measurements

K_r may also be determined from conductivity measurements. This method is very attractive because electrode effects (typically measured in electrode overpotentials) are essentially absent and thus (in comparison to the preceding strategy) "corrections" (a la Gödickemeier *et al.* [45, 46]) are unnecessary. Eqs. (3.1), (3.2), (3.15), (3.16) and (2.8) may be combined to yield, for the total conductivity of SDC:

$$\sigma_{tot} = z_V^2 fqD_V\left(c_V + \Theta c_e\right) = qfz_V^2 D_V\left\{\left[\tfrac{3}{4}K_r^{\frac{1}{2}}P^{-\frac{1}{4}} + \left(\tfrac{1}{2}c_A\right)^{\frac{3}{2}}\right]^{\frac{2}{3}} + \frac{\Theta K_r^{\frac{1}{2}}P^{-\frac{1}{4}}}{\left[\tfrac{3}{4}K_r^{\frac{1}{2}}P^{-\frac{1}{4}} + \left(\tfrac{1}{2}c_A\right)^{\frac{3}{2}}\right]^{\frac{1}{3}}}\right\} \qquad (3.24a)$$

Moreover, if $\tfrac{3}{4}K_r^{\frac{1}{2}}P^{-\frac{1}{4}} << \left(\tfrac{1}{2}c_A\right)^{\frac{3}{2}}$ then

$$\sigma_{tot} = \tfrac{1}{2}qfz_V^2 D_V c_A\left\{1 + \frac{\Theta K_r^{\frac{1}{2}}P^{-\frac{1}{4}}}{\left(\tfrac{1}{2}c_A\right)^{\frac{3}{2}}}\right\} = \tfrac{1}{2}qfz_V^2 D_V c_A\left\{1 + \beta^{\frac{1}{2}}P^{-\frac{1}{4}}\right\} \qquad (3.24b)$$

By fitting Eq. (3.24a) to conductivity data [47], a unique value of Θ (or D_e) can be found for any K_r or vice versa. In addition, since a data set is fitted rather than one data point (the case for Φ_{oc} data and Eqs. (3.17) and (3.19)) statistical errors are minimized. The results of this strategy are provided in Table 3-3. In comparison to Table 3-2, Table 3-3 shows higher K_r values for each Θ (or higher Θ for a given Kr) and, accordingly, higher β values. Because of the

[6] In the strictest sense K_r should be dimensionless when used for the calculation of ΔG_r. Nonetheless, the analysis presented remains valid since the additional terms required to make K_r dimensionless constitute a constant.

Table 3-3. Values of Θ, K_r and β calculated from fitting Eq. (3.24) to the SDC conductivity data of Eguchi *et al.* [47].

$\Theta = D_e/4D_V$	K_r ($m^{-9}atm.^{1/2}$)	ln K_r ($m^{-9}atm.^{1/2}$)	β ($atm.^{1/2}$)
0.1	1.0×10^{77}	177.3	8.0×10^{-9}
1	1.3×10^{76}	175.3	1.0×10^{-7}
10	2.0×10^{74}	171.1	1.6×10^{-7}
100	2.0×10^{72}	166.5	1.6×10^{-7}
140	1.0×10^{72}†	165.8	1.6×10^{-7}
1000	2.0×10^{70}	161.9	1.6×10^{-7}

†K_r calculated from thermogravimetric data of Kobayashi *et al.* [43] in section 4.4.2.

absence of electrode effects and since conductivity measurements are made at equilibrium, the values of Θ and K_r obtained from conductivity measurements (Table 3-3) may be considered to be "more correct" than those from Φ_{oc} measurements (Table 3-2). Additionally, the lower β values in Table 3-2 may be due to the calculations being made for a single (P_L, P_0, T) coordinate rather than a range as is the case for the conductivity data, in Table 3-3. As will be demonstrated in later sections this can have a significant effect on the calculations.

In closing this section, it is worth noting that the ΔG_r values (i.e., $RT\ln K_r$) calculated (for a given Θ) from any of the electrical/electrochemical methods—Eqs. (3.17), (3.19) or (3.24)—are, given acceptable experimental error, almost the same. This speaks to the utility and correctness of the strategies employed to calculate ΔG_r (or K_r).

4. OPEN CIRCUIT POTENTIAL AND MODEL VERIFICATION FOR SDC SOFCS

In this section, the electrochemical performance of SOFCs assembled in our laboratory consisting of SDC electrolytes and porous platinum (Pt) or gold (Au) electrodes with air on the cathode side of the electrolyte and either CO/CO_2 or H_2/H_2O gas mixture at the anode are reported (sections 4.1 and 4.2). The model developed in section 3—Eq. (3.19)—is then evaluated by fitting it to the experimental data presented in section 4.1.

4.1 OPEN CIRCUIT POTENTIAL

Porous Pt electrodes were applied to samples with density ≥ 90 % of the theoretical density. These samples were used to construct an SOFC of the type;

$$P_{O_2}, \text{ Pt/SDC/Pt, } P_{CO/CO_2} \left(\text{or } P_{H_2/H_2O}\right) \tag{4.1}$$

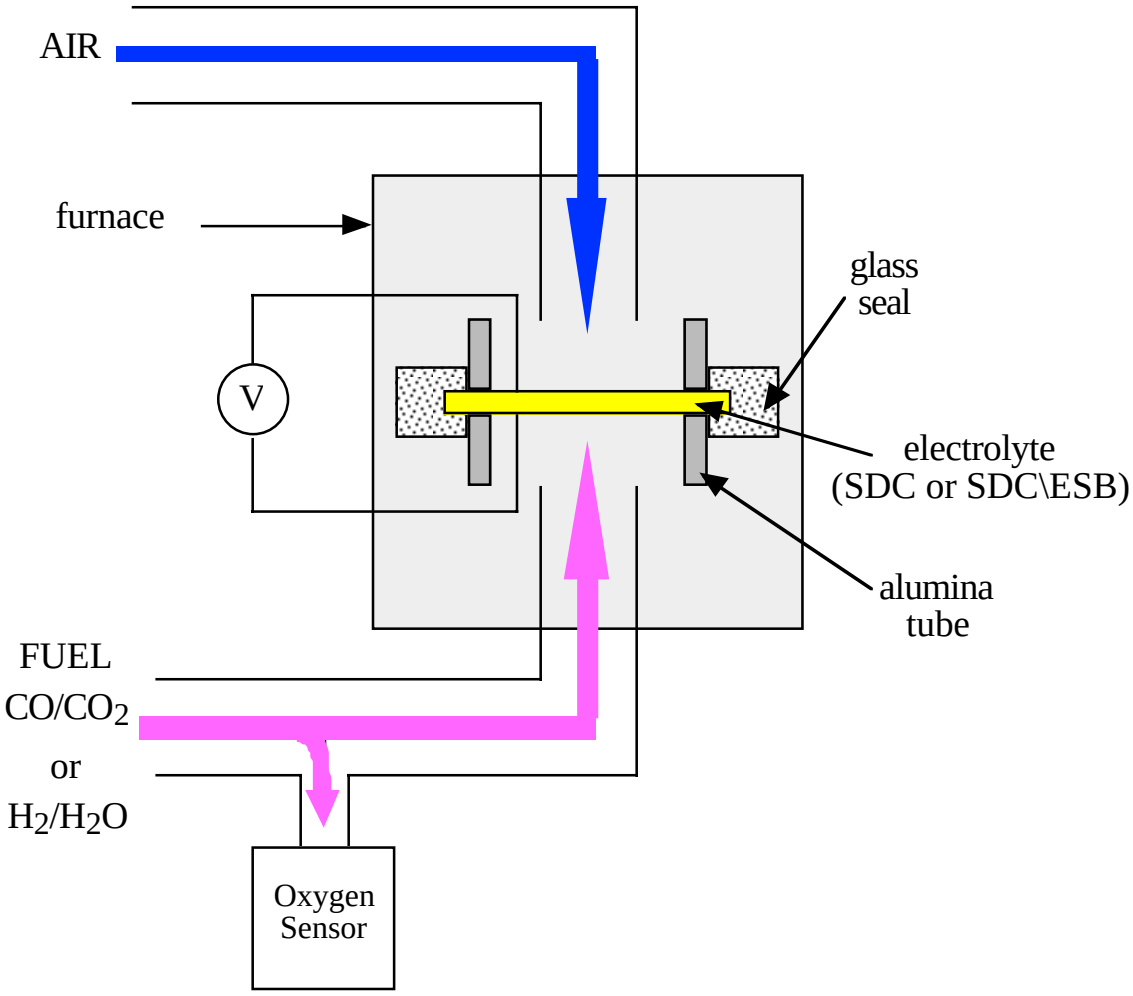

Figure 4-1. Setup of the fuel cell apparatus.

with air as the oxidizing gas and CO/CO_2 or H_2/H_2O gas mixtures as the reducing gas. Φ_{oc} was then measured with a Keithley 2000 multimeter, as shown in Figure 4-1, for various P_{O_2}'s and temperatures and used to calculate the apparent transference number, t'_{ion}, which is given by

$$t'_{ion} = \frac{\Phi_{oc}}{\Phi_{th}} \tag{4.2}$$

where Φ_{th} is the theoretical (Nernst) potential.

Each P_{O_2} was set by the mixing ratio of the reducing gases (the P_{O_2} on the oxidizing side was kept constant). The P_{O_2} of each reducing gas mixture was measured with a zirconia (automotive) oxygen sensor, placed in series with the SOFC, with (stagnant) air on the reference

side and the reducing gas combination to be measured on the sensing side. The sensor potential is taken as equal to the theoretical (Nernst) potential, Φ_{th}, for the fuel cell since $t'_{ion} = 1$ for zirconia. Therefore:

$$\Phi_{sensor} = \Phi_{th} = \frac{k_B T}{4q} \ln \frac{P_L}{P_0} \tag{4.3}$$

where P_L is the P_{O_2} on the oxidizing/air side (at x = L) and P_0 is the P_{O_2} on the reducing/fuel side (at x = 0). P_0 may then be calculated from a knowledge of the sensor potential, P_L and temperature. Additional details of the experimental procedure may be obtained elsewhere [48].

Figures 4-2 and 4-3 show the dependence of Φ_{oc} and t'_{ion} on P_{O_2} in the temperature range 500 °C to 800 °C. In Figure 4-3, the experimental error (calculated statistically) in t'_{ion}, arising primarily from small, random fluctuations, are represented as error bars. In Figure 4-2, Φ_{oc} (see Eq. (4.1)) is near theoretical (sensor) for *high* P_{O_2} and therefore falls on a 45° line. At *low* P_{O_2}, Φ_{oc} begins to deviate due to the onset of electronic conduction. Correspondingly, in Figure 4-3, t'_{ion} was constant and close to unity in the *high* P_{O_2} region and decreased in the *low* P_{O_2} region. The P_{O_2} for the onset of electronic conduction (i.e., $t'_{ion} \leq 0.9$ for $P_{O_2} \leq P_{O_2}^{onset}$) is shown in Table 4-1. As expected, the Φ_{oc} and t'_{ion} of the SOFCs decreased with increasing temperature as a result of the diminishing ionic domain of the SDC electrolyte. In Figure 4.2a, Φ_{oc} is normalized by the factor nF/RT in order to make the curves more visually distinguishable.

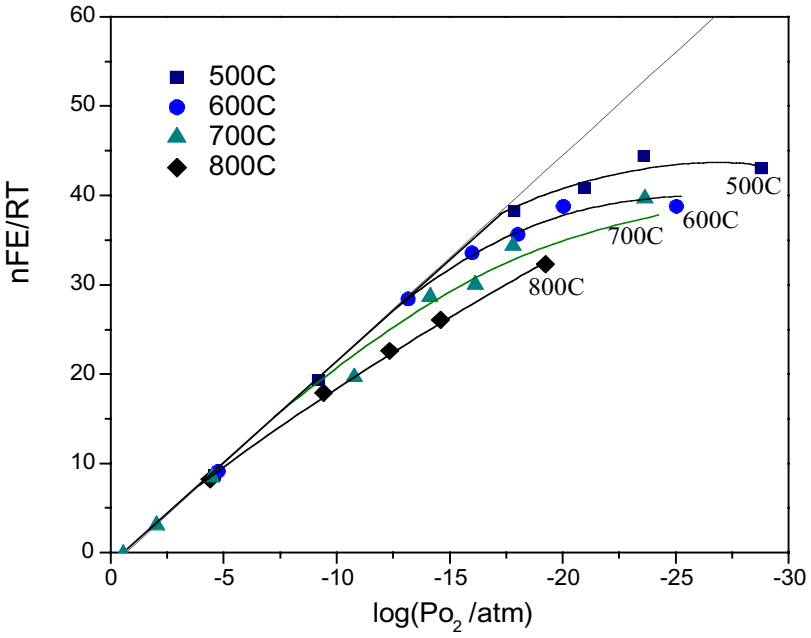

(a)

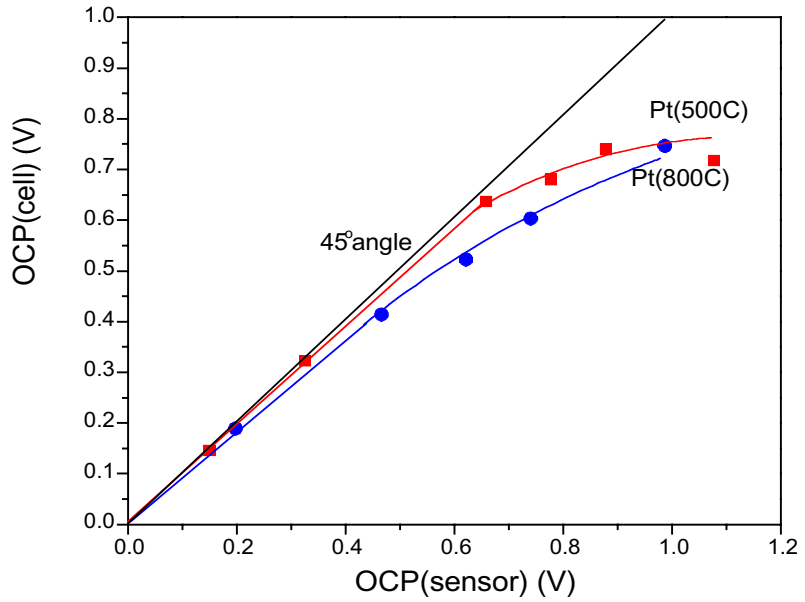

(b)

Figure 4-2. Normalized OCP (*nFE/RT*) of the SOFC, P_{O_2}, Pt/SDC/Pt, P_{CO/CO_2} $\left(\text{or } P_{H_2/H_2O}\right)$, as a function of (a) P_{O_2} and (b) sensor potential (Φ_{th}).

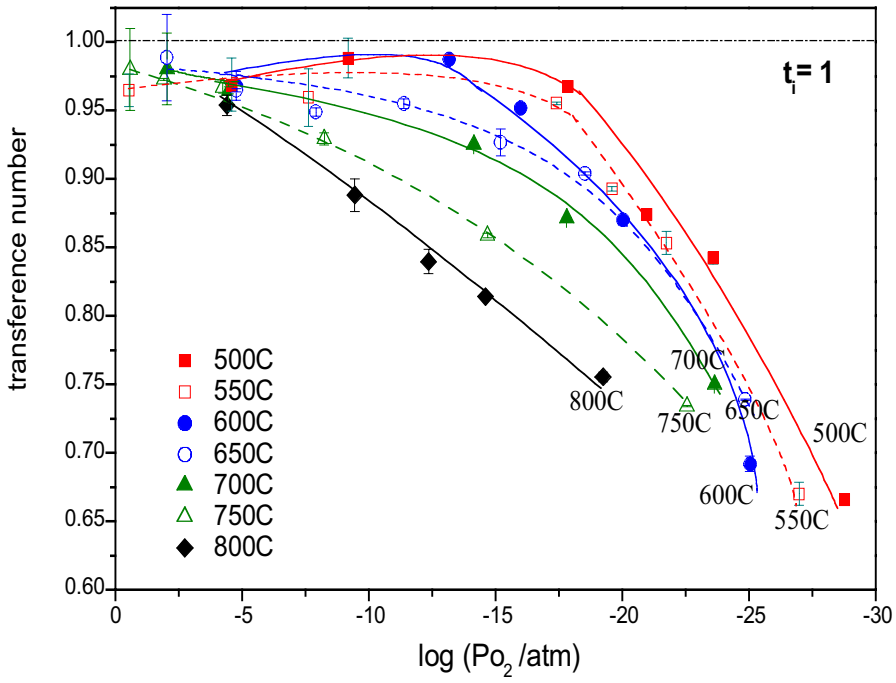

Figure 4-3. Dependence of t'_{ion} on P_{O_2} for 500 °C ≤ T ≤ 800 °C for the SOFC, P_{O_2}, Pt/SDC/Pt, P_{CO/CO_2} $\left(\text{or } P_{H_2/H_2O}\right)$.

4.2 EFFECT OF CATHODE MATERIAL (Au AND Pt)

The electrochemical performance of SOFCs is influenced greatly by the characteristics of the electrodes. In this work, both Pt and Au electrodes were used in the ceria-based SOFCs. Au is a notoriously bad electrode material. However, it is a stable (i.e., it does not react with ESB) material for use as a cathode on the SDC\ESB bilayers. To evaluate the performance of the Au electrode on SDC electrolytes (and later for comparison with bilayered SDC\ESB electrolytes) an SOFC was constructed of the following type

$$P_{O_2},\ \text{Au/SDC/Pt},\ P_{CO/CO_2}\left(\text{or } P_{H_2/H_2O}\right) \qquad (4.4)$$

and its Φ_{oc} values compared with those obtained from the SOFC in Eq. (4.1).

Figure 4-4 shows the P_{O_2} dependence of Φ_{oc} in the temperature range: 650 °C ≤ T ≤ 800 °C and Figures 4-5 and 4-6 show the P_{O_2} dependence of t'_{ion} in the temperature range: 500 °C ≤ T ≤ 800 °C for the SDC SOFC with the Au cathode. Table 4-1 compares the values of P_{O_2} at which t'_{ion} drops below 0.9 for SDC SOFCs with Pt and Au cathodes. Godickemeier *et al.*[45,

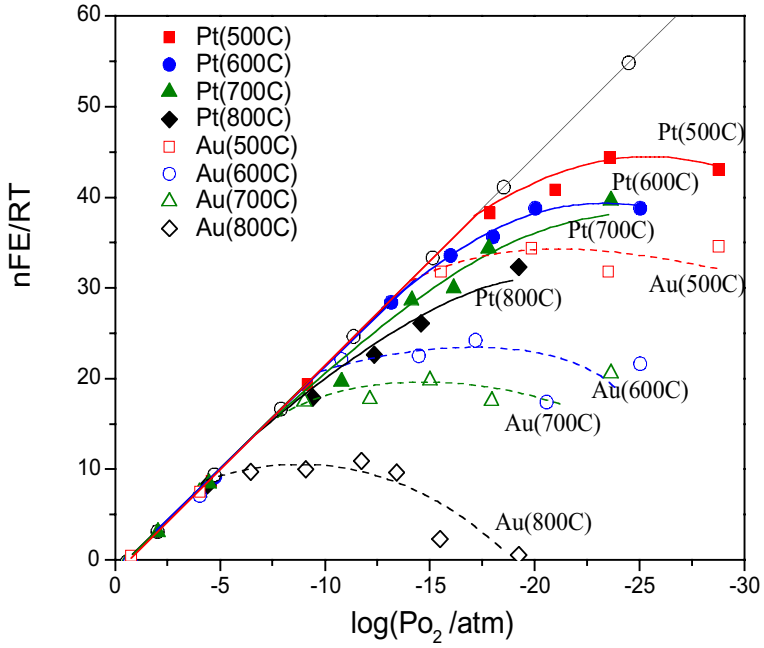

(a)

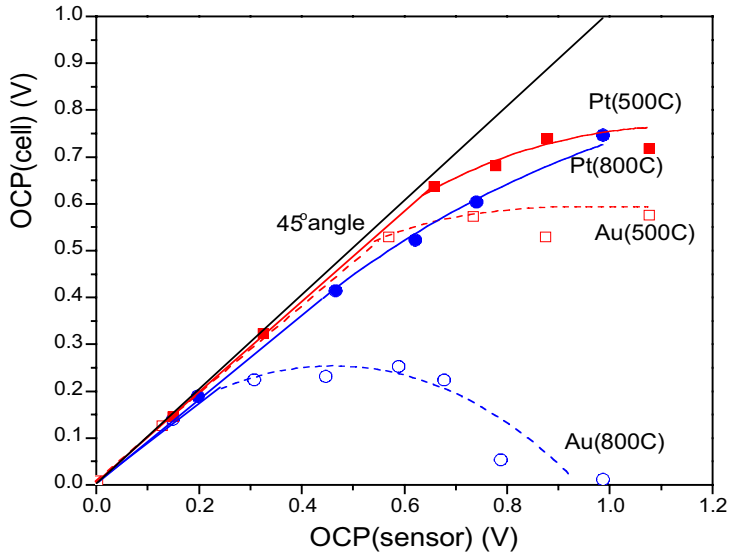

(b)

Figure 4-4. Comparison of normalized OCP (*nFE/RT*) of SOFCs in Eqs. (4.1) and (4.4) as a function of (a) P_{O_2} and (b) sensor potential (Φ_{th}).

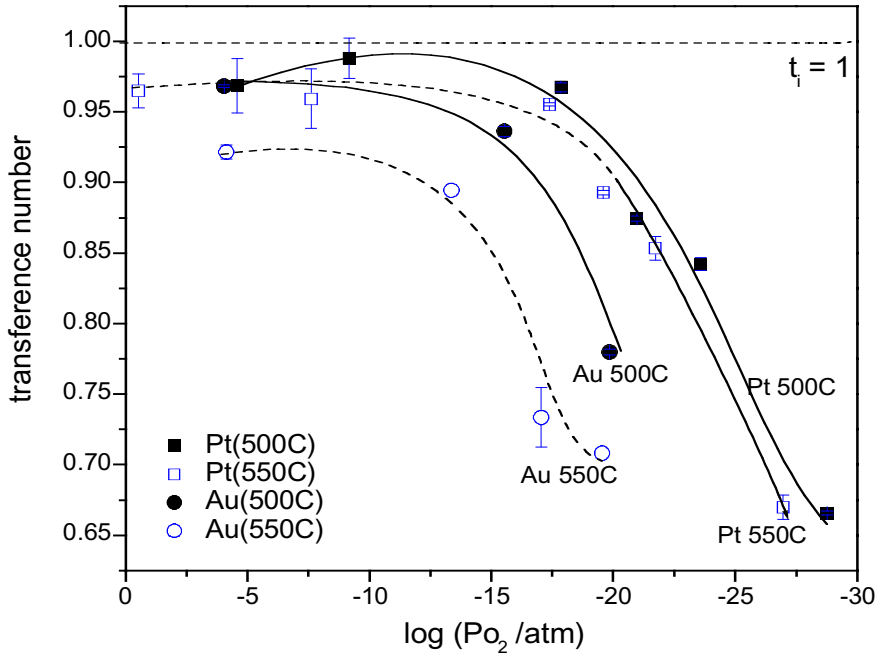

(a)

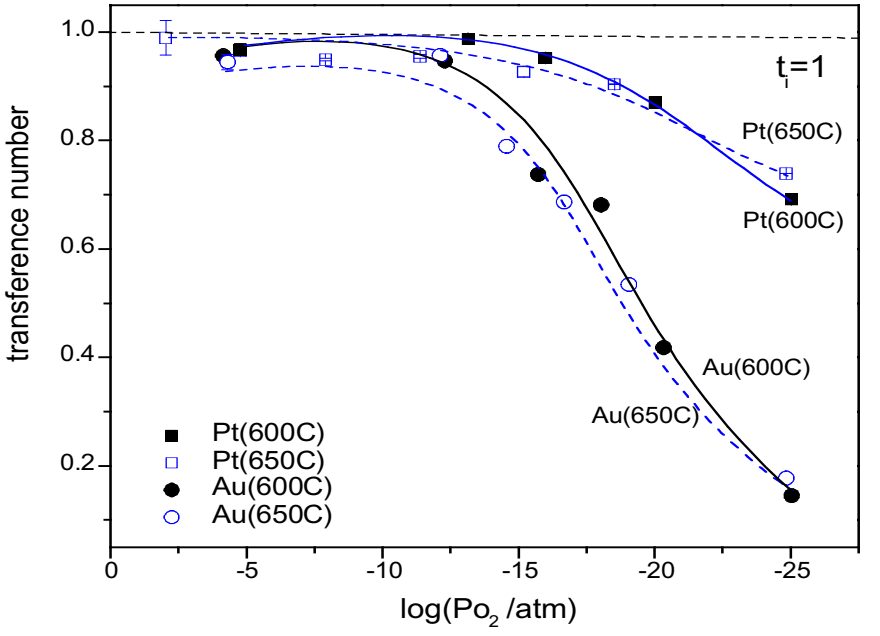

(b)

Figure 4-5. Comparison of t'_{ion} for SOFCs in Eqs. (4.1) and (4.4) as a function of P_{O_2} at (a) 500 and 550°C and (b) 600 and 650°C.

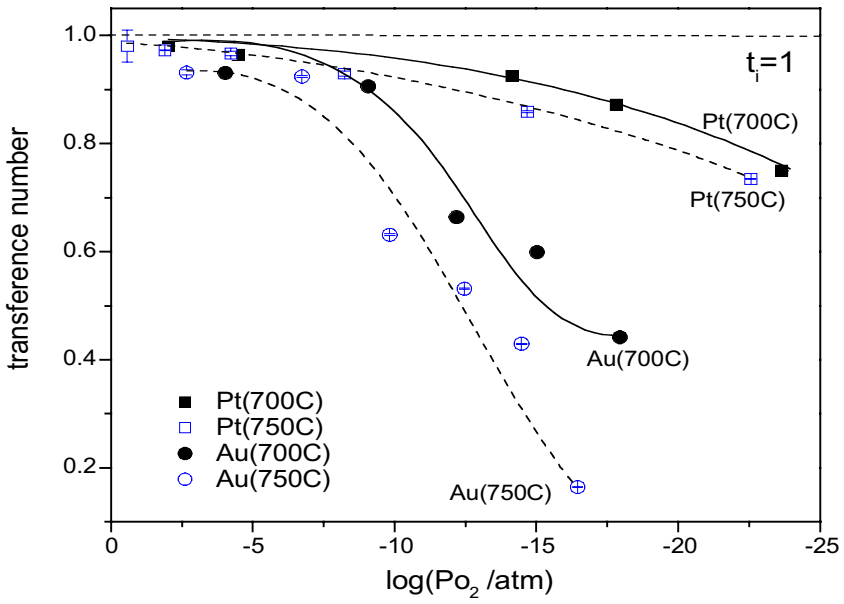

(a)

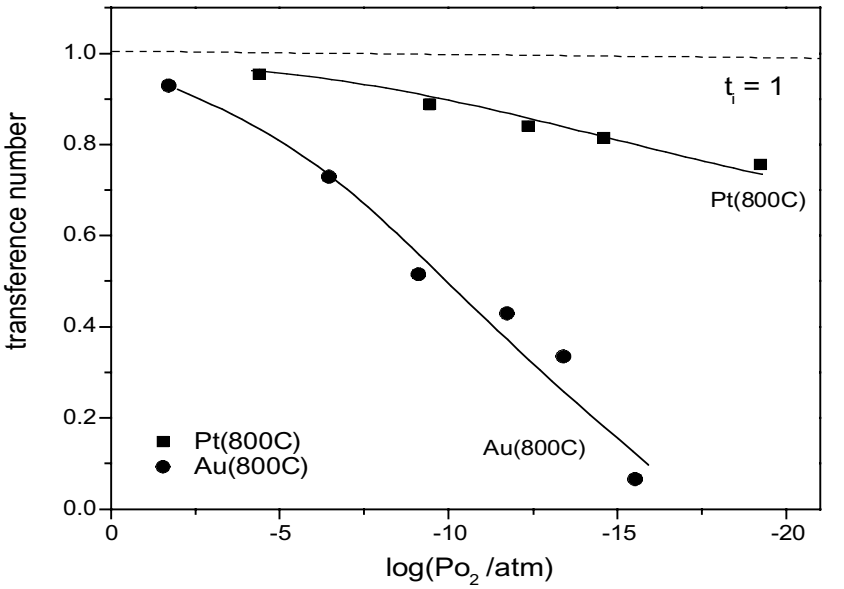

(b)

Figure 4-6. Comparison of t'_{ion} for SOFCs in Eqs. (4.1) and (4.4) as a function of P_{O_2} at (a) 700 and 750ϒC and (b) 800ϒC.

Table 4-1. Oxygen Partial Pressure at which t'_{ion} = 0.90 for SOFCs in Eqs. (4.1) and (4.4).

Temperatures (ϒC)	P_{O_2}, Pt cathode (atm.)	P_{O_2}, Au cathode (atm.)
500	~ 10^{-22}	~ $10^{-17.5}$
550	~ 10^{-21}	~ 10^{-14}
600	~ $10^{-19.5}$	~ $10^{-13.5}$
650	~ 10^{-18}	~ 10^{-13}
700	~ 10^{-16}	~ $10^{-9.5}$
750	~ 10^{-12}	~ $10^{-7.5}$
800	~ 10^{-8}	~ 10^{-4}

46] showed that both Au and Pt electrodes allow for oxygen transport with Au cathodes exhibiting a higher electrode overpotential than Pt cathodes. This is a consequence of Au being a poor electro-catalyst. Since Pt is electro-catalytically more active than Au, the chemical potential difference $(\mu''_{O_2} - \mu'_{O_2})$ across the electrolyte of a concentration cell with Pt electrodes is greater than with Au electrodes; this is shown schematically in Figure 4-7. Accordingly, a higher Φ_{oc} (and t'_{ion}) was obtained for the SDC SOFC that had a Pt rather than a Au cathode.

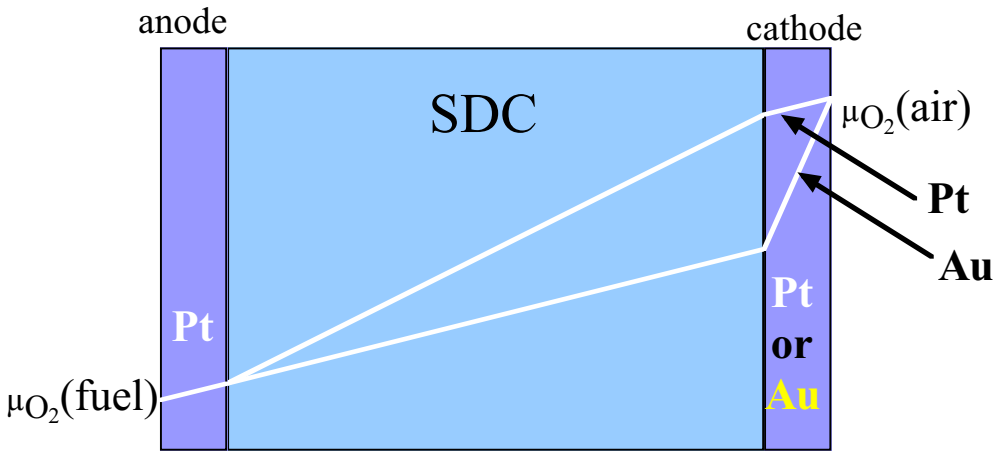

Figure 4-7. Schematic representation comparing the effect of electrode overpotential on the variation of μ_{O_2} across a SOFC with an Au vs. a Pt cathode.

4.3 EXPERIMENTAL VERIFICATION OF THE MODEL

In order to verify the accuracy and validity the model developed for *open-circuit* conditions in section 3.3, Eq. (3.19) is fitted to the experimental data in Figures 4-8 through 4-14. This was done by adjusting the parameters K_r and Θ (i.e., D_e/D_V) to maximize the correlation coefficient, r, (and $\breve{r}$, the corrected[7] correlation coefficient) [49] between the data and the model (i.e., to obtain the best fit of the model to the data). Table 4-2 shows the parameters used for each plot and the correlation coefficients obtained. The high correlation coefficients obtained and the fact that only two *degrees of freedom* are allowed are testament to the ability of the model to describe the physics relating the material properties of the electrolyte material (K_r and Θ) to the electrochemical performance of the SOFC.

Figures 4-8 through 4-14 show that as P_0 decreases below a critical value, Φ_{oc} becomes less than Φ_{th}. This corresponds to an increase in the electronic conductivity of the electrolyte, which is attributable to the increasing concentration of electrons on the reducing side of the electrolyte due to the decreasing P_{O_2}. In addition, the deviation of the Φ_{oc} from Φ_{th} starts progressively later as the temperature decreases which corresponds to a widening of the electrolytic domain of SDC, a phenomenon reported by other researchers. At 800 °C, Φ_{oc} starts to deviate from Φ_{th} at ~ 0.3 V while at 500 °C the deviation begins at ~ 0.7 V. This behaviour is a consequence of the exponential dependence of K_r on reciprocal temperature ($1/T$). Thus, K_r increases and SDC produces electrons more readily (i.e., at a higher P_{O_2}) as the operating temperature increases (see Eq. (3.19)).

Another noteworthy feature of Figures 4-8 to 4-14, is that as the temperature decreases, the shape of the curve for Φ_{oc} becomes more plateau-like once the deviation from Φ_{th} begins. This phenomenon may be explained by considering that at low temperatures $D_e/D_V >> 1$ and $c_{V_L} >>> c_{e_L}$, under these conditions Eq. (3.19) reduces to:

$$\Phi_{oc} = -\frac{k_B T}{z_e q} \ln \frac{c_{V_L} + \Theta c_{e_L}}{\Theta c_{e_L}} \tag{4.5}$$

In other words, at low temperatures Φ_{oc} is independent of P_0, a circumstance predicted by the model and borne out by experiment.

[7] In fitting Eq. (3.19) to experimental data, fitting parameters, K_r and Θ, are adjusted, i.e., the model has two *degrees of freedom*. The correlation coefficient, r, is often corrected to reflect the presence of the fitting parameters [49].

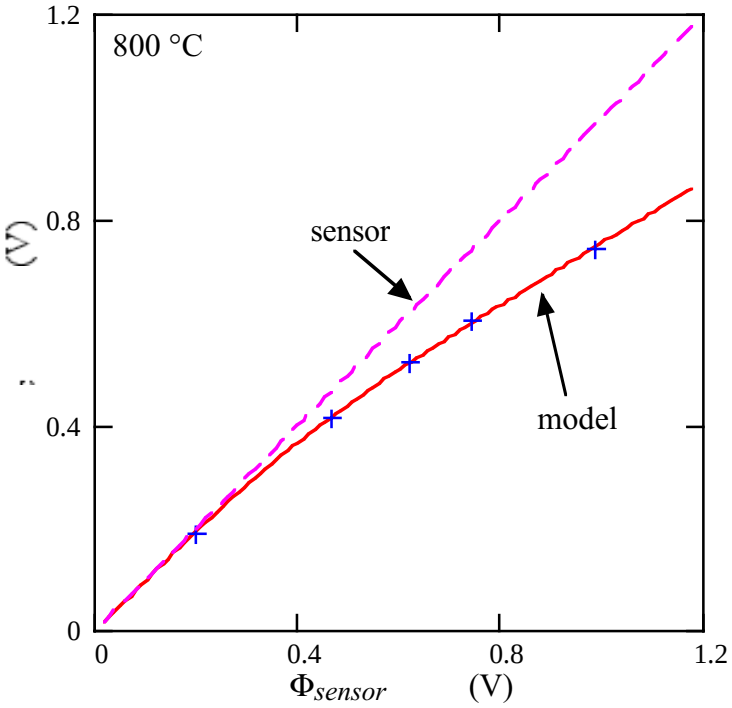

Figure 4-8. *Open-circuit* potential, Φ_{oc}, versus Φ_{sensor} (Φ_{th}) at 800 °C, model (—) fitted to experimental data (+) for the fuel cell; sensor (---).

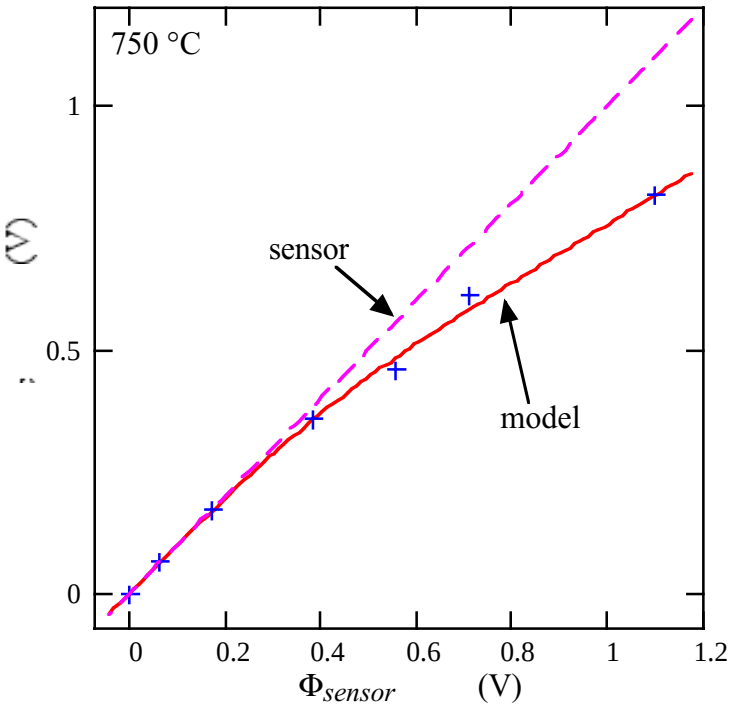

Figure 4-9. Open-circuit potential, Φ_{oc}, versus Φ_{sensor} (Φ_{th}) at 750 °C, model (—) fitted to experimental data (+) for the fuel cell; sensor (---).

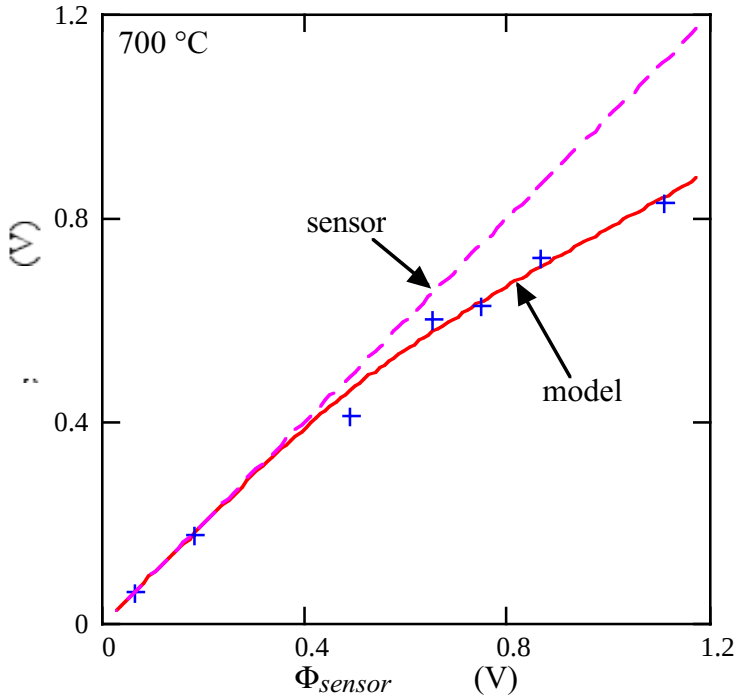

Figure 4-10. Open-circuit potential, Φ_{oc}, versus Φ_{sensor} (Φ_{th}) at 700 °C, model (—) fitted to experimental data (+) for the fuel cell; sensor (---).

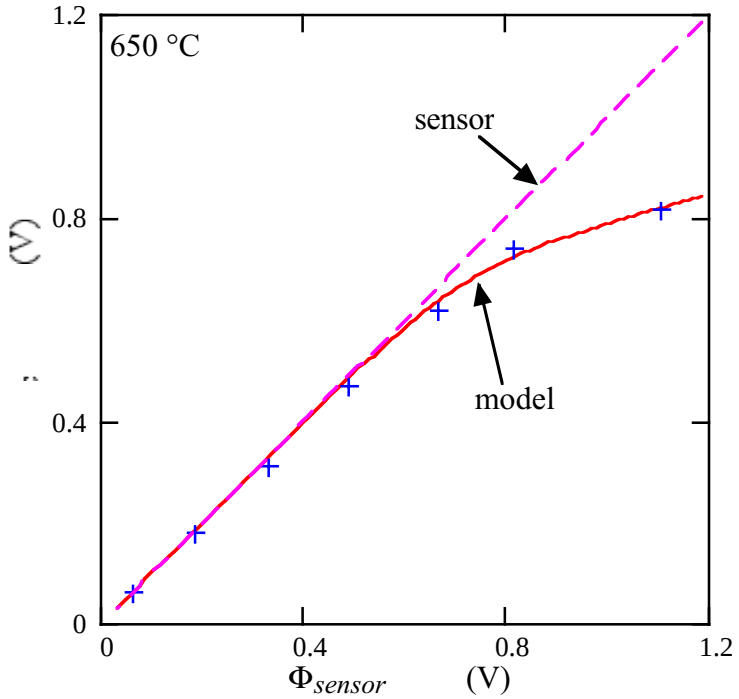

Figure 4-11. Open-circuit potential, Φ_{oc}, versus Φ_{sensor} (Φ_{th}) at 650 °C, model (—) fitted to experimental data (+) for the fuel cell; sensor (---).

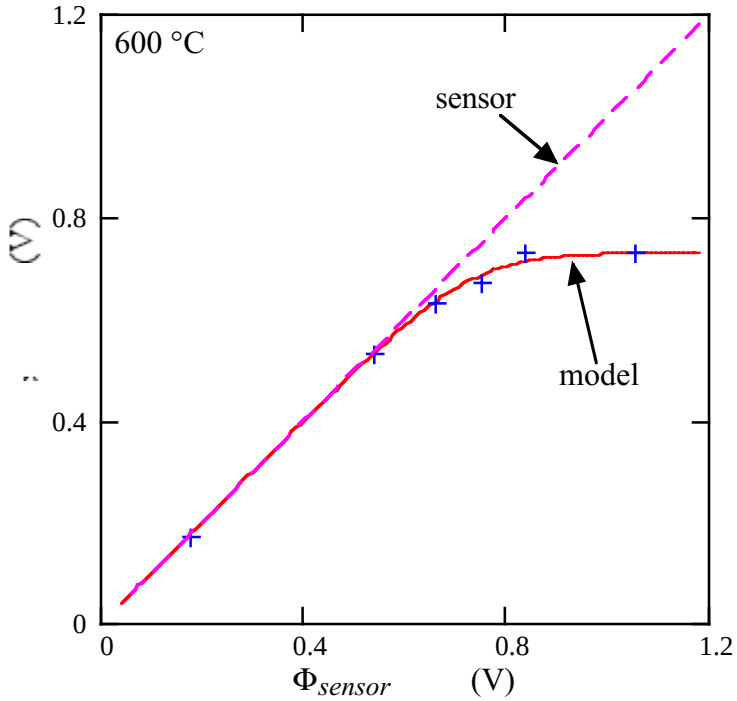

Figure 4-12. Open-circuit potential, Φ_{oc}, versus Φ_{sensor} (Φ_{th}) at 600 °C, model (—) fitted to experimental data (+) for the fuel cell; sensor (---).

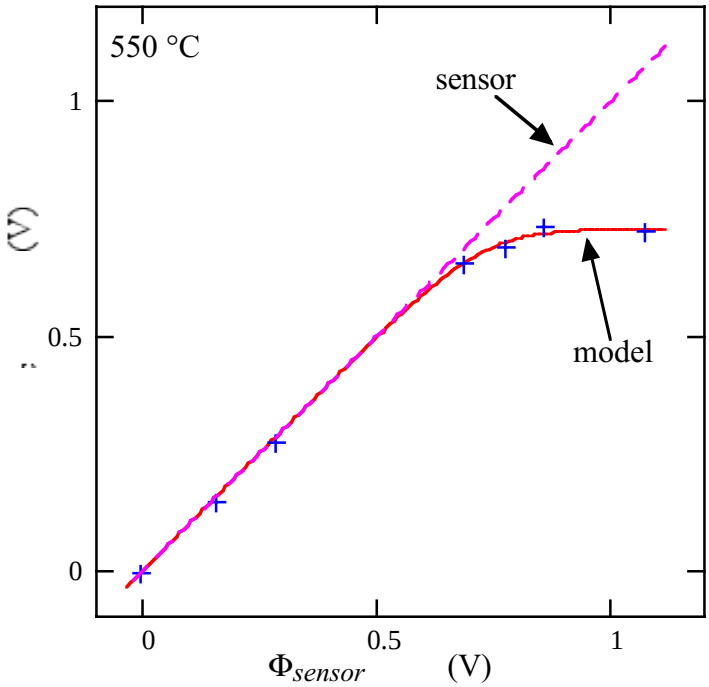

Figure 4-13. Open-circuit potential, Φ_{oc}, versus Φ_{sensor} (Φ_{th}) at 550 °C, model (—) fitted to experimental data (+) for the fuel cell; sensor (---).

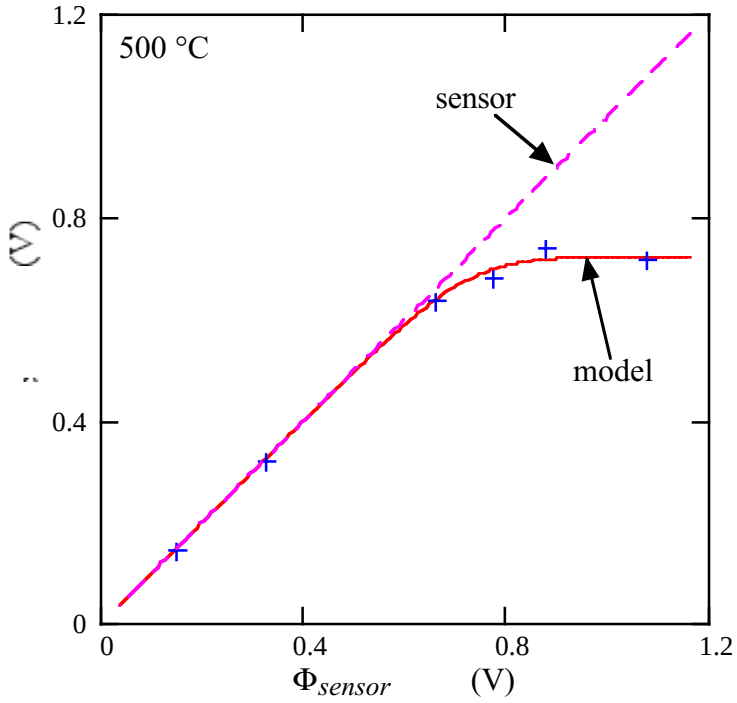

Figure 4-14. Open-circuit potential, Φ_{oc}, versus Φ_{sensor} (Φ_{th}) at 500 °C, model (—) fitted to experimental data (+) for the fuel cell; sensor (---).

As Figure 4-15 and Table 4-2. show, at 800 °C the values of K_r and D_e/D_V used to get the best fits to the data are respectively, larger and smaller than expected, i.e., K_r and D_e/D_V obtained at 800 °C do not concur with the values obtained in section 3.4. This outcome may be explained in two (complementary) ways. The first examines the impact of the (porous Pt) electrodes on the

Table 4-2. Values of K_r and D_e/D_V used to fit the model to experimental data

Temperature (°C)	K_r ($m^{-9}atm.^{1/2}$)	ln K_r	D_e/D_V	r	$\tilde{r}$
800	1.0×10^{72}†	165.8	1.1×10^{2}††	0.958	0.929
800	1.4×10^{79}	182.3	1.4	1.00	1.00
750	1.6×10^{78}	180.1	1.6	0.999	0.999
700	4.0×10^{77}	178.7	1.5	0.996	0.995
650	5.6×10^{73}	169.8	5.6	0.999	0.998
600	1.0×10^{71}	163.5	71	0.999	0.998
550	4.5×10^{66}	153.5	5.7×10^{3}	0.999	0.999
500	4.0×10^{65}	151.1	1.0×10^{4}	0.999	0.998

† K_r calculated from thermogravimetric data of Kobayashi *et al.* [43] in section 3.4.1, Table 3-1.

†† D_e/D_V calculated from Eq. (3.19) using data of Gödickemeier *et al.* [45, 46] in section 3.4.2, Table 3-2.

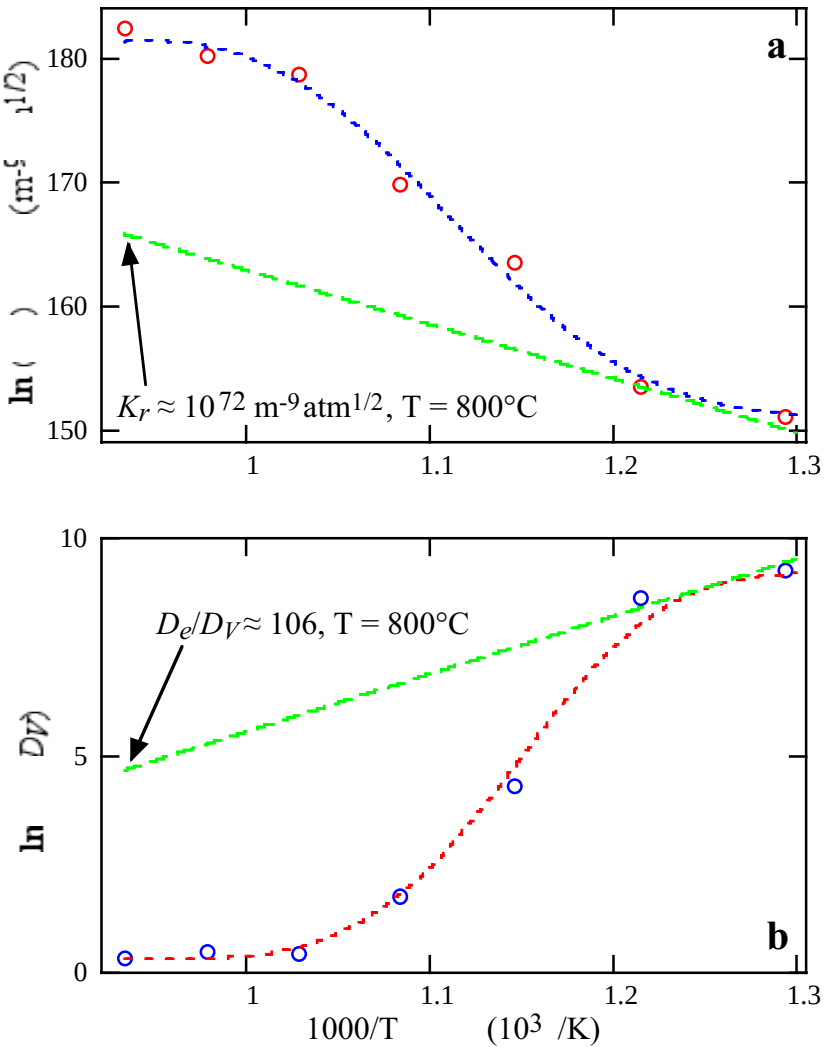

Figure 4-15. Plots of (a) K_r and (b) D_e/D_V versus reciprocal temperature. K_r and D_e/D_V values are those used in fitting the model (Figures 4-8 to 4-14). The dashed lines are for visual guidance and the straight lines indicate probable slopes without the impact of Pt electrodes, defect associates [36] and electrode overpotential.

characteristics of the SDC surface as they relate to K_r and D_e/D_V. The second examines the sensitivity of K_r and D_e/D_V to experimental error.

Electrode Effects. Figure 4-16a shows surface sites where the oxygen exchange can occur distributed across the surface of the SDC sample in what may be described as their *normal* states (i.e., before application of the electrodes). When electrodes are introduced, (see Figure 4-16b) the nature of many of the surface sites changes. At the SDC-Pt-gas interface, (i.e., the triple-phase boundary) the oxygen exchange reaction is enhanced significantly because, for the cathodic reaction (i.e., oxygen incorporation), adsorbed oxygen species (from the gas phase) can

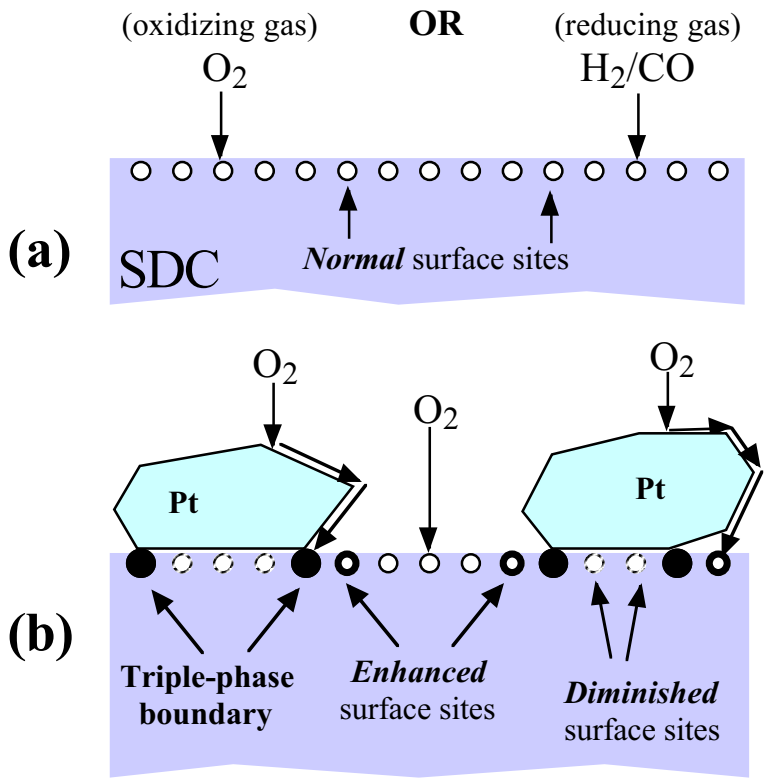

Figure 4-16. Comparison of the SDC-gas and SDC-Pt-gas interfaces showing: (a) *Normal* oxygen exchange surface sites for SDC in an oxidizing or a reducing gas, and (b) *Enhanced* and *diminished* oxygen exchange surface sites and triple phase (SDC-Pt-gas) boundaries.

obtain electron(s) readily (in comparison to SDC alone) from the metal phase. Adsorbed oxygen species are then transferred into a vacant oxygen site on the SDC (the ceramic phase) surface. This process is reversed for the anodic reaction (i.e., oxygen release) where oxygen atoms leave oxygen sites in the ceramic phase, release electrons to the metal phase and then react with the gas phase[8]. The oxygen exchange reaction is further catalyzed by the platinum, which adsorbs oxygen (and, potentially, species from the reducing gas) more readily than SDC [40]. The adsorbed oxygen (cathode reaction) migrates to the triple-phase boundary or even to surface sites in its neighborhood that benefit from the spreading of electrons across the surface from the triple phase boundaries (i.e., the *enhanced* surface sites depicted in Figure 4-16b).

As temperature increases the (electrochemical) resistance of the electrodes (to ionic transport), and therefore the electrode overpotential, decreases. In addition, the electronic conductivity of the electrolyte increases with temperature, thereby reducing Φ_{oc} and t'_{ion}. Both

[8] This is a highly simplified description. The steps for the anodic reaction are very complex and involves several steps that have not yet been identified without ambiguity. A primary source of uncertainty for the anodic reaction is the presence (theoretically) of numerous paths for the reaction between fuel and oxygen species [40].

have an effect on the performance of the SOFC, but the dominance of one over the other is dependent on the associated activation energies. Further discussion of these effects may be found in References 36, 40, 50 and 51.

As the temperature lowers, the significance of electrode overpotentials increases and becomes just as important as the change in K_r. In *open-circuit* (I_{ext} = 0) conditions the dominant contributor to the electrode overpotential is slow electrocatalytic (charge transfer) reactions at the electrodes. At high enough temperatures, the electrocatalytic reactions are fast and the electrode overpotential can be neglected. This is not true at lower temperatures. As temperatures decrease, the charge transfer rate at the interface slows causing an accumulation of charged oxygen species near the reaction sites. The accumulation creates an electric field that slows down and eventually stops other charged oxygen species from approaching the reaction sites. Thermodynamically, the material should still be able to reach thermodynamic equilibrium (i.e., the charge transfer reactions will take place if given enough time). However, if the reaction kinetics are slow enough, thermodynamic equilibrium will not be attained. Consequently, the effective oxygen potential gradient and, therefore, the *open-circuit* potential, across the SDC sample is less than that predicted by thermodynamics.

Where possible, electrodes are designed to minimize the overpotential. The Pt electrodes on the sensor are specially designed to optimize the performance of the sensor by minimizing the electrode overpotential. In contrast, our simple porous Pt electrodes have not yet been optimized. Hence they produce a comparably larger overpotential, in similar conditions, than the electrodes on the commercial oxygen sensor.

Experimental Errors. The values of K_r in Table 4-2 show that the difference between K_r from the data of Kobayashi *et al*. [43] and that calculated from the model, at 800 °C is large. However, they also show that the corresponding values for ln K_r ($\propto \Delta G_r$) are within 10% of each other. The reason that this is significant is that the actual measured quantities in the experiment are Φ_{oc} and temperature and Φ_{oc} is proportional to **ln** K_r as shown below:

$$\mathbf{ln}\frac{K_r}{K_r^*} = -\frac{\Delta G_r}{kT} = -\frac{2z_V q\Phi_{oc}}{kT} \tag{4.6}$$

where K_r^* is a unit bearing pre-exponential (made necessary by the definition of K_r in Eq. (3.14). Consequently, experimental errors made in the measurement of Φ_{oc} are magnified (exponentially) in the calculation of K_r. Moreover, from error analysis

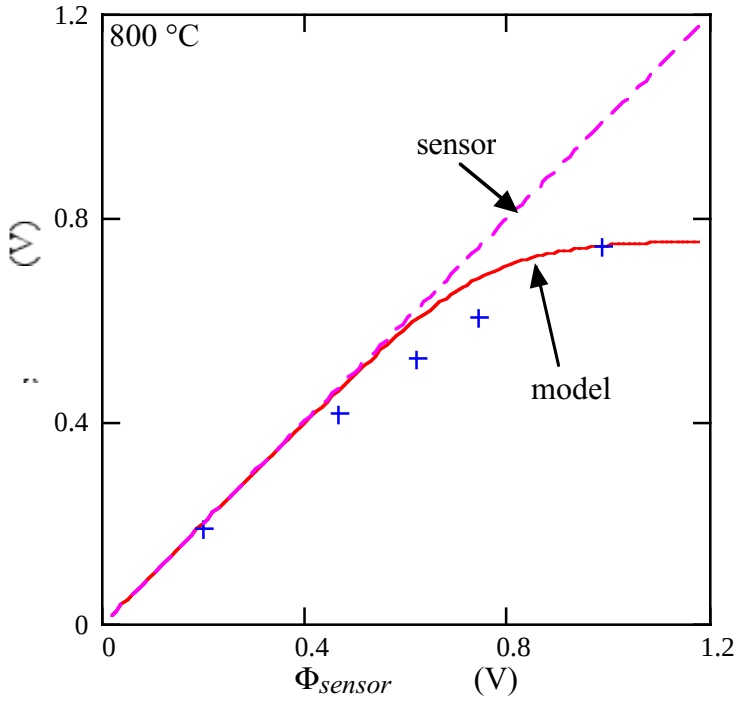

Figure 4-17. *Open-circuit* potential, Φ_{oc}, versus Φ_{sensor} (Φ_{th}) at 800 °C without "fitting". The model (—) was fitted to experimental data (+) (sensor (---)) for the fuel cell using the K_r value obtained from the data of Kobayashi *et al.* [43] and the corresponding D_e/D_V ratio in Table 3-2.

$$\frac{\Delta_{err}\left(\ln K_r - \ln K_r^*\right)}{\ln K_r - \ln K_r^*} = \frac{\Delta_{err}\Phi_{oc}}{\Phi_{oc}} + \frac{\Delta_{err}T}{T} \tag{4.7}$$

where the symbol Δ_{err} indicates the error (so $\Delta_{err}y$ is the error in y).

For the experiment, $\Delta_{err}\Phi_{oc}/\Phi_{oc}$ (i.e., the fractional error) is between ~0.05 and ~0.1 while $\Delta_{err}T/T$ lies between ~0.01 and ~0.05. Therefore, the fractional error in $\ln K_r/K_r^*$ falls in the range 0.06 to 0.15 (i.e., 6% to 15%). This result shows that, if experimental errors are included, the K_r (or perhaps more appropriately $\ln K_r$) value obtained from Kobayashi *et al.* [43] is approximately equal to that obtained from the Φ_{oc} experiments outlined above. This argument is further corroborated by the good fit, Figure 4-17, obtained when the model is applied to experimental data using the K_r value from Kobayashi *et al.* [43] and the corresponding Θ from Table 3-2.

Finally, there is also the effect of the P_{O_2} range in which the experiments were conducted. The data of Kobayashi *et al.* [43] (at 800 °C) spans a P_{O_2} range from ~$10^{-17.55}$ atm. to ~$10^{-20.5}$ atm. while for the same temperature the Φ_{oc} experiment spans a range of ~10^{-4} to ~10^{-19} atm. In

addition, the data of Kobayashi *et al*. [43], in Table 4, shows an increasing trend for K_r as P_{O_2} decreases. Together, the implication is that had Kobayashi *et al*. [43] taken data over a larger range then, perhaps, a higher average K_r value would have been obtained from their data. This result is substantiated somewhat when the model is applied to the Φ_{oc} data using the K_r (and the corresponding D_e/D_V ratio) value calculated from the data of Kobayashi *et al*. [43] shown in Figure 4-17. The data point, corresponding to $P_0 \approx 10^{-19}$ atm., falls exactly on the modeled curve.

5. BILAYER MODEL

In this section, the bilayer model presented earlier is thoroughly revised and extended to closed-circuit conditions. Models that we developed elsewhere [36, 52] are used to obtain the relationship between the thickness ratio of the constituent layers of the SDC\ESB bilayer and (in *open-circuit* conditions) the chemical potential drop or (in *closed-circuit* conditions) the electrical potential drop across either layer. By having such a relationship, the relative thickness of the SDC and ESB layers may be optimized to maximize total conductivity of the bilayer and the protection of ESB from decomposition under a range of operating conditions.

5.1 OPEN-CIRCUIT CONDITIONS AND THICKNESS RATIO

Mechanistically, the diffusion of oxygen occurs by oxygen ions jumping from an occupied site to an adjacent vacant site in the MIECs oxygen sub-lattice. Also, oxygen vacancies and electrons/holes travel together in an electrically neutral packet (see Figure 3-1), as discussed earlier in section 3.2. Thus, the fluxes of the various species are related as follows:

$$2z_V j_{O_2} = -z_V j_V = z_{e,h} j_{e,h} \tag{5.1}$$

where $z_{e,h}$ is the charge equivalence of electrons (-1) or holes (+1).

For the bilayered electrolyte, the flux of any species is the same in both layers, in steady state conditions. Also, Eq. (5.1) shows that it is necessary to consider the flux of only one species. Therefore, for a bilayer consisting of an ε layer (SDC) and a δ layer (ESB), we have:

$$j_{O_2}^{\varepsilon} = j_{O_2}^{\delta} \tag{5.2a}$$

$$j_V^{\varepsilon} = j_V^{\delta} \tag{5.2b}$$

or

$$z_{e,h} j_{e,h}^{\varepsilon} = z_{e,h} j_{e,h}^{\delta} \tag{5.2c}$$

where the superscript denotes the layer. At this point two approaches are taken. We have obtained [36] expressions for j_V based on Wagner's equation [53] (the "thermodynamic" model) and the transport equations listed in section 3.1 (the transport model). Both approaches are used and the results compared below. However, we expect that the expression for j_V derived from the transport equations [36] to be more accurate since fewer assumptions were made in its development. Nevertheless, the accuracy of both models (transport and thermodynamic) may, indirectly, be validated by comparing the results of both approaches.

5.1.1 "Thermodynamic" Approach

The oxygen vacancy and electron conductivity of the *n*-type MIEC, SDC, as a function of P_{O_2}, is given by[9] [36]:

$$\sigma_V(P) = z_V^2 q^2 \frac{D_V}{k_B T}\left[\tfrac{3}{4} K_r^{\frac{1}{2}} P^{-\frac{1}{4}} + \left(\tfrac{1}{2} c_A\right)^{\frac{3}{2}}\right]^{\frac{2}{3}} \tag{5.3}$$

and

$$\sigma_e(P) = z_e^2 q^2 \frac{D_e}{k_B T} K_r^{\frac{1}{2}} P^{-\frac{1}{4}}\left[\tfrac{3}{4} K_r^{\frac{1}{2}} P^{-\frac{1}{4}} + \left(\tfrac{1}{2} c_A\right)^{\frac{3}{2}}\right]^{-\frac{1}{3}} \tag{5.4}$$

Similarly, the oxygen vacancy and electron-hole conductivity of the *p*-type MIEC, ESB, as a function of P_{O_2}, is given by[10] [36, 38]:

$$\sigma_V(P) = \frac{z_V^2 q^2 D_V}{16 k_B T}\left[\left(K_m P^{\frac{1}{2}} + 8c_A\right)^{\frac{1}{2}} - K_m^{\frac{1}{2}} P^{\frac{1}{4}}\right]^2 \tag{5.5}$$

and

[9] For $P_{O_2} < \sim 1$ atm. the electronic conduction in SDC (and GDC) is *n*-type [36, 47].

[10] For P_{O_2} values above its decomposition potential, the electronic conduction in ESB is *p*-type [36, 38 - 41].

$$\sigma_h(P) = \frac{z_h^2 q^2 D_h}{4k_B T}\left(-K_m P^{\frac{1}{2}} + \sqrt{8c_A K_m P^{\frac{1}{2}} + K_m^2 P}\right) \tag{5.6}$$

where K_m is the external equilibrium constant [36, 38] for ESB and the subscript "*h*" refers to electron-holes. It should also be noted that in applying these formulae to ESB the erbium and bismuth cations are treated as aliovalent acceptor "dopants" sitting in a fluorite lattice [54].

Wagner's equation [53] for oxygen flux may be combined with Eq. (5.1) with the result:

$$-j_{O_2} = \frac{k_B T}{4^2 q^2 L^{\varepsilon}} \cdot \int_{P_0}^{P_I} \frac{\sigma_V^{\varepsilon}(P)\sigma_e^{\varepsilon}(P)}{\sigma_V^{\varepsilon}(P) + \sigma_e^{\varepsilon}(P)} \cdot \frac{dP}{P} = \frac{k_B T}{4^2 q^2 L^{\delta}} \cdot \int_{P_I}^{P_L} \frac{\sigma_V^{\delta}(P)\sigma_h^{\delta}(P)}{\sigma_V^{\delta}(P) + \sigma_h^{\delta}(P)} \cdot \frac{dP}{P} \tag{5.7a}$$

which may be rewritten as

$$\tau(P_I) = \frac{L^{\varepsilon} j_{O_2}^{\varepsilon}}{L^{\delta} j_{O_2}^{\delta}} = \frac{L^{\varepsilon}}{L^{\delta}} = \frac{\int_{P_0}^{P_I} \frac{\sigma_V^{\varepsilon}(P)\sigma_e^{\varepsilon}(P)}{\sigma_V^{\varepsilon}(P) + \sigma_e^{\varepsilon}(P)} \cdot \frac{dP}{P}}{\int_{P_I}^{P_L} \frac{\sigma_V^{\delta}(P)\sigma_h^{\delta}(P)}{\sigma_V^{\delta}(P) + \sigma_h^{\delta}(P)} \cdot \frac{dP}{P}} \tag{5.7b}$$

where τ is defined as the SDC\ESB ($\delta\backslash\varepsilon$) thickness ratio of the two layers, L is the thickness (i.e., length) of a layer and the subscripts "0" and "L" refer to the conditions at x = 0 (low P_{O_2} or fuel/reducing side of the SOFC/electrolyte) and x = L (high P_{O_2} or air/oxidizing side of the SOFC/electrolyte); the subscript "*I*" refers to the interface between the two constituent layers.

The integral in the denominator in Eq. (5.7) exists, but it is very unwieldy. For ESB, $K_m > 10^{19}$ $m^{-3}atm.^{-1/2}$ and $c_A = 2.2 \times 10^{28}$ m^{-3} [36], consequently, in the range of P_{O_2} (10^{-20} atm. to 0.21 atm.) and T (500 °C to 800 °C) under investigation

$$8c_A >>> K_m P^{1/2}$$

and Eqs. (5.5) and (5.6) reduce to

$$\sigma_V(P) = \frac{z_V^2 q^2 D_V c_A}{2k_B T} \tag{5.5b}$$

and

$$\sigma_h(P) = \frac{z_h^2 q^2 D_h}{k_B T} K_m^{\frac{1}{2}} P^{\frac{1}{4}} \left(\tfrac{1}{2} c_A\right)^{\frac{1}{2}} \tag{5.6b}$$

With this simplification the denominator in Eq. (5.7) is easily integrated and Eq. (5.7) becomes

$$\tau(P_I) = \frac{\dfrac{z_e^2 D_e^{\varepsilon}}{1+\frac{4}{3}\Theta^{\varepsilon}} \left\{ \dfrac{c_V^{\varepsilon}(P)}{2} - \dfrac{\Omega^2}{6} \ln \dfrac{c_V^{\varepsilon}(P) - \Omega\sqrt{c_V^{\varepsilon}(P)} + \Omega^2}{\left(\sqrt{c_V^{\varepsilon}(P)} + \Omega\right)^2} - \dfrac{\Omega^2}{\sqrt{3}} \tan^{-1} \dfrac{2\sqrt{c_V^{\varepsilon}(P)} - \Omega}{\Omega\sqrt{3}} \right|_{P_0}^{P_I} \right\}}{-\dfrac{z_h^2 D_h^{\delta} c_A^{\delta}}{8\Theta^{\delta}} \cdot \left\{ \ln\left(1 + \Theta^{\delta}\left(\tfrac{1}{2} c_A^{\delta}\right)^{-\frac{1}{2}} K_m^{\frac{1}{2}} P^{\frac{1}{4}}\right) \right|_{P_I}^{P_L} \right\}} \tag{5.7c}$$

where

$$\Omega = -\tfrac{4}{3}\Theta^{\frac{1}{3}} \left(\tfrac{1}{2} c_A^{\varepsilon}\right)^{\frac{1}{2}} \left(1 + \tfrac{4}{3}\Theta\right)^{-\frac{1}{3}} \tag{5.8}$$

$$\Theta^{\varepsilon,\delta} = \frac{z_{e,h}^2 D_{e,h}}{z_V^2 D_V} \tag{5.9}$$

and, from Eq. (3.15),

$$c_V^{\varepsilon}(P) = \left[\tfrac{3}{4} K_r^{\frac{1}{2}} P^{-\frac{1}{4}} + \left(\tfrac{1}{2} c_A^{\varepsilon}\right)^{\frac{3}{2}}\right]^{\frac{2}{3}} \tag{5.10}$$

5.1.2 "Transport" Approach

From our earlier work [36], j_V, as derived from the transport model, is given by:

$$j_V = \frac{D_V D_{e,h}}{L} \left[\frac{\left(z_V - z_{e,h}\right)\left(c_{V_0} - c_{V_L}\right)}{z_V D_V - z_{e,h} D_{e,h}} + \frac{z_{e,h}\left(D_{e,h} - D_V\right) c_A}{\left(z_V D_V - z_{e,h} D_{e,h}\right)^2} \ln \frac{z_V^2 D_V c_{V_L} + D_{e,h} c_{e,h_L}}{z_V^2 D_V c_{V_0} + D_{e,h} c_{e,h_0}} \right] \tag{5.11}$$

Combining this equation with Eq. (5.1) and rearranging yields

$$\tau(P_I) = \frac{D_V^{\varepsilon} D_e^{\varepsilon} \left[\frac{(z_V - z_e)\left(c_{V_0}^{\varepsilon} - c_{V_I}^{\varepsilon}\right)}{z_V D_V^{\varepsilon} - z_e D_e^{\varepsilon}} + \frac{z_e \left(D_e^{\varepsilon} - D_V^{\varepsilon}\right) c_A^{\varepsilon}}{\left(z_V D_V^{\varepsilon} - z_e D_e^{\varepsilon}\right)^2} \ln \frac{\left(z_V D_V^{\varepsilon} - z_e D_e^{\varepsilon}\right) z_V c_{V_I}^{\varepsilon} + z_e D_e^{\varepsilon} c_A^{\varepsilon}}{\left(z_V D_V^{\varepsilon} - z_e D_e^{\varepsilon}\right) z_V c_{V_0}^{\varepsilon} + z_e D_e^{\varepsilon} c_A^{\varepsilon}} \right]}{D_V^{\varepsilon} D_h^{\delta} \left[\frac{(z_V - z_h)\left(c_{V_I}^{\delta} - c_{V_L}^{\delta}\right)}{z_V D_V^{\varepsilon} - z_h D_h^{\delta}} + \frac{z_h \left(D_h - D_V^{\varepsilon}\right) c_A^{\delta}}{\left(z_V D_V^{\varepsilon} - z_h D_h^{\delta}\right)^2} \ln \frac{\left(z_V D_V^{\varepsilon} - z_h D_h^{\delta}\right) z_V c_{V_L}^{\delta} + z_h D_h^{\delta} c_A^{\delta}}{\left(z_V D_V^{\varepsilon} - z_h D_h^{\delta}\right) z_V c_{V_I}^{\delta} + z_h D_h^{\delta} c_A^{\delta}} \right]} \quad (5.12)$$

where

$$c_{V_k}^{\varepsilon}(P_k) = \left[\tfrac{3}{4} K_r^{\frac{1}{2}} P_k^{-\frac{1}{4}} + \left(\tfrac{1}{2} c_A^{\varepsilon} \right)^{\frac{3}{2}} \right]^{\frac{2}{3}} \quad (5.13)$$

$$c_{V_k}^{\delta}(P_k) = \frac{1}{16} \left[\left(K_m P_k^{\frac{1}{2}} + 8 c_A^{\delta} \right)^{\frac{1}{2}} - K_m^{\frac{1}{2}} P_k^{\frac{1}{4}} \right]^2 \quad (5.14)$$

and the subscript $k = 0, I, L$.

5.1.3 Results and Discussion

The results of the model for *open-circuit* conditions are summarized in Table 5-1. Table 5-1 shows that there is very close agreement (enough, perhaps, to be indistinct experimentally) between the "thermodynamic" model—Eq. (5.7c)—and the "transport" model—Eq. (5.12)—giving credence to the propriety of both approaches.

In the table, the values for K_r are calculated from the thermogravimetric data of Kobayashi *et al*. [43] and from fitting Eq. (3.19) to our experimental data (section 4.3). At 500 °C the value of K_r is adjusted slightly to reflect t'_{ion} = 0.9 for SDC, as obtained by other researchers [19]. We expect that value wasn't achieved in our experiments due to high electrode overpotentials from the Pt-paste electrodes. This was discussed in section 4.3.

Similarly, the values for K_m are calculated from Eq. (3.19) using literature values [55 - 57] for t'_{ion} (Φ_{oc}/Φ_{th}) and assuming $2D_V(\text{SDC}) \approx D_V(\text{ESB})$ [52] and $D_e(\text{SDC}) \approx D_h(\text{ESB}) = D_{e,h}$ (therefore $\Theta^{\varepsilon} = 0.5\Theta^{\delta}$). In addition, $c_A^{\varepsilon} = 5 \times 10^{27}$ m^{-3}, $c_A^{\delta} = 22 \times 10^{27}$ m^{-3}, $P_L = 0.21$ atm. and $P_0 = 10^{-20}$ atm. in all calculations made in this section. Understandably, there exists some variability in the literature [19, 55 - 58] for the value t'_{ion} and although this variability is small (< 3%) it does have a significant impact on the predictions of the model for τ.

Table 5-1. τ^* and ASR (L = 10 μm) at 800 °C and 500 °C in *open-circuit* conditions.

T (°C)	K_r ($m^{-9}atm.^{1/2}$)	K_m ($m^{-3}atm.^{-1/2}$)	$\Theta_{SDC}(\Theta_{ESB})$	t'_{ion} (SDC)	t'_{ion} (ESB)	τ^*_{thermo}	$\tau^*_{transport}$	ASR†† (Ωcm^2)
800	†1.0×10^{72}	2.0×10^{23}	‡‡11.5(5.75)	0.80	0.98	17.2	17.8	0.010
800	†1.0×10^{72}	8.4×10^{23}	‡‡11.5(5.75)	0.80	0.96	8.5	8.8	0.010
800	‡1.4×10^{79}	2.0×10^{23}	‡0.35(5.75)	0.75	0.98	18000	24000	0.011
800	‡1.4×10^{79}	8.4×10^{23}	‡0.35(5.75)	0.75	0.96	9100	12000	0.011
500	‡4.0×10^{65}	1.0×10^{18}	‡2570(1285)	0.84	0.99	9.8	9.8	0.12
500	‡4.0×10^{65}	9.3×10^{18}	‡2570(1285)	0.84	0.97	3.2	3.2	0.11
500	5.1×10^{64}	1.0×10^{18}	‡2570(1285)	0.90	0.99	4.6	4.6	0.12
500	5.1×10^{64}	9.3×10^{18}	‡2570(1285)	0.90	0.97	1.53	1.53	0.10

† Calculated from thermogravimetric data of Kobayashi *et al.* [43] in section 3.4.1.

‡ Obtained from fitting Eq. (3.19) to experimental data—see section 4.3 and Table 4-2.

†† ASR, SDC: 0.011 Ωcm^2 at 800 °C; 0.13 Ωcm^2 at 500 °C; ESB: 0.0024 Ωcm^2 at 800 °C; 0.048 Ωcm^2 at 500 °C.

‡‡ Calculated from Eq. (3.19) to concur with literature values [55 - 57] for t'_{ion} (as discussed in text).

The area-specific resistance (ASR) of the bilayered electrolyte is included in Table 5-1 to evaluate how low of an ASR is possible in *open-circuit* conditions. The total ASR of the bilayer, (if the cross-sectional area is the same for both layers) is given by:

$$ASR = \left(\frac{L^{\varepsilon}}{\sigma^{\varepsilon}} + \frac{L^{\delta}}{\sigma^{\delta}} \right) \tag{5.15a}$$

However, since $\tau = L^{\varepsilon}/L^{\delta}$ and the total thickness of the bilayer, $L = L^{\varepsilon} + L^{\delta} = (1 + 1/\tau)L^{\varepsilon}$ then

$$ASR = \frac{L}{1+\tau}\left(\frac{\tau}{\sigma^{\varepsilon}} + \frac{1}{\sigma^{\delta}} \right) \tag{5.15b}$$

For large τ (i.e., $\tau >$ ~2 at 800 °C and $\tau >$ ~3 at 500 °C) Eq. (5.15) reduces to

$$ASR \approx \frac{L}{\sigma^{\varepsilon}} \tag{5.15b}$$

—i.e., the ASR depends solely on the conductivity of SDC. For small τ (i.e., $\tau <$ ~0.02 at 800 °C and $\tau <$ ~0.03 at 500 °C) Eq. (5.15) reduces to

$$ASR = \frac{L}{\sigma^{\delta}} \qquad (5.15b)$$

—i.e., the ASR depends solely on the conductivity of ESB.

Using K_r calculated from the data of Kobayashi *et al*. [43], the optimal (minimum) thickness ratio, τ^*, to prevent decomposition of the ESB layer—ESB decomposes for $P_I \leq \sim 10^{-9}$ atm. [55 - 57] at 800 °C—at the SDC-ESB interface, is ~9 or ~18 depending on whether t'_{ion} is 0.98 or 0.96 for ESB [55 - 57]. Samaria-doped ceria is more electronically conductive than ESB and so it permeates oxygen more easily. If the layers had the same thickness, the chemical potential drop would be greater across the more *resistive* layer (analogous to an electrical circuit). Consequently, to increase the chemical potential drop across the SDC layer and offer protection to the ESB layer requires a thickening of the SDC layer relative to the ESB layer. Accordingly, if the ESB layer is more permeable (i.e., smaller t'_{ion}) then the chemical potential drop across it is smaller and a thinner layer of SDC (smaller τ^*) can provide the same protection. By extension, this suggests that there is a trade-off between having a bilayer that produces near theoretical open-circuit potential and one that has the highest conductivity (due to the thinner SDC layer).

At 800 °C the ASR (for L = 10 μm) of the bilayered electrolyte is approximately equal to that of a single-layer SDC electrolyte (i.e., the ESB layer has a negligible effect on the ASR of the bilayer). (At 800 °C, the ASR is 0.011 Ωcm^2 and 0.0024 Ωcm^2 for SDC and ESB respectively.) This result is a consequence of the high τ^* values necessitated by the oxygen permeability of SDC and though this result is not ideal, it is still has promise because the ESB layer blocks conduction of electrons through the bilayer and, thereby should increase the efficiency of power delivery to an external load compared to SDC alone.

The results obtained using K_r and Θ calculated from our experimental data for SDC at 800 °C, section 4.3, reflects the difficulties we experienced with the Pt-paste electrodes and emphasizes the need to separate electrode effects from the measured value of Φ_{oc} in order to accurately determine the performance of the electrolyte. Although more reasonable, the K_r and Θ values calculated from our experimental data at 500 °C likewise suffer from electrode effects, in this case evidenced in the lower than expected t'_{ion}.

At 500 °C, ESB decomposes at $P_I \leq \sim 10^{-16}$ atm. [55 - 57] and τ^* ranges from ~1.5 to ~10 depending on whether t'_{ion} is 0.84 or 0.90 for SDC and 0.98 or 0.96 for ESB [55 - 57]. Again this value is approximately equal to that of a single-layer SDC electrolyte alone. (At 500 °C, the ASR is 0.13 Ωcm^2 and 0.048 Ωcm^2 for SDC and ESB respectively.)

As Table 5-1 shows, improvement in τ^* depends largely on whether t'_{ion} for SDC increases more rapidly than t'_{ion} for ESB. Or if K_r (for SDC) reduces more rapidly with temperature than K_m (for ESB). The equilibrium constants are related to the free energies, ΔG_r and ΔG_m respectively, of the oxygen exchange reaction and temperature as follows:

$$\ln K_r = \ln K_r^\circ - \frac{\Delta G_r}{k_B} \cdot \frac{1}{T}$$

and

$$\ln K_m = \ln K_m^\circ - \frac{\Delta G_m}{k_B} \cdot \frac{1}{T}$$

where K°_r and K°_m are unit bearing pre-exponentials. The expressions above show that the equilibrium constant for the external equilibrium reaction (between the atmosphere and the material) that occurs more readily (i.e., has a higher free energy) will vary more strongly with (reciprocal) temperature. SDC is known to react (i.e., incorporate or release oxygen) more readily with the ambient atmosphere than ESB, because of its ability to produce electrons. Consequently, it is reasonable to expect that as the temperature is lowered K_r will decrease more rapidly than K_m—and hence t'_{ion} will increase more rapidly with declining temperature for SDC compared to ESB. Therefore, it is reasonable to expect more favourable values of τ^* as the temperature decreases.

In either case, the variability of τ^* due to the values of K°_r, K°_m and Θ (or t'_{ion}) result in an insignificant change in the performance factor, i.e., the ASR, of the bilayer. Therefore basing τ^* on the most conservative estimates of K°_r, K°_m and Θ (or t'_{ion}) will result in a very low ASR of ~0.01 at 800 °C and an acceptably low ASR of ~0.1 at 500 °C. Either ASR would enable a high power density SOFC if electrodes with suitable performance (i.e., low overpotential) were found.

5.2 CLOSED-CIRCUIT CONDITIONS AND THICKNESS RATIO

5.2.1 Model

For *closed-circuit* conditions, the principles and procedure are almost identical to those described and developed in the preceding sections for *open-circuit* conditions. However, there is one major difference. Specifically, in *closed-circuit* conditions, oxygen does not permeate through the MIEC by ambipolar diffusion, rather oxygen vacancies are transported at a rate

proportional to the external current. Consequently, it may not be as appropriate to speak of a P_{O_2} at the interface (nor at any other point in either MIEC layer). Since there is no longer a P_{O_2} at the interface, a new gauge is required to indicate the stability of the ESB layer.

In *open-circuit* conditions there is an oxygen chemical potential difference across each layer (equivalent to a difference in P_{O_2}). In *closed-circuit* conditions the oxygen chemical potential difference still exists between $x = 0$ and $x = L$, however inside any layer (i.e., for $0 < x < L$) it is replaced by defect chemical potential differences and electrical potential differences. Additionally, the electric potential is related to the defect concentration (and therefore the defect chemical potential) [36]. Altogether, this suggests that in *closed-circuit* conditions, the electric potential difference across the ESB layer should be a suitable gauge of the stability of ESB at the SDC-ESB interface.

At 800 °C, and with air on one side, an ESB electrolyte decomposes when the fuel side $P_{O_2} \leq \sim 10^{-9}$ atm. [55 - 57]. This corresponds to a (Nernst) potential difference of ~0.44 V. Therefore, if the electrical potential difference across the ESB layer is held below 0.4 V, then the ESB layer remains stable. Similarly, at 500 °C, with air on one side, an ESB electrolyte, decomposes when the fuel side $P_{O_2} \leq \sim 10^{-16}$ atm. [55 - 57] corresponding to a (Nernst) potential difference of ~0.6 V (since $P_L = 0.21$ atm. on the oxidizing side). Therefore, the ESB layer should remain stable when the electrical potential difference across it is less than 0.6 V.

To obtain an expression for $\tau(\Delta\phi)$ in *closed-circuit* conditions, consider the *closed-circuit* defect flux and the spatially varying Galvani potential, which are given by [36]:

$$-\frac{j_V}{D_V} + -\frac{j_{e,h}}{D_{e,h}} = \frac{z_V - z_{e,h}}{z_{e,h}}\gamma = \frac{z_V - z_{e,h}}{z_{e,h}} \cdot \frac{\phi_L - \phi_0 + \lambda\left(c_{V_0} - c_{V_L}\right)}{\lambda L} \tag{5.16}$$

and

$$\phi_L - \phi_0 = \frac{z_V \frac{j_V}{D_V} + z_{e,h}\frac{j_{e,h}}{D_{e,h}}}{z_V\left(z_V - z_{e,h}\right)f\gamma} \ln \frac{c_{V_L} + \frac{j_V}{z_V D_V f \lambda \gamma}}{c_{V_0} + \frac{j_V}{z_V D_V f \lambda \gamma}} \tag{5.17}$$

where, ϕ is potential, $f = q/k_B T$ and

$$\lambda = \frac{z_V - z_{e,h}}{z_{e,h} c_A f} \tag{5.18}$$

Since the ESB layer is a poor electronic conductor it blocks the flux of electrons and holes. Additionally, as one moves away from *open-circuit* conditions, the electronic flux inside the MIEC decreases. Hence, Eqs. (5.16) and (5.17) reduce to

$$-\frac{j_V}{D_V} \approx \frac{z_V - z_{e,h}}{z_{e,h}}\gamma = \frac{z_V - z_{e,h}}{z_{e,h}} \cdot \frac{\phi_L - \phi_0 + \lambda\left(c_{V_0} - c_{V_L}\right)}{\lambda L} \tag{5.16b}$$

and

$$\phi_L - \phi_0 \approx \frac{z_V j_V}{z_V\left(z_V - z_{e,h}\right)D_V f\gamma}\ln\frac{c_{V_L} + \dfrac{j_V}{z_V D_V f\lambda\gamma}}{c_{V_0} + \dfrac{j_V}{z_V D_V f\lambda\gamma}} = -\frac{1}{z_{e,h} f}\ln\frac{c_{V_L} - \dfrac{c_A}{z_V}}{c_{V_0} - \dfrac{c_A}{z_V}} \tag{5.17b}$$

Combining Eqs. (5.1), (5.16b) and (5.17b) yields

$$\tau(\Delta\phi) = \frac{D_V^{\varepsilon}\dfrac{z_V - z_e}{z_e}\left\{\dfrac{\Delta\phi^{\varepsilon}}{\lambda^{\varepsilon}} + \left(c_{V_0}^{\varepsilon} - \dfrac{c_A^{\varepsilon}}{z_V}\right)\left[1 - \exp\left(-z_e f\Delta\phi^{\varepsilon}\right)\right]\right\}}{D_V^{\delta}\dfrac{z_V - z_h}{z_h}\left\{\dfrac{\Delta\phi^{\delta}}{\lambda^{\delta}} - \left(c_{V_L}^{\delta} - \dfrac{c_A^{\delta}}{z_V}\right)\left[1 - \exp\left(z_h f\Delta\phi^{\delta}\right)\right]\right\}} \tag{5.19}$$

where

$$\Delta\phi^{\varepsilon} = \phi_I - \phi_0 \tag{5.20}$$

and

$$\Delta\phi^{\delta} = \phi_L - \phi_I \tag{5.21}$$

Additionally, by definition [36]

$$\Delta\Phi = -\Delta\phi = -\left(\phi_L - \phi_0\right) \tag{5.22}$$

where $\Delta\Phi$ is the potential across a single layered electrolyte. Thus, for the bilayer one may write

$$\Delta\Phi = \Delta\Phi^{\varepsilon} + \Delta\Phi^{\delta} = -\left(\phi_I - \phi_0\right) - \left(\phi_L - \phi_I\right) = -\Delta\phi^{\varepsilon} - \Delta\phi^{\delta} \tag{5.23}$$

Substituting Eq. (5.23) for $-\Delta\phi^{\varepsilon}$, into Eq. (5.19) yields

$$\tau(\Delta\phi^{\delta}) = -\frac{D_V^{\varepsilon}\frac{z_V - z_e}{z_e}\left\{\frac{\Delta\Phi + \Delta\phi^{\delta}}{\lambda^{\varepsilon}} - \left(c_{V_0}^{\varepsilon} - \frac{c_A^{\varepsilon}}{z_V}\right)\left[1 - \exp\left(z_e f\left(\Delta\Phi + \Delta\phi^{\delta}\right)\right)\right]\right\}}{D_V^{\delta}\frac{z_V - z_h}{z_h}\left\{\frac{\Delta\phi^{\delta}}{\lambda^{\delta}} - \left(c_{V_L}^{\delta} - \frac{c_A^{\delta}}{z_V}\right)\left[1 - \exp\left(z_h f\Delta\phi^{\delta}\right)\right]\right\}} \tag{5.24}$$

Finally, the external equilibrium constants K_r and K_m—Eqs. (5.13) and (5.14)—are functions of $\Delta\Phi^{\varepsilon}$ and $\Delta\Phi^{\delta}$ respectively and are given by [36]:

$$K_r(\Delta\Phi) = K_r^* \exp\left(-\frac{\Delta G_r \pm z_e q\Delta\Phi}{kT}\right) \tag{5.25}$$

and

$$K_m(\Delta\Phi) = K_m^* \exp\left(-\frac{\Delta G_m \pm z_h q\Delta\Phi}{kT}\right) \tag{5.26}$$

5.2.2 Results and Discussion

The results of the model for *closed-circuit* conditions are summarized in Table 5-2, where τ^* is referenced to $\Delta\Phi = \Phi_{th}$ (i.e., *short-circuit* conditions, [36] where the voltage drop across either layer is greatest). The optimal thickness ratio to prevent decomposition of the ESB layer, in *closed-circuit* conditions—ESB decomposes for $-\Delta\phi^{\delta} \geq \sim 0.4$ V at 800 °C and $-\Delta\phi^{\delta} \geq \sim 0.6$ V at 500 °C—is a function of the operating conditions. If the internal electronic current (the *leakage* current, I_e) is small, then external current (I_{ext}) is directly proportional to the internal ionic current (I_V). Neglecting the effect of the electrodes,

$$\Delta\Phi = t'_{ion}\Phi_{th} - I_{ext}R_{load} \tag{5.27}$$

where R_{load} is the resistance of the external circuit. In *short-circuit* conditions, see Figure 5-1, $R_{load} = 0$ and $t'_{ion} \approx 1$ [36] (because $I_e \approx 0$). (Under this condition, the internal ionic current is maximum and $\Phi_{th} = I_V \times R_{int}$.) Therefore, the largest values of $\Delta\Phi$ and $-\Delta\phi$ occur in *short-circuit*

Table 5-2. τ^*—with reference to $\Delta\Phi = \Phi_{th}$ (*short-circuit* conditions)—and ASR (L = 10 μm) at 800 °C and 500 °C in *closed-circuit* conditions.

T (°C)	K_r ($m^{-9}atm.^{1/2}$)	K_m ($m^{-3}atm.^{-1/2}$)	$\Theta_{SDC}(\Theta_{ESB})$	τ^*	ASR†† (Ωcm^2)
800	†1.0×10^{72}	2.0×10^{23}	‡‡11.5(5.75)	0.42	0.005
800	‡1.0×10^{72}	8.4×10^{23}	‡‡11.5(5.75)	0.42	0.005
500	‡4.0×10^{65}	1.0×10^{18}	‡2570(1285)	0.027	0.05
500	‡4.0×10^{65}	9.3×10^{18}	‡2570(1285)	0.027	0.05
500	5.1×10^{64}	1.0×10^{18}	‡2570(1285)	0.027	0.05
500	5.1×10^{64}	9.3×10^{18}	‡2570(1285)	0.027	0.05

† Calculated from thermogravimetric data of Kobayashi *et al.* [43] in section 3.4.1.

‡ Obtained from fitting Eq. (3.19) to experimental data—see section 4.3 and Table 4-2.

†† ASR, SDC: 0.011 Ωcm^2 at 800 °C; 0.13 Ωcm^2 at 500 °C; ESB: 0.0024 Ωcm^2 at 800 °C; 0.048 Ωcm^2 at 500 °C.

‡‡ Calculated from Eq. (3.19) to concur with literature values [55 - 57] for t'_{ion} (as discussed in text).

conditions because that is the point at which the external circuit draws the largest current from the fuel cell—and I_e is the smallest. In this context, τ^* is then the optimal thickness ratio with respect to short-circuit conditions and at 800 °C, $\tau^* \approx 0.42$ while at 500 °C $\tau^* \approx 0.027$. This is in stark contrast to the results obtained above for *open-circuit* conditions, Table 5-1. The difference however is readily explained by considering that in *open-circuit* conditions ESB is more *resistive* than SDC to the transport (permeation) of oxygen because of the low concentration of electronic species in ESB.

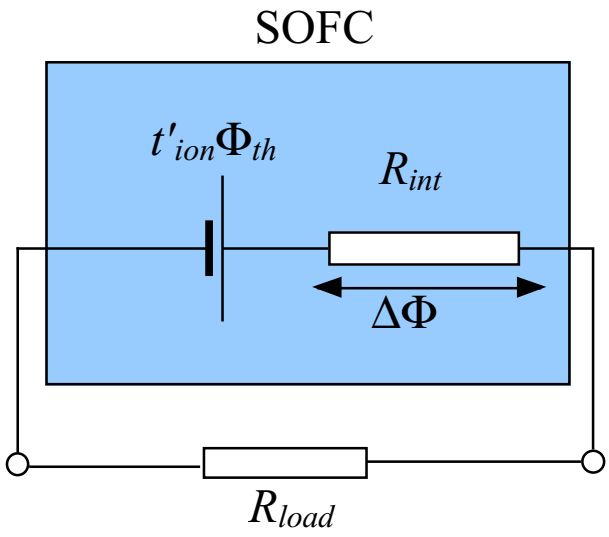

Figure 5-1. Equivalent circuit for SOFC

In *closed-circuit* conditions (where the ionic and electronic species are no longer constrained to travel together) SDC is more resistive than ESB to the transport of oxygen vacancies because ESB has a higher concentration of oxygen vacancies than SDC. Hence, if the layers had the same thickness, there would be a larger electrical potential drop across the SDC layer. So to allow a larger voltage drop (up to 0.4 V at 800 °C or up to 0.6 V at 500 °C) across the ESB layer, the thickness of the SDC layer must be reduced relative to that of the ESB layer.

Consequently, in *closed-circuit* conditions, the total ASR of the bilayer at 800 °C is 45% of the ASR of a single SDC layer of the same thickness—or approximately twice the ASR of a single ESB layer of the same thickness. At 500 °C, even better results are obtained where the total ASR of the bilayer is ~38% of the ASR of a single SDC layer of the same thickness or approximately equal to the ASR of a single ESB layer of the same thickness.

Table 5-2 also shows that τ^* (and therefore the ASR) is essentially independent of t'_{ion} (also K_r and K_m). This is a consequence of the *leakage* current being negligibly small in *short-circuit* conditions—when the electronic current travels through the external circuit and the electrolyte behaves like a perfect ionic conductor ($t'_{ion} = 1$)—and because the ESB layer blocks electronic current.

Short-circuit conditions, provide us with a worst case scenario for a closed-circuit SOFC, i.e., an SOFC delivering power to a load. However, we are even more interested in the optimal delivery of that power. Again neglecting the effect of the electrodes,

$$W = I_{ext}\Delta\Phi = I_{ext}t'_{ion}\Phi_{th} - I_{ext}^2 R_{load} \tag{5.28}$$

where W is the power delivered to the load. Differentiating Eq. (5.28) and setting the result to zero we are able to find the current at which maximum power, W_{max}, is delivered. Then, by substituting that expression into Eq. (5.27), we have

$$\Delta\Phi_{W_{max}} = \tfrac{1}{2}t'_{ion}\Phi_{th} \approx \tfrac{1}{2}\Phi_{th} \tag{5.29}$$

where, $\Delta\Phi_{W_{max}}$ is $\Delta\Phi$ for maximum power delivery.

Table 5-3 shows the results of the model for τ and ASR when the bilayer is optimized for maximum power delivery ($\tau^*_{W_{max}}$ and $ASR_{W_{max}}$ respectively). The values of Θ are omitted from Table 5-3 since they correspond exactly to those in Table 5-2. At 500 °C the decomposition potential for ESB (~0.6 V) is greater than $\Delta\Phi_{W_{max}}$ ($\approx \Phi_{th}/2 = 0.37$ V), therefore $\tau^* = 0$ and the

Table 5-3. $\tau^*_{W_{max}}$ and ASR (L = 10 μm) at 800 °C and 500 °C in *closed-circuit* conditions.

T (°C)	K_r ($m^{-9}atm.^{1/2}$)	K_m ($m^{-3}atm.^{-1/2}$)	$\tau^*_{W_{max}}$	$ASR_{W_{max}}$ †† (Ωcm^2)
800	†1.0×10^{72}	2.0×10^{23}	0.051	0.003
800	‡1.0×10^{72}	8.4×10^{23}	0.051	0.003
500	n.a.	1.0×10^{18}	0	0.048
500	n.a.	9.3×10^{18}	0	0.048

† Calculated from thermogravimetric data of Kobayashi *et al.* [43] in section 3.4.1.

‡ Obtained from fitting Eq. (3.19) to experimental data—see section 4.3 and Table 4-2.

†† ASR, SDC: 0.011 Ωcm^2 at 800 °C; 0.13 Ωcm^2 at 500 °C; ESB: 0.0024 Ωcm^2 at 800 °C; 0.048 Ωcm^2 at 500 °C.

ASR is the same as that of an ESB layer. Table 5-3 shows that $\tau^*_{W_{max}}$ and $ASR_{W_{max}}$ are significantly smaller than τ^* and ASR in Table 5-2, a direct consequence of the reduced operating voltage needed for maximum power delivery versus maximum current delivery (i.e., *short-circuit* conditions). For maximum power delivery, the ASR of the bilayer is just ~25% greater than the ASR of a single ESB layer of the same thickness.

5.3. SUMMARY

The feasibility of a bilayered electrolyte consisting of a layer of SDC on the fuel (reducing side) side and ESB on the air (oxidizing) side of an SOFC has been studied. Expressly, the feasibility of the bilayered electrolyte depends on the optimization of the thickness ratio of the layers so that the ESB layer is protected from decomposition in a highly reducing (low P_{O_2}) atmosphere while the ionic conductance of the combination is maximized. Consequently, it is necessary to obtain a stability criterion for ESB and its functional relationship to τ. It was argued that in *open-circuit* conditions it is sufficient to know the P_{O_2} at the SDC-ESB interface while in *closed-circuit* conditions it is necessary to know the voltage drop, $-\Delta\phi^{\delta}$, across the ESB layer.

In *open-circuit* conditions, ("thermodynamic" and "transport") models developed for oxygen flux were used to obtain the functional relationship between the τ and the effective P_{O_2} at the SDC-ESB interface. Both approaches produced essentially identical results, which further substantiates their validity.

Using our best estimates of K_r and K_m at 800 °C, the bilayer model showed that τ^* lies between 9 and 18 in *open-circuit* conditions. In *closed-circuit* conditions τ^* is ~0.4 if the bilayer is optimized for maximum current delivery and ~0.05 for maximum power delivery. Similarly,

at 500 °C, τ lies between 1.5 and 10 in *open-circuit* conditions and is ~0.03 in *closed-circuit* conditions and $\tau^* \rightarrow 0$ at maximum power delivery

Since ESB has a higher ionic conductivity than SDC, a lower ASR for the bilayer is obtained for the smaller value of τ and, for the most efficient delivery of power, one would prefer the lowest ASR. This implies that an SDC-ESB bilayered SOFC would have the best performance if it was fabricated with a τ^* based on *closed-circuit* conditions—for maximum delivery of either power or current. This is not a problem since, in principle, a fuel cell is used to deliver current/power to a load. Moreover, *open-circuit* conditions in the presence of a reducing gas can be avoided by purging the gas or to just allow the fuel cell to cool since the decomposition P_{O_2} for ESB decreases with temperature. The latter solution is attractive because of its simplicity, however it would have to be carefully implemented since the effective P_{O_2} of the fuel also reduces with temperature.

6. BILAYER: EXPERIMENTAL RESULTS

In this section, initial results of experiments on SOFCs with SDC\ESB bilayered electrolytes are presented.

6.1 OPEN CIRCUIT VOLTAGE

The open-circuit voltage of an oxygen concentration cell of the type:

$$P_{O_2}, \text{ Au/ESB\SDC/Pt, } P_{CO/CO_2} \left(\text{or } P_{H_2/H_2O}\right) \tag{6.1}$$

was measured as a function of P_{O_2} on the anode (fuel) side and temperature and used to calculate t'_{ion}. Au paste was coated on the ESB layer for a cathode and Pt paste was coated on the SDC layer for an anode. Figures 6-1 and 6-2 compare Φ_{oc} and t'_{ion}, respectively, obtained for single layer SDC (Eq. (4.1)) and bilayered SDC\ESB (Eq. (6.1)) cells. The SDC\ESB cell showed a substantial increase in Φ_{oc} and t'_{ion}, compared to the single layered, SDC-based SOFC cell. Also, the Φ_{oc} of the SDC\ESB cell was greater than that of SDC at any temperature. This enhancement in _oc and t'ion, is due to the ability of the ESB layer to block electronic conduction. Thus further confirming our bilayer concept.

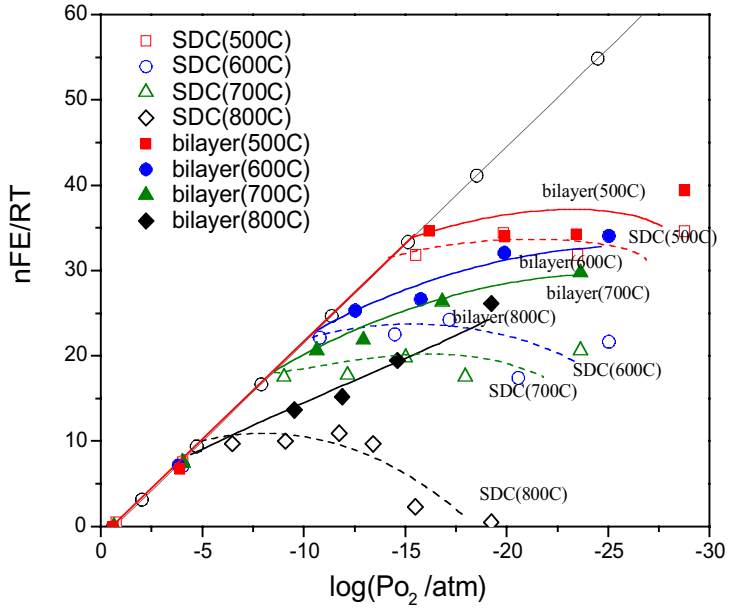

(a)

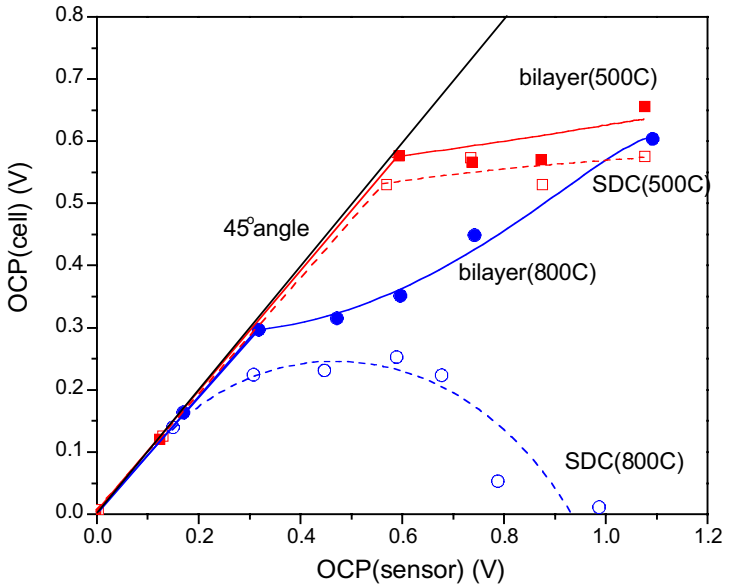

(b)

Figure 6-1. Comparison of Φ_{oc} (*nFE/RT*) of fuel cells in Eqs. (4.1) and (6-1) as a function of (a) P_{O_2} and (b) sensor voltage (Φ_{th}); ESB thickness: 1.3μm.

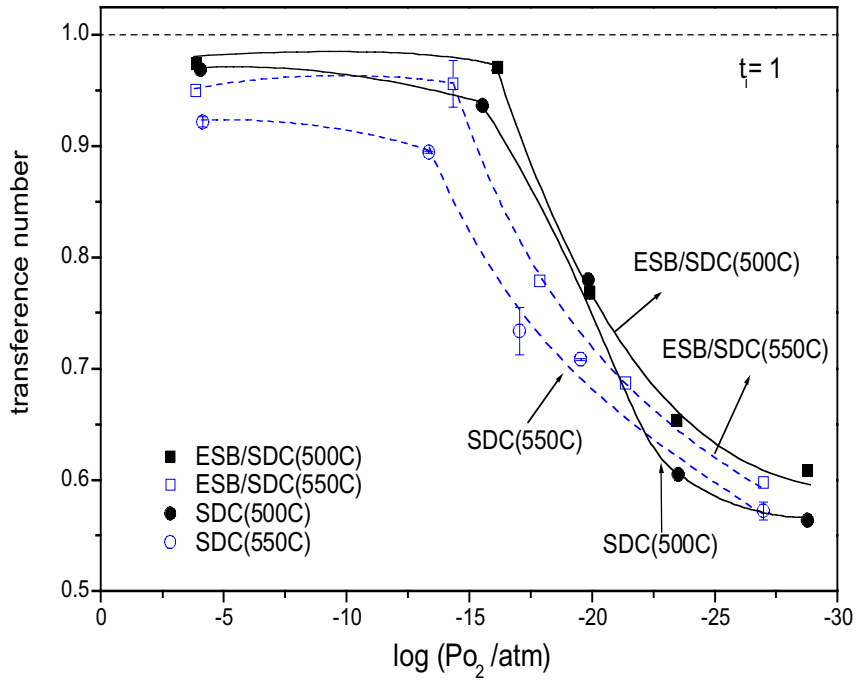
transference number
log (Po2 /atm)
ti= 1
ESB/SDC(500C)
ESB/SDC(550C)
SDC(500C)
SDC(550C)
ESB/SDC(500C)
ESB/SDC(550C)
SDC(550C)
SDC(500C)

(a)

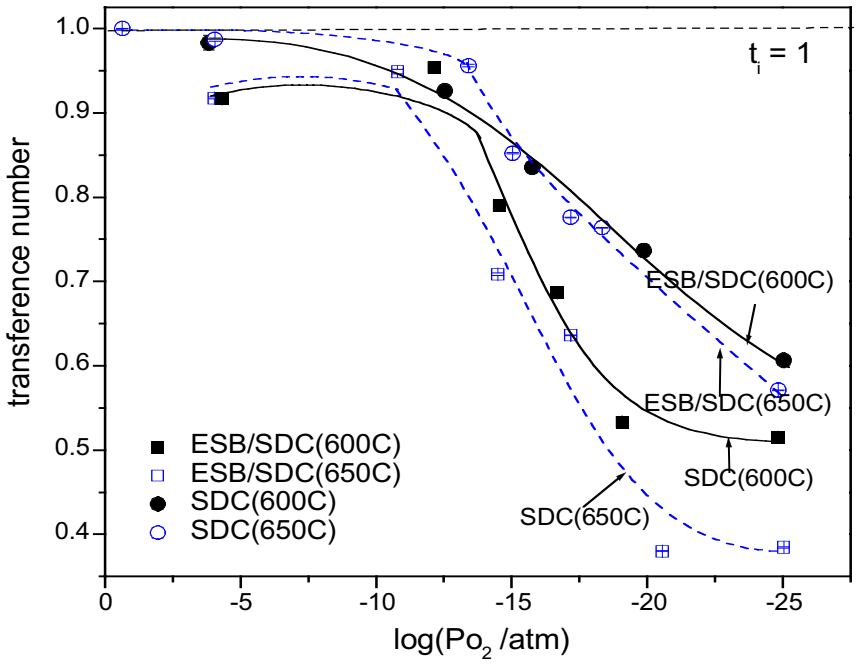
transference number
log(Po2 /atm)
ti = 1
ESB/SDC(600C)
ESB/SDC(650C)
SDC(600C)
SDC(650C)
ESB/SDC(600C)
ESB/SDC(650C)
SDC(600C)
SDC(650C)

(b)

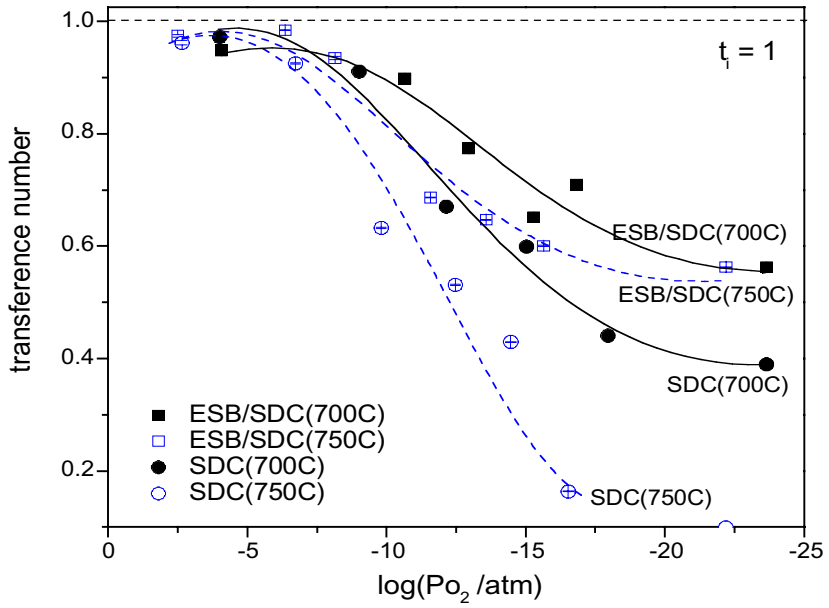

(c)

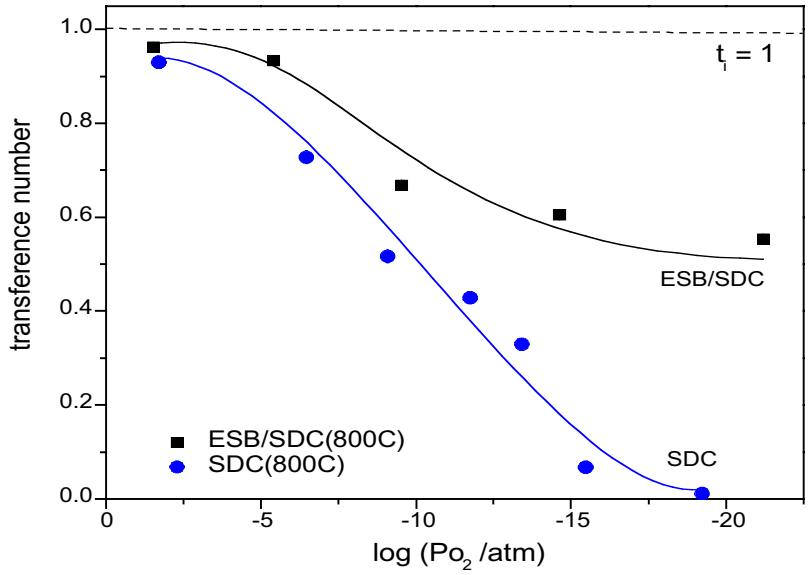

(d)

Figure 6-2. Comparison of t'_{ion} of fuel cells in Eqs. (4.1) and (6-1) as a function of P_{O_2} at (a) 500 and 550℃, (b) 600 and 650℃, (c) 700 and 750℃, and (d) 800℃.

6.2 EFFECT OF RELATIVE THICKNESS ON Φ_{OC} AND t'_{ion}

To investigate the effect of relative thickness of bilayered SDC\ESB electrolytes on Φ_{oc} and t'_{ion}, two cells were prepared by depositing ESB layers via PLD on identical SDC substrates. The thicknesses of the ESB layers (0.8 μm and 1.3 μm) were determined from profilometry and SEM analysis. Henceforth, each bilayer substrate is identified as SDC\ESB0.8 and SDC\ESB1.3 corresponding to ESB thicknesses of 0.8 μm and 1.3 μm respectively. Table 6-1 shows the relative thickness of SDC\ESB electrolytes, including some of our previous data [59].

Open circuit voltage and t'_{ion} of SDC\ESB0.8 and SDC\ESB1.3 cells are shown in Figures 6-3 and 6-4 respectively, as a function of P_{O_2} for 500 °C ≤ T ≤ 800 °C. Table 6-2 shows the values of P_{O_2} at which t'_{ion} falls below 0.9 for SDC and SDC\ESB. Open circuit voltage and t'_{ion} of SDC\ESB0.8 and SDC\ESB1.3 cells show similar results, because the relative thickness of SDC\ESB layers in the two cells is of the same order of magnitude.

To further explore the effect of the relative thickness of the constituent layers of SDC\ESB bilayers, Φ_{oc} and t'_{ion} data from Wachsman *et al*. [59]—taken for SDC\ESB cells under identical conditions of (H_2/H_2O on the anode side and air on the cathode side)—was included in the analyses. As shown in Figures 6-5 and 6-6, in the temperature range studied, Φ_{oc} and t'_{ion} increased significantly as the ESB film thickness increased, approaching ~1 V and ~0.9 respectively for a relative thickness (ESB\SDC) of 0.03. Therefore, the theoretical (Nernst) voltage and a t'_{ion} of unity is achievable with a thicker ESB layer relative to SDC (for a given total thickness). This again confirms the bilayer concept.

Table 6-1. Relative Thicknesses of SDC\ESB Electrolytes

Electrolytes	SDC layer thickness (mm)	ESB film thickness (μm)	Relative thickness (ESB\SDC)
SDC\ESB0.8	1.601	0.8	$5.0 \leftrightarrow 10^{-4}$
SDC\ESB1.3	1.756	1.3	$7.4 \leftrightarrow 10^{-4}$
SDC\ESB30†	1.0	30	$3.0 \leftrightarrow 10^{-2}$

†: relative thickness from previous results (from Wachsman et al. [59])

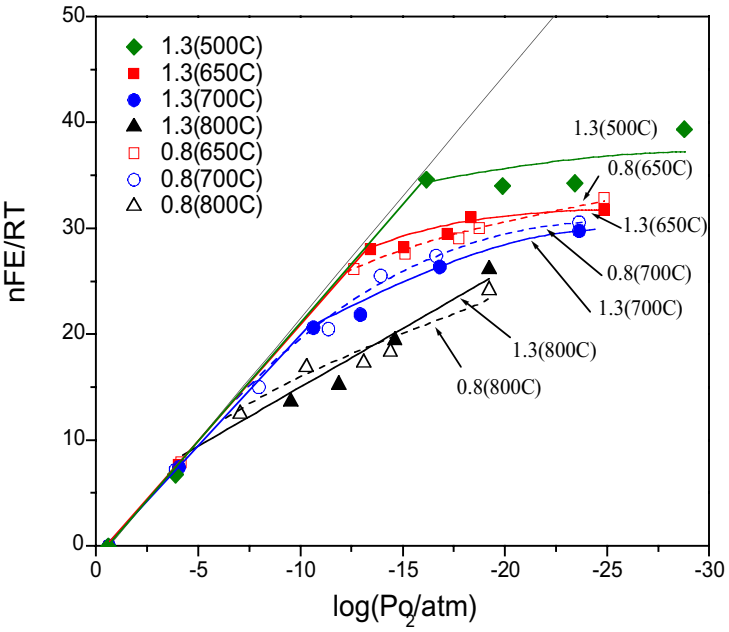

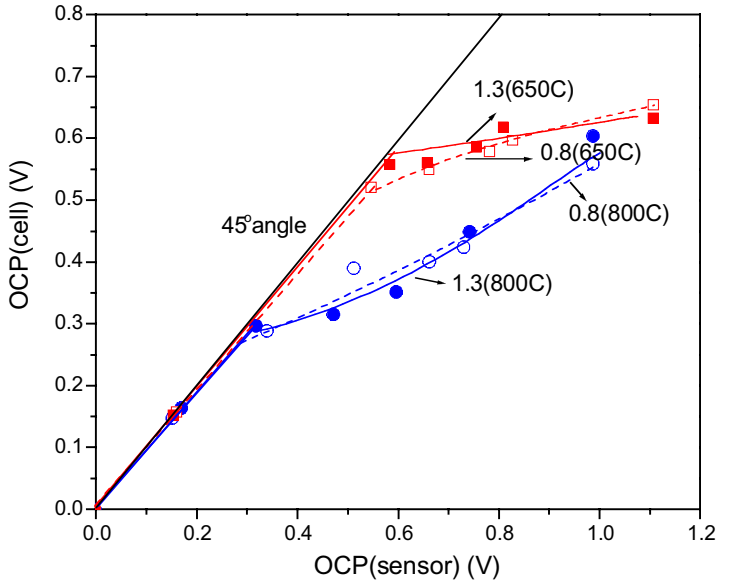

Figure 6-3. Comparison of Φ_{oc} (*nFE/RT*) of SDC\ESB0.8 and SDC\ESB1.3 concentration cells (Eq. (6.1)) as a function of (a) P_{O_2} and (b) sensor voltage (Φ_{th}).

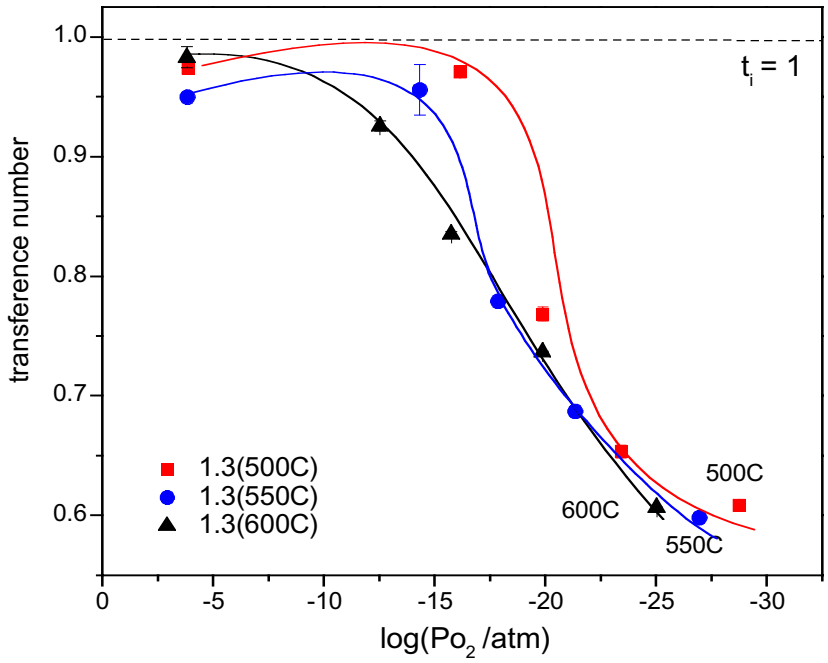
1.0
0.9
0.8
0.7
0.6
transference number
t_i = 1
1.3(500C)
1.3(550C)
1.3(600C)
500C
600C
550C
0
-5
-10
-15
-20
-25
-30
log(Po_2 /atm)

(a)

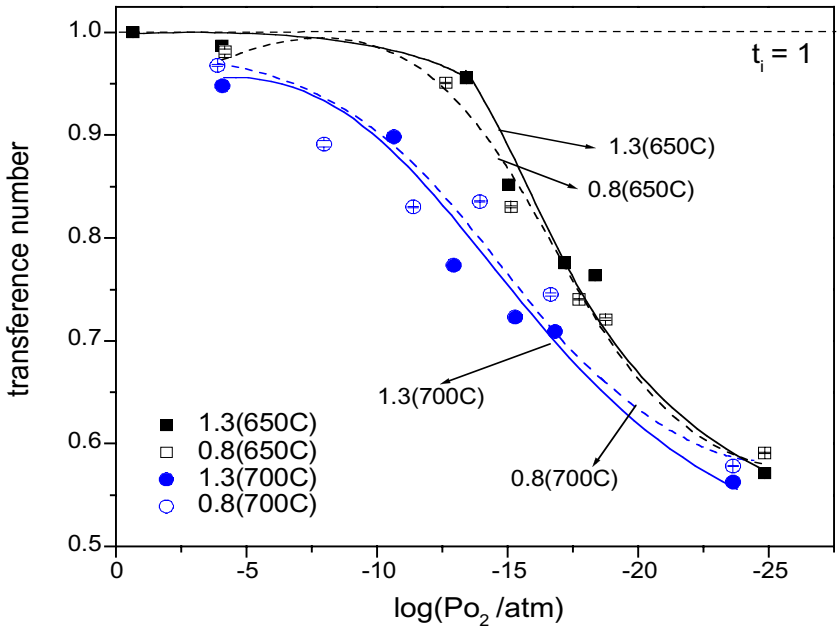
1.0
0.9
0.8
0.7
0.6
0.5
transference number
t_i = 1
1.3(650C)
0.8(650C)
1.3(700C)
0.8(700C)
1.3(650C)
0.8(650C)
1.3(700C)
0.8(700C)
0
-5
-10
-15
-20
-25
log(Po_2 /atm)

(b)

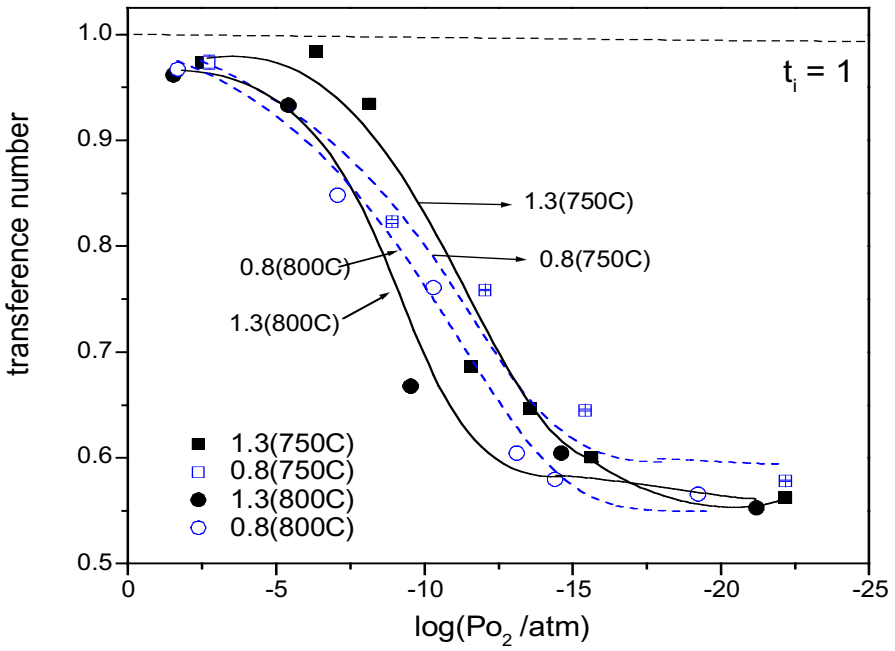

(c)

Figure 6-4. Comparison of t'_{ion} for SDC\ESB0.8 and SDC\ESB1.3 cells (Eq. (6.1)) as a function of P_{O_2} at (a) 500 and 550 °C, (b) 650 and 700 °C, (c) 750 and 800 °C.

Table 6-2. Oxygen Partial Pressure at which t'_{ion} = 0.90 for SDC, SDC\ESB0.8 and SDC\ESB1.3 cells (in Eqs. (4.1) and (6-1)).

Temperatures (°C)	SDC (0)[1]	0.8SDC\ESB (5.0×10^{-4})[1]	1.3SDC\ESB (7.4×10^{-4})[1]
500	$\sim 10^{-17.5}$		$\sim 10^{-17.5}$
550	$\sim 10^{-14}$		$\sim 10^{-16}$
600	$\sim 10^{-13.5}$		$\sim 10^{-15}$
650	$\sim 10^{-13}$	$\sim 10^{-14.5}$	$\sim 10^{-14.5}$
700	$\sim 10^{-9.5}$	$\sim 10^{-9}$	$\sim 10^{-11}$
750	$\sim 10^{-7.5}$	$\sim 10^{-8}$	$\sim 10^{-8.5}$
800	$\sim 10^{-4}$	$\sim 10^{-7}$	$\sim 10^{-7}$

()[1]: relative thickness of electrolytes (SDC\ESB)

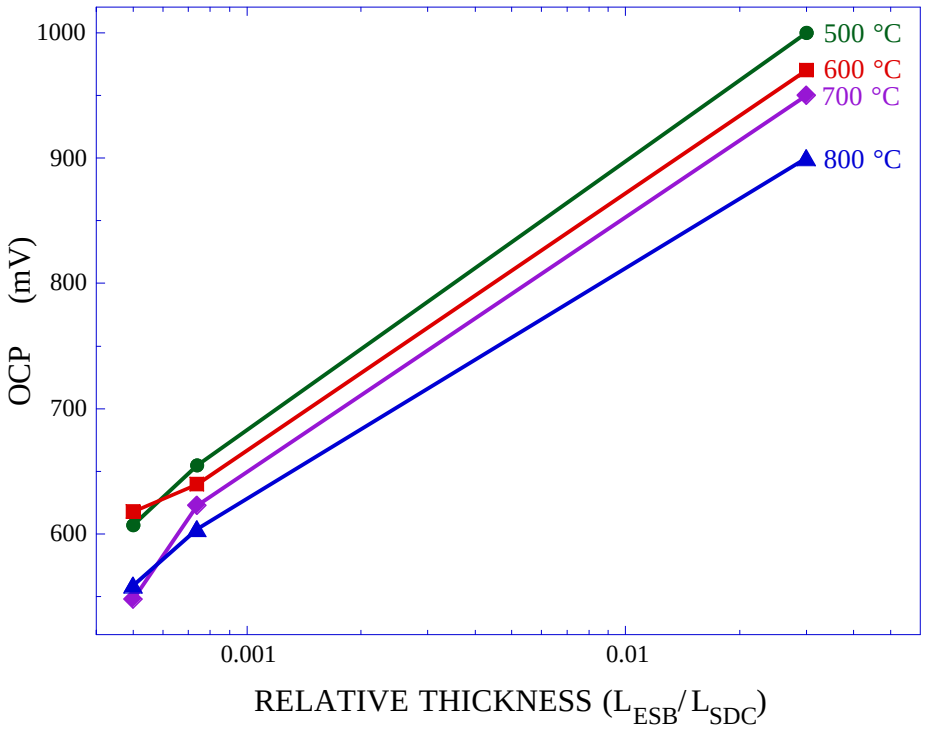

Figure 6-5. Dependence of Φ_{oc} on relative thickness of the constituent layers of SDC\ESB SOFC.

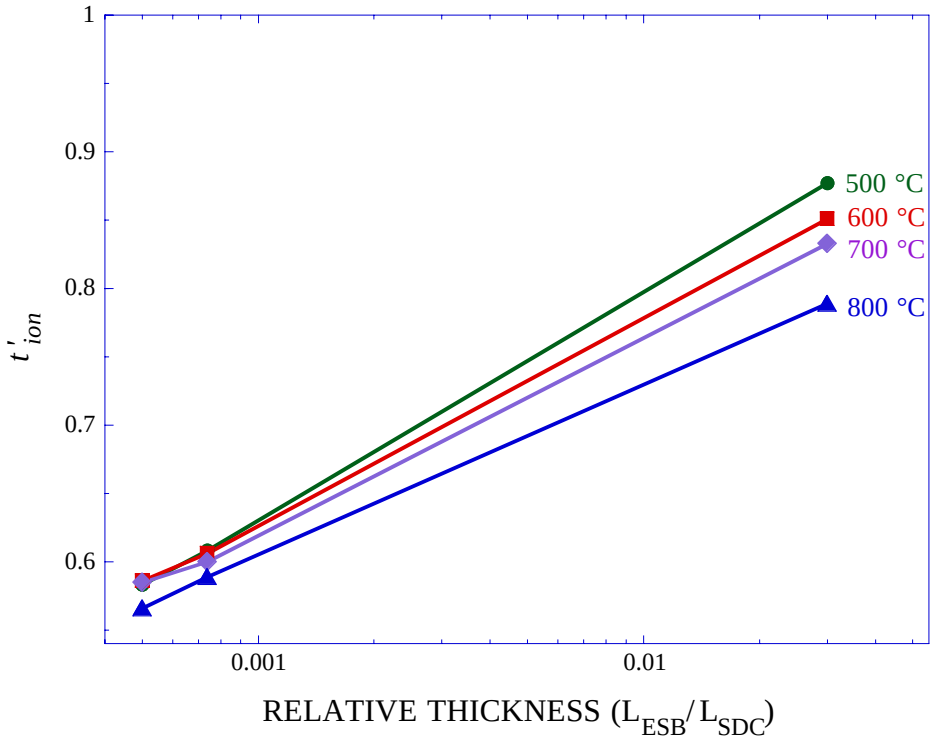

Figure 6-6. Dependence of t'_{ion} on relative thickness of the constituent layers of SDC\ESB SOFC.

7. REFERENCES

1. K. Mehta, S. J. Hong, J. -F. Jue and A. V. Virkar, in *Solid Oxide Fuel Cells III*, S. C. Singhal and H. Iwahara, ed., PV 93-4, p. 92, Electrochem. Soc. Proc. Series.
2. P. Soral, U. Pal and W. Worrell, *J. Electrochem. Soc.* **145** (1998) 99.
3. P. Shuk, H. -D. Wiemhöfer, U. Guth, W. Gopel and M. Greenblatt, *Solid State Ionics* **89** (1996) 179.
4. A. M. Azad, S. Larose and S. A. Akbar, *J. Mat. Sci*. **29** (1994) 4135.
5. J. Van herle, T. Horita, T. Kawada, N. Sakai, H. Yokoko and M. Dokiya, *Solid State Ionics*, **86-88** (1996) 1255.
6. W. Huang, P. Shuk, and M. Greenblatt, *Solid State Ionics*, **100** (1997) 23.
7. M. N. Rahaman, *Ceramic Processing and Sintering*, Marcel Decker, Inc., New York 1995.
8. P. D. Battle, C. R. A. Catlow, J. W. Heap and L. M. Moroney, J. Solid State Chem. 63, 8 (1986)
9. N. Jiang and E.D. Wachsman, J. Am. Ceram. Soc., 82 [11] 3057 - 64 (1999)
10. E. D. Wachsman, S. Boyapati, M. J. Kaufman, N. Jiang, J. Am. Ceram. Soc. 83 (2000) 1964 – 1968
11. E. D. Wachsman, N. Jiang, D. M. Mason and D. A. Stevenson, Proc. Electrochem., Soc., 89 - 11, 15 (1989)
12. S. Boyapati, E. D. Wachsman and B. C. Chakoumakos, Solid State Ionics 138 (2001) 293-304
13. S. Boyapati, E. D. Wachsman and N. Jiang, Solid State Ionics, 140 (2001) 149-160
14. E. D. Wachsman, S. Boyapati and N. Jiang, Ionics, 7 (2001) p. 1
15. T. Takahashi and H. Iwahara, J. of Appl. Electrochem. 3 (1973) 65-72
16. M. J. Verkerk and A. J. Burggraaf, J. Electrochem., 128 (1981) 75
17. G. Meng, C. Chen, X. Han, P. Yang and D. Peng, J. Mat. Sci. 28-30 (1988) 533

18. K. Z. Fung and A. V. Virkar, J. Am. Ceram. Soc., 74 [8] 1970-80 (1991)
19. B.C.H. Steele, *Solid State Ionics*, **129** (2000) 95.
20. A. V. Virkar, G. R. Miller, and R. S. Gordon, *J. Am. Ceram. Soc*., **61** (1978) 250.
21. S. J. Hong, K. Mehta, and A.V. Virkar, *J. Electrochem. Soc.*, **145** (1998) 638.
22. C. Tian and S. Chan, *Solid State Ionics*, **134** (2000) 89.
23. R. Gerhardt and A. S. Nowick, *J. Am. Ceram. Soc*., **69** (1986) 641.
24. R. Gerhardt, A. S. Nowick, M. E. Mochel, and I. Dumler, *J. Am. Ceram. Soc*., **69** (1986) 647.
25. E. Schouler, G. Girond, M. Kleitz, *J. Chem. Phys*., **70** (1973).
26. G. M. Christie and F. P. F. van Berkel, *Solid State Ionics*, **83** (1996) 17.
27. P. L Chen and I. W. Chen, *J. Am. Ceram. Soc*., **79** (1996) 1793.
28. S. Jung, E. D. Wachsman and N. Jiang, submitted, Ionics
29. E.D. Wachsman, N. Jiang, D. M. Mason, and D. A. Stevenson, *Proceedings of the first international syposium on Solid Oxide Fuel Cells* **89-11**, ed. S. C. Singhal Electrochem. Soc. Proc. Series.
30. E. D. Wachsman, S. Boyapati, M. J. Kaufman, and N. Jiang, *Solid State Ionic Devices: Proc. Electrochem. Soc.*, **42** (1999).
31. D. Y. Wang, D. S. Park, J. Griffith, and A. S. Nowick, *Solid State Ionics*, **2** (1981) 95.
32. S. Ohara, R. Maric, X. Zhang, K. Mukai, T. Fukui, H. Yoshida, T. Inagaki, K. Miura, *J. Power Sources*, 86, 455 (2000).
33. J. Will, A. Mitterdorfer, C. Kleinlogel, D. Perednis, L.J. Gaukler, *Solid State Ionics*, 131, 79 (2000).
34. S. deSouza, S.J. Visco, L.C. DeJonghe, *J. Electrochem. Soc.*, 144, L35 (1997).
35. K.T. Miller, F.F. Lange, D.B. Marshall, *J. Mater. Res.*, 5, 151 (1990).
36. K. Duncan, Ph. D. Thesis, University of Florida (2001).
37. J. Newman, Electrochemical Systems (Prentice-Hall, 1991).

38. F. W. Poulsen, *Solid State Ionics* **129** (2000) 145.
39. F. W. Poulsen, *J. Solid State Chem.* **143** (1999) 115.
40. I. Riess and J. Schoonman in: Handbook of Solid State Electrochemistry, ed. P. J. Gellings and H. J. M. Bouwmeester (CRC Press, 1997) chap. 8, p. 269.
41. W. Weppner in: Handbook of Solid State Electrochemistry, ed. P. J. Gellings and H. J. M. Bouwmeester (CRC Press, 1997) chap. 9, p. 295.
42. S. Wang, H. Inaba, H. Tagawa, M. Dokiya and T. Hashimoto, *Solid State Ionics* **107** (1998) 73.
43. T. Kobayashi, S. Wang, M. Dokiya, Hiroaki T. and T. Hashimoto, *Solid State Ionics* **126** (1999) 349.
44. H. Inaba and H. Tagawa, *Solid State Ionics* **83** (1996) 1.
45. M. Godickemeier, K. Sasaki, L. Gauckler and I. Riess, *J. Electrochem. Soc*. **144** (1997) 1635.
46. M. Godickemeier and L. Gauckler, *J. Electrochem. Soc*. **145** (1998) 414.
47. K. Eguchi, T. Setoguchi, T. Inoue and H. Arai, *Solid State Ionics* **52** (1992) 265.
48. J. -Y. Park, M. Sc. Thesis, University of Florida, (2001).
49. M. R. Spiegel in, Schaum's Outline Series: Theory and Problems of Statistics 2nd. edition (McGraw-Hill, 1994).
50. P. J. Gellings, H. J. A. Koopmans and A. J. Burggraaf, *App. Catalysis* **39** (1988) 1
51. E. D. Wachsman, Ph. D. Thesis, Stanford University (1990).
52. K. L. Duncan and E. D. Wachsman, *Ionics* **6** (2000) 145.
53. C. Wagner, *Z. Elektrochem*. **60** (1956).4.
54. E. D. Wachsman and K. L. Duncan, *Proceedings of the International Symposium on Solid State Ionic Devices*, Vol. 99-13 (The Electrochemical Society, Inc. 1999), p. 159.
55. T. Takahashi, H. Iwahara and T. Arao, *J. App. Electrochem*. **7** (1977) 299.
56. M. J. Verkerk, K. Keizer and A. J. Burggraaf, *J. App. Electrochem*. **10** (1980) 81.

57. M. J. Verkerk and A. J. Burggraaf, *J. App. Electrochem.* **10** (1980) 677.

58. V. V. Kharton and F. M. B. Marques, *Solid State Ionics* **140** (2001) 381.

59 E. D. Wachsman, P. Jayaweera, N. Jiang, D.M. Lowe, and B.G. Pound, *J. Electrochem. Soc*., 144 (1997) 233.